Energy & Environmental Science

ROYAL SOCIETY OF CHEMISTRY

REVIEW

View Article Online
View Journal

Cite this: DOI: 10.1039/d5ee07830j

Review of module designs for organic and perovskite solar cells

Jae Won Kim,†[a] You-Hyun Seo,†[a] Hee Jeong Jeong,[ab] Eun Chong Chae,[ac] Helen Hejin Park,[ad] Bong Joo Kang,[a] Kyungsik Kim,[e] Jinho Lee,*[e] Soonil Hong*[a] and Nam Joong Jeon*[af]

Received 27th December 2025,
Accepted 19th March 2026

DOI: 10.1039/d5ee07830j

rsc.li/ees

Organic solar cells (OSCs) and perovskite solar cells (PSCs) are emerging as promising next-generation alternatives to conventional silicon solar cells because of their rapidly increasing power conversion efficiency (PCE); potential for low-cost manufacturing; and suitability for diverse applications, including building- and vehicle-integrated photovoltaics, space-based solar power sources, and portable power sources. With the certified PCEs of OSCs and PSCs reaching 19.2% and 27.0%, respectively, significant effort is now directed toward upscaling these cells for commercialization. However, this transition presents a critical challenge: compared with those of their small-area cell (~0.1 cm^2) counterparts, the PCEs of large-area modules (>10 cm^2) typically decrease by 20–30%, posing a significant barrier to the replacement of silicon-based technologies. While laser scribing is a prevalent technique for producing efficient large-area modules, it frequently introduces process-induced damage and stability concerns, as well as high process costs. This review critically examines the various module designs that are used in OSC and PSC fabrication schemes, summarizes the tradeoffs among different patterning techniques, and proposes future design directions that can bridge the efficiency gap and provide enhanced long-term stability.

Broader context

The climate crisis has accelerated the development of renewable energy resources, among which organic solar cells (OSCs) and perovskite solar cells (PSCs) have gained prominence as leading next-generation photovoltaic platforms. Although significant efforts are underway to commercialize these devices, a considerable efficiency gap persists between small-area cells and large-area modules, even as laboratory device efficiencies approach those of crystalline silicon. Unlike silicon photovoltaics, OSC and PSC architectures encounter unique performance-degrading factors when scaled up through monolithic serial interconnection of subcells (typically 5–10 mm in width). This comprehensive review first elucidates the fundamental principles of the dominant monolithic series-connected architecture, focusing on the critical trade-offs between resistive and geometric losses. We then provide an overview of the evolution of patterning technologies, ranging from mechanical and printing methods to high-precision laser scribing that has enabled recent record-efficiency modules. Furthermore, we highlight the frontier of innovative P2-free or scribeless designs that redefine conventional module fabrication paradigms by minimizing cell-to-module loss.

[a] Division of Advanced Materials, Korea Research Institute of Chemical Technology (KRICT), 141 Gajeong-ro, Yuseong-gu, Daejeon 34114, Republic of Korea. E-mail: sihong@krict.re.kr, njjeon@krict.re.kr
[b] Department of Chemical and Biological Engineering, Korea University, 145 Anam-ro, Seongbuk-gu, Seoul 02841, Republic of Korea
[c] Department of Materials Science and Engineering, Seoul National University, 1 Gwanak-ro, Gwanak-gu, Seoul 08826, Republic of Korea
[d] Department of Chemical and Biological Engineering, Hanbat National University, 125 Dongseo-daero, Yuseong-gu, Daejeon 34158, Republic of Korea
[e] Department of Physics, Department of Intelligent Semiconductor Engineering, Incheon National University, 119 Academy-ro, Yeonsu-gu, Incheon 22012, Republic of Korea. E-mail: jlee@inu.ac.kr
[f] Institute for Advanced Technology Convergence, Kyungpook National University, 80 Daehak-ro, Buk-gu, Daegu 41566, Republic of Korea
† Jae Won Kim and You-Hyun Seo contributed equally to this work.

1. Introduction

Net-zero policies are being implemented worldwide, and significant efforts are being directed toward the development of renewable energy sources to address the global climate change crisis.[1–3] Among these methods, solar cells, which are considered a key technology, convert sunlight into electricity without depleting natural resources.[3–6] Since their initial development at Bell Labs in 1954, crystalline silicon solar cells have become the dominant force in the photovoltaic market, accounting for more than 90% of sales.[7–10] Facilitated by continuous technological advancements, single-crystal silicon solar cells have

achieved impressive power conversion efficiencies (PCEs) that are now approaching 27% and long-term lifespans of more than 20 years.[7–11] However, despite their success, conventional silicon solar cells face limitations related to their energy-intensive manufacturing processes, rigidity, and weight, which can restrict their application ranges.[8–13] To overcome these challenges, third-generation photovoltaics such as organic solar cells (OSCs) and perovskite solar cells (PSCs) are gaining significant attention.[13–17] These technologies offer unique advantages, such as solution-based low-cost processing, light weights, and high mechanical flexibility. However, translating these benefits from small, laboratory-scale cells to large-area commercial products presents a significant hurdle.[18–21] Therefore, the design and fabrication of efficient and stable modules have become pivotal research areas for unlocking the full potential of these next-generation technologies.

Currently, the applications of solar cells are rapidly expanding beyond traditional ground-mounted power generation systems to diverse fields, such as building-integrated photovoltaics (BIPVs), vehicle-integrated photovoltaics (VIPVs), smart farms, and portable power solutions.[22–28] These emerging applications demand a new set of attributes, including light weights, mechanical flexibility, and tunable aesthetics. However, crystalline silicon solar cells face inherent limitations: their indirect bandgaps result in low absorption coefficients, necessitating thick wafers (typically $\sim$180 μm) to achieve sufficient sunlight absorption levels, which increases both the weights and material costs of the cells.[2,7,12] This intrinsic thickness of silicon wafers, combined with their brittleness, makes them prone to cracking during operation or installation processes, requiring protection *via* rigid encapsulation with tempered glass and robust frames. In contrast, OSCs and PSCs possess direct bandgaps that yield high absorption coefficients, enabling efficient light harvesting at thin film thicknesses (typically <1 μm).[23,29–31] Their use of organic or hybrid materials provides compatibility with flexible substrates, reducing their weights and improving their form factors. Furthermore, the bandgaps of OSCs and PSCs can be finely tuned through molecular design, doping, or compositional engineering schemes, providing opportunities for seamlessly integrating these cells into urban environments where both performance and aesthetics are prioritized.[31–34]

Over the past two decades, both OSCs and PSCs have demonstrated remarkable progress in terms of laboratory-scale device efficiency, with certified PCEs of 19.2% for OSCs and 27.0% for PSCs, as reported by the National Laboratory of the Rockies (NLR).[35,36] As the performance of these small-area cells improved, research into upscaling them for the development of modules commenced in earnest, beginning in 2009 for OSCs and in 2014 for PSCs.[37–39] Nevertheless, the module fabrication process is hindered by the significant reduction exhibited by the PCE when scaling from small-area cells to large-area modules; this is reflected in the certified NLR module records, which have demonstrated PCEs of 14.5% for OSC modules and 21.1% for PSC modules.[36,40] Compared with crystalline silicon solar cells, which are fabricated from wafers grown with the Czochralski method, solution-processed OSCs and PSCs encounter distinct challenges during the scale-up phase, including nonuniform film thicknesses and morphologies and the formation of defects such as pinholes, all of which compromise the performance of the constructed devices.[20,21,41,42] Furthermore, both OSCs and PSCs typically employ monolithic module architectures in which multiple subcells are interconnected in series with narrow widths (typically 5–10 mm), effectively reducing the ohmic losses caused by the sheet resistance of transparent electrodes.[20,21,28,43–45] While effective, this type of architecture necessitates a delicate patterning process for the interconnection lines, creating nonproductive ''dead areas''. Maximizing the ratio of the photoactive area to the total area, *i.e.*, the geometrical fill factor (GFF), is therefore essential for module design purposes.[46–48]

This review provides a comprehensive overview of the existing module design and fabrication schemes for OSCs and PSCs, focusing on the key architectures and patterning techniques. We start with monolithic module architectures based on mechanical patterning processes, including early manual patterning approaches, and then focus on the printing-based patterning methods that are commonly used for solution-processable solar cells, such as slot-die coating and screen printing. The discussion then shifts to the laser scribing technique, which is a dominant and highly precise method for creating monolithic interconnections in both OSC and PSC modules. This review subsequently explores alternative module architectures that move beyond the traditional monolithic approach, highlighting the novel interconnection and device layout strategies. Finally, we provide an overview of the key strategies and a future outlook with respect to other challenges, such as the fabrication of commercial modules and the implementation of AI assistance for both OSC and PSC modules.

2. Monolithic module designs

Single-junction OSCs and PSCs are typically constructed in a planar configuration consisting of a substrate/transparent electrode/electron transport layer (ETL) or hole transport layer (HTL)/photoactive layer/HTL or ETL/top electrode, with interface modification techniques applicable at each layer.[15,29,49,50] The transparent electrode is patterned or etched to prevent electrical shorting between the bottom and top electrodes, after which each functional layer is sequentially deposited under appropriate processing conditions. Finally, the top electrode is deposited through a mask to collect charges from the active layer, whereas the transparent bottom electrode extracts carriers with opposite polarities, enabling photovoltaic operations.

A key advantage of these technologies is that many of their functional layers are solution-processable. This allows for the implementation of various printing and coating techniques, where printable inks prepared from organic semiconductors or perovskite precursors enable the deposition of thin, uniform films over large areas, holding promise for low-cost, high-throughput manufacturing processes.[37,51] In addition to wet-processing techniques, dry-processing methods based on vacuum deposition

have been proven to be useful, particularly for small-molecule OSC absorbers and co-evaporated PSC absorbers. In this solvent-free approach, materials are deposited in a high-vacuum chamber and subsequently condense onto the substrate.[52–54] While this method typically involves higher equipment costs and slower deposition rates than solution coating does, it offers exceptional film thickness and morphology control, resulting in highly uniform, pure, and reproducible multilayer structures.

The fabrication of OSC and PSC modules requires a design that is structurally different from that of conventional silicon solar cells: a monolithic, stripe-patterned, series-connected architecture.[28,55] This configuration is necessary to overcome the primary challenge of scaling up these technologies because of the limited conductivity of transparent conductive oxides (TCOs) such as indium tin oxide (ITO) and fluorine-doped tin oxide (FTO), which are used as transparent electrodes. The impact of this limitation is governed by the sheet resistance (R_{sheet}, $\Omega\ \mathrm{sq}^{-1}$), which determines the total resistance (R) of an electrode on the basis of its geometry:

$$R = R_{\mathrm{sheet}}\frac{L}{W}$$

where L is the length of the current path and W is the width of the conductive medium.[43] To construct loss-free and widely expandable solar modules in monolithic designs, transparent electrodes should be divided into stripes, either *via* pre-patterning methods (*e.g.*, selective sputtering) or post-patterning methods (*e.g.*, laser and mechanical scribing or wet etching). This approach, however, introduces a critical tradeoff. Increasing the stripe width reduces the required number of interconnection gaps (*i.e.*, areas where ITO is removed) within a given area, thus minimizing aperture losses but significantly increasing the resistive losses of the ITO, which reduces the current density and fill factor. Therefore, a balance between minimizing the aperture loss and reducing the resistive loss must be carefully maintained in the stripe geometries of subcells. Additionally, it is essential that the layers between the electrodes be patterned, with both electrodes designed to have slight shifts in their respective patterns to ensure an interconnection between the bottom transparent electrodes of one subcell and the top electrode of the neighboring subcell.[56,57] As a result, the prevailing OSC and PSC module architecture is based on a monolithic series-interconnection design, in which adjacent subcells are patterned into regularly spaced stripes, typically with widths less than 1 cm.

Precise and reproducible patterning has become indispensable for the fabrication of OSC and PSC modules.[18,28] This process involves creating finely defined scribe lines to partition the device area into individual subcells, which are monolithically interconnected in series to increase the operating voltage and ensure an efficient current management scheme while minimizing geometric losses caused by nonproductive dead areas. Such a structural segmentation strategy enhances the overall power output by reducing the resistive losses induced across large areas. The critical technical requirements of scribing include high line definition precision, minimal collateral material damage, and consistent pattern fidelity, all of which are essential for guaranteeing reliable electrical isolation and robust interconnections between subcells. Patterning can be implemented through several advanced approaches, including mechanical scribing; laser scribing, which provides superior precision and a high processing speed; and mask-assisted printing, which offers a cost-effective alternative for large-area fabrication tasks.[58–62] These techniques have been widely employed for the stripe patterning of functional layers sandwiched between cathodes and anodes, thereby establishing a series of connections that underpin the monolithic architectures of OSC and PSC modules.

In OSC and PSC modules, the pattern of the bottom transparent electrode is referred to as P1, that of the photoactive layer together with the charge transport layers is defined as P2, and that of the top electrode is denoted as P3. Minimizing the inactive areas between the P1 and P3 lines while maximizing the photoactive region directly increases the GFF (Fig. 1A). The implementation of precise patterning processes has further optimized monolithic module designs by enlarging the effective active area, thereby reducing the induced aperture losses and improving the overall performance of devices. In a monolithic module structure, accurately patterning the photoactive layer (P2) is essential; otherwise, the series connection region (SCR) functions as a reverse diode, disrupting the series connections between adjacent subcells (Fig. 1B).[63,64] The high resistance of these regions restricts current flows, leading to an uneven current distribution and power losses. Furthermore, the presence of reverse-diode behavior prevents the efficient recombination of charges in the SCR, significantly degrading the voltage gain of the module. As presented in Fig. 1C and D, the PCE of a module increases with increasing GFF, and this trend persists even for module areas exceeding 100 cm^2. Therefore, implementing appropriate patterning during the module design phase is indispensable for transforming the SCR from a rectifying junction into a low-resistance ohmic contact, thereby ensuring efficient charge transport throughout the module.

Advancements in monolithic module designs have been instrumental for improving the scalability and efficiency of OSC and PSC technologies. In monolithic architectures, interconnected strip-shaped subcells allow for efficient charge collection, enabling high voltages and improved current management across larger areas. However, the patterning approach employed during module fabrication—specifically pre-patterning *versus* post-patterning—plays a crucial role in determining the GFF, PCE, scalability, and manufacturing practicality of the developed module, as described in Fig. 2. Pre-patterning is defined as the creation of patterns on the substrate prior to the deposition of subsequent layers. This can be achieved through patterned coating methods such as slot-die coating, screen printing, gravure printing, inkjet printing, *etc.*, or selective printing and evaporation with masking patterns.[37,56,65–67] Notably, pre-patterning enables the reliable electrical isolation that is essential for serial subcell integration, minimizing the postprocess complexity level and the potential damage inflicted upon the functional layers. However, pre-patterning demands high substrate preparation precision and is susceptible to high GFFs, possibly making it

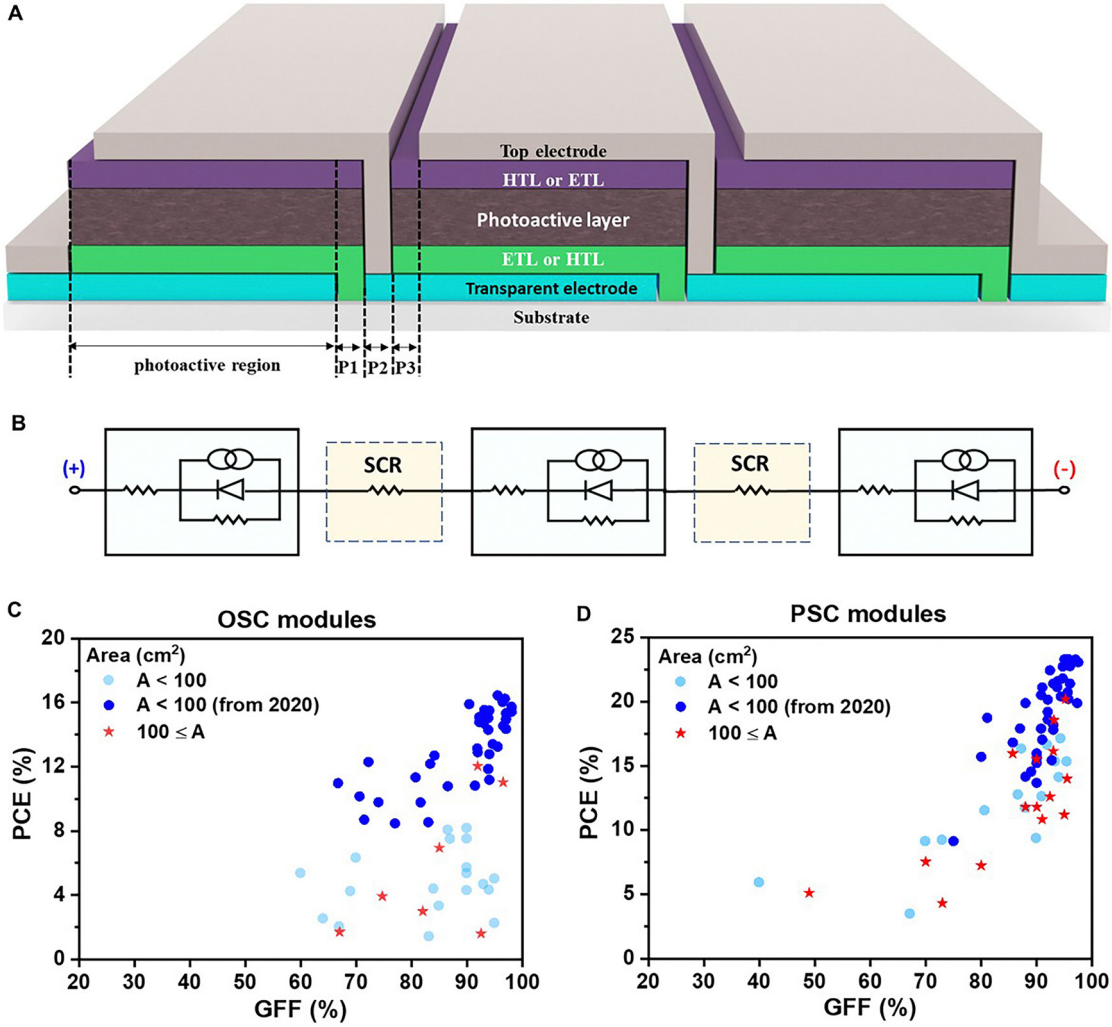

Fig. 1 Monolithic module structure and representative OSC and PSC modules. (A) Schematic monolithic OSC and PSC modules and (B) corresponding equivalent circuits. PCE *vs.* GFF plots of representative (C) OSC and (D) PSC modules.

challenging to implement real-time adjustments when the module area is scaled up.

In contrast, post-patterning involves the definition of interconnection lines after the entire device stack is deposited. P1 patterning is usually conducted *via* laser scribing or wet etching processes, whereas P2 and P3 patterning are the key points of distinction between pre-patterning and post-patterning approaches. Post-patterning methods typically include mechanical and laser scribing techniques, each of which possesses distinct advantages and limitations. Mechanical scribing, which involves solvent-soaked swabs or blades, has proven effective for small-area modules, but resolution and scaling limitations hinder its performance in cases with larger formats.[67–71] Automated mechanical approaches have demonstrated GFF values above 90%, but careful optimization steps are required to avoid damaging the underlying layers and compromising the uniformity of the constructed module.[68,69] Laser scribing, which is the dominant technique for high-efficiency modules, enables the rapid, high-resolution formation of series connections, dramatically increasing the GFF above 90%.[47,72,73] Additionally, its mask-free and noncontact nature makes it compatible with both rigid and flexible substrates. Although post-patterning methods such as mechanical and laser scribing techniques allow delicate patterning processes to achieve high GFFs, additional costs are incurred for the installation and operation steps, and some concerns related to defect creation and layer damage are present.

3. OSC modules

The advancement of OSC modules reflects parallel progress in photoactive materials and scalable fabrication techniques. The development trend commenced with foundational discoveries, such as those concerning conductive polymers and the introduction of the bulk heterojunction (BHJ) concept in 1995, which first enabled efficient charge separation schemes.[74] Early module studies, which were pioneered by research groups such as F.C. Krebs, focused on adapting printing technologies, including slot-die coating, screen printing, and inkjet printing, for the first generation of photoactive systems such as P3HT:PCBM.[38,56,75–78]

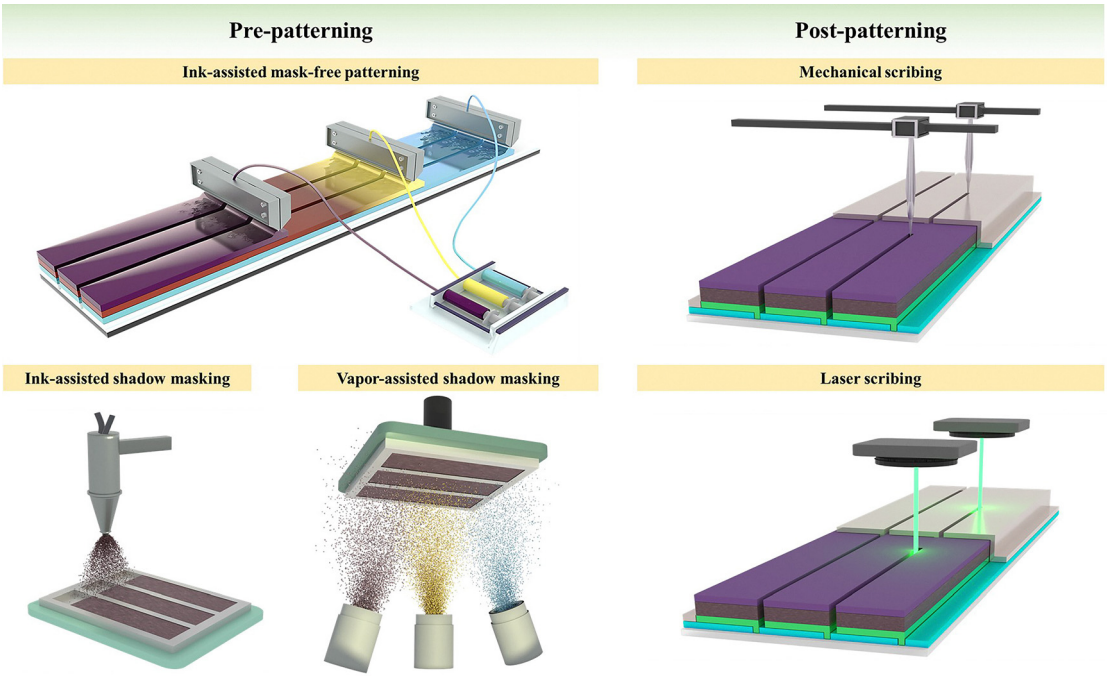

Fig. 2 Schematic of the pre-patterning and post-patterning processes for OSC and PSC modules. Pre-patterning is composed of ink-assisted shadow mask-free patterning, ink-assisted shadow masking, and vapor-assisted shadow masking processes. Post-patterning comprises mechanical and laser scribing techniques.

While these efforts established the viability of large-area printed OSCs, the inherent limitations of the utilized materials restricted the efficiency of the developed modules to approximately 3%. Significant advances occurred with the development of low-bandgap donor polymers (*e.g.*, PTB7-Th) combined with fullerene acceptors, which increased the efficiency of laboratory-scale cells beyond 10% by 2015.[79,80] This material improvement, coupled with advances in processing, allowed the PCEs of single-junction OSC modules to surpass 5% from 2016 onward.[48,81]

The most transformative breakthrough, however, has been the advent of nonfullerene acceptors (NFAs).[82–84] High-performance NFAs, particularly A–D–A-type molecules such as the Y6 family, have revolutionized the field by offering superior near-infrared absorption and energy level alignment capabilities.[84,85] This material revolution has enabled single-junction lab cells to exceed the 20% efficiency threshold.[86–90] When integrated with optimized printing processes, these advanced material systems have driven the PCEs of reported academic modules to exceed 16% (Fig. 1C and Table 1).[91,92] Nevertheless, significant challenges remain. A performance gap persists, with the certified record for large-area OSC modules (>200 cm^2) currently sitting at 14.5%.[40] Furthermore, the ability to achieve state-of-the-art performance often relies on costly patterning processes such as laser scribing, highlighting the ongoing need for novel, low-cost, and scalable fabrication strategies to fully realize the commercial potential of OSC module technology.

3.1 Monolithic OSC modules based on mechanical patterning

In the early development stages of OSC modules, before the widespread availability of advanced printing and laser tools, researchers relied on manual mechanical patterning methods to create series-connected monolithic devices.[93,94] For a conventional device architecture, where electrons are collected at the top electrode and holes are located at the bottom, this typically involves using a knife edge or a swab soaked in an organic solvent to selectively remove the photoactive layer and the underlying PEDOT:PSS HTL, thereby exposing the bottom electrode for interconnection. While functional, these manual methods suffer from poor resolutions, which limits the GFF to less than 70% and severely constrains the overall efficiency of the constructed modules.

To overcome these limitations, the field has progressed to automated mechanical scribing, employing fine metal needles, blades, or even threads mounted on precision equipment.[68,69,95,96] A typical strategy involves the sequential deposition of the HTL, the photoactive layer, and the ETL onto a prepatterned P1 substrate, followed by mechanical scribing of the P2 line. After the top electrode is deposited, the P3 line is then scribed to achieve electrical isolation and complete the series connection. The structure of an OSC module based on P3HT:PCBM, one of the representative early photoactive layers, is described in Fig. 3A. Although mechanical scribing may cause damage, J.G. Tait *et al.* demonstrated that this technique can achieve fine-stripe P2 patterning below 50 μm, which is finer than the aerosol pre-patterning approach utilized in 2016 (Fig. 3B).[95]

S. Dong *et al.* demonstrated the use of a mechanical scribing machine under ambient conditions to form P2 and P3 lines, achieving a GFF of 86.6% in PTB7:$PC_{71}BM$-based devices.[96] In this work, the incorporation of an NDI-PFNBr-doped interfacial ZnO cathode layer enhanced the conductivity of the ETL and

Table 1 Representative papers reporting module PCEs calculated on the aperture module area, explicitly considering GFF in OSC modules from 2010 to 2025

Year	Device structure	P1	P2	P3	GFF (%)	Module PCE (%)	Module area (cm^2)	Ref.
2010	PET/ITO/ZnO/P3HT:PCBM/PEDOT:PSS/Ag	—	Slot-die coating (R2R)	Screen printing (R2R)	67	2.00	96	S1
						1.69	360	
2011	Glass/Cr/Al/Cr/P3HT:PCBM/PEDOT:PSS/Au		Slot-die coating	—	64.07	2.5	13.2	S2
2014	Glass/ITO/ZnO/P3HT:Si-PCPDTBT:$PC_{60}BM$/PEDOT:PSS/ZnO/P3HT:Si-PCPDTBT:$PC_{60}BM$/PEDOT:PSS/Ag	Laser scribing	Laser scribing	Laser scribing	85	3.30	1.1	S3
2014	IMI/ZnO/OPV12:$PC_{60}BM$/PEDOT:PSS/ZnO/pDPP5T-2:$PC_{70}BM$/MoO3/Ag	Laser scribing	Laser scribing	Laser scribing	90	5.70	0.1	S4
2015	Glass/ITO/AZO/P3HT:PCBM/PEDOT:PSS/Ag	Laser scribing	Laser scribing	Laser scribing	83.2	1.38	1.15	S5
2015	Glass/ITO/PEDOT:PSS/pDPP5T-2:$PC_{60}BM$/ZnO/AgNWs	Laser scribing	Laser scribing	Laser scribing	95	2.22[a]	67.4[a]	S6
2015	Glass/ITO/PEDOT:PSS/POD2T-DTBT:$PC_{70}BM$/Al	—	Mechanical scribing	—	82	2.98[a]	131.7[a]	S7
2015	Glass/ITO/PEDOT:PSS/PBDT-TFQ:$PC_{71}BM$/Ca/Al	Laser scribing	Laser scribing	Laser scribing	90	4.27	5.33[a]	S8
2015	PET/ITO/ZnO/P3HT:PCBM/PEDOT:PSS/Ag grids	Laser scribing	Laser scribing	Inkjet printing	92.5	1.59	156	S9
2016	PET/ITO/Ag/ITO/ZnO/PBTZT-*stat*-BDTT8:PCBM/TCA/AgNWs	Laser scribing	Laser scribing	Laser scribing	90	5.33	0.3	S10
2016	Glass/ITO/PEDOT:PSS/PCDTBT:$PC_{70}BM$/ZnO NPs/PEDOT:PSS/Nafion/Si-PCPDTBT:$PC_{70}BM$/LiF/Al	Laser scribing	Laser scribing	Mechanical scribing	95	5.0	1.33	S11
2016	Glass/ITO/ZnO/PTB7-Th:$PC_{70}BM$/MoO_3/Ag	Chemical etching	Slot-die coating	Mask patterning	90	7.5	4.15	S12
2016	Glass/ITO/p-NHT18/n-C_{60}/C_{60}/HDR14:C_{60}/p-NHT18/n-C_{60}/C_{60}/HDR14:C_{60}/p-NHT18/Ag	Laser scribing	Laser scribing	Laser scribing	94	4.3	64	S13
2017	Glass/ITO/ZnO/PBTZT-*stat*-BDTT-8:PTB7-th:$PC_{70}BM$/MoO_x/Ag	Laser scribing	Laser scribing	Laser scribing	90	8.16	0.1	S14
2018	Glass/ITO/ZnO/PBDB-T:ITIC/MoO_3/Ag	Laser scribing	3D printing (Maobi)	—	70	6.3	18	S15
2018	Glass/ITO/ZnO/PTB7:$PC_{70}BM$/CPP105D/PEDOT:PSS/ZnO/PTB7:$PC_{70}BM$/MoO_3/Ag	—	Mechanical scribing	—	84	4.37[a]	28.57[a]	S16
2018	Glass/ITO/ZnO/P3HT:IDTBR/PEDOT:PSS/Ag	Laser scribing	Laser scribing	Laser scribing	93	4.65[a]	64[a]	S17
2018	Glass/ITO/ZnO/PBTIBTT:ITIC-F/MoO_3/Ag	Laser scribing	Laser scribing	Laser scribing	87	7.48	4.0	S18
2019	Glass/ITO/NDI-PFNBr@ZnO/PTB6-Th:$PC_{71}BM$/MoO_3/Ag	—	Mechanical scribing	Mechanical scribing	86.6	8.05	16	S19
2019	PET/ITO/hc-PEDOT:PSS/ZnO/PBDB-T:ITIC/MoO_3/Ag	—	—	—	60	5.34[a]	25	S20
2019	Glass/Al/PF2:$PC_{71}BM$/PEDOT:PSS/Ag grid	—	Mechanical patterning	Mask patterning	69	4.21	95.65[a]	S21
2019	PET/ITO/ZnO/SMD2:ITIC-Th/WO_x/Ag		Slot-die coating	Screen printing	74.7	3.92[a]	107.1[a]	S22
2020	Glass/ITO/PEDOT:PSS/PM6/Y6/PNDIT-F3N-Br/Ag	—	Mechanical scribing	Mask patterning	91.4	10.84	12.6	S23
2020	Glass/Nabil/ZnO/PTB7-Th:EH-IDTBR/MoO_3/Ag	Chemical etching	Mechanical patterning	Mask patterning	85	6.95[a]	100	S24
2020	Glass/ITO/PEDOT:PSS/PM6:DTY6/PNDIT-F3NBr/Ag		Mechanical scribing	Mask patterning	70.6	10.17[a]	25.5[a]	S25
2020	Glass/Ag grid/PH1000/ZnO/PTB7-Th:COi8DFIC:PCBM/MoO_3/Ag	—	—	—	77	8.48	12.99[a]	S26
2021	Glass/ITO/ZnO/PV2300:PV-A3:PCBM/HTL-X/Ag	Laser scribing	Laser scribing	Laser scribing	83	8.55[a]	39.28[a]	S27
2021	Glass/ITO/ZnO/PM6:Y6:ITIC:$PC_{71}BM$/MoO_3/Ag	Laser scribing	Laser scribing	Laser scribing	95.5	13.25	19.34	S28
2021	Glass/ITO/ZnO/PM6:BTP-4Cl-12/h-HTL/Ag	—	—	—	81.6	9.79[a]	5.76[a]	S29
2021	PET/Ag grid/PBDB-T-2F:Y6:$PC_{71}BM$/MoO_3/Ag	—	—	—	74	9.8	54	S30
2021	Glass/ITO/PEI-Zn/PM6:BTP-eC9/MoO_3/Ag	Laser scribing	Laser scribing	Laser scribing	80.7	11.35	31.24[a]	S31
2022	Glass/ITO/PEDOT:PSS/PM6:BO-4Cl:m-BTP-PhC6/Bis-FIMG/Ag.	Laser scribing	Laser scribing	Laser scribing	96.4	16.04	19.3	S32
2022	Glass/ITO/PEDOT:PSS/PM6:BTP-Bo-4Cl/Bis-FIMG/Ag.	Laser scribing	Laser scribing	Laser scribing	97	14.35	19.3	S33
2022	Glass/ITO/ZnO/PBDB-T-2F:N3:P(NDI2OD-T2)/MoO_3/Ag	—	Laser scribing	Mechanical scribing	91.82	13.14	22.44	S34
2022	PET/Ag/PEI-Zn/PM6:BTB-Ec9/PEDOT:F/AgNWs-polymer	Mask patterning	Laser scribing	Laser scribing	72.2	12.3	21	S35
2022	Glass/ITO/PEDOT:PSS/PM6/T8/PNDIT-F3N/Ag	—	Mechanical patterning	Mask patterning	83.33[a]	12.17[a]	9	S36
2023	Glass/Ag grid/PH1000/ZnO/PM6:Qx-1/MoO_3/Ag	—	Slot-die coating (R2R)	Mask patterning	71.43[a]	8.71[a]	42[a]	S37
2023	Glass/ITO/ZnO/PBQx-TF:eC9-2Cl/MoO_3/Ag	Laser scribing	Mechanical scribing	Mechanical scribing	92.2	15.1	23.6	S38
2023	Glass/ITO/ZnO/PB2:FTCC-Br:BTP-eC9/MoO_3/Ag	Laser scribing	Mechanical scribing	Mechanical scribing	93.8	14.3	54	S39
2023	Glass/ITO/PEDOT:PSS/PM6:Y6:$PC_{70}BM$/BCP/Ag	Chemical etching	Mechanical patterning	Mask patterning	86.5	10.8	10	S40
2023	Glass/ITO/PEDOT:PSS/PM6:L8-BO:BTP-S8:BTP-S2/Bis-FIMG/Ag	Laser scribing	Laser scribing	Laser scribing	94	12.78	72.25	S41
2023	Glass/ITO/PEDOT:PSS/PM6/Y6/ZnO/Al	Laser scribing	Laser scribing	Laser scribing	93.8	11.86[a]	30.72[a]	S42
2023	Glass/ITO/ZnO/PTVT-T:GS60/MoO_x/Ag	—	Mechanical scribing	Mechanical scribing	94	11.2	22.1	S43
2023	Glass/ITO/PEDOT:PSS/PBDB-TFCl:D18-Cl:PY-IT/PDINN/Ag	—	Mechanical scribing	Mask patterning	84.1	12.7	36.2	S44
2023	Glass/ITO/PEDOT:PSS/PM6:PBQx-TCl:PY-IT/PDINN/Ag	Laser scribing	Laser scribing	Laser scribing	96.8	16.26	19.3	S45
2024	Glass/ITO/PEDOT:PSS:NiO_x/PBQx-TCl:eC9-2Cl/NDI-Ph/Ag	—	Mechanical scribing	Mechanical scribing	94	15.52	23.60	S46
2024	Glass/ITO/PEDOT:PSS/PM6:BTP-eC9:Qx-5Cl/PDINN/Ag	Laser scribing	Laser scribing	Laser scribing	94.6	13.41[a]	18.29[a]	S47

Table 1 (*continued*)

Year	Device structure	P1	P2	P3	GFF (%)	Module PCE (%)	Module area (cm^2)	Ref.
2024	Glass/ITO/ZnO/PM6:L8-BO(HU-DT):$PC_{70}BM/MoO_3$/Ag	Laser scribing	Laser scribing	Laser scribing	96.5	11.04	205.99	S48
2024	Glass/ITO/PEDOT:PSS/PM6:D18:BTP-eC9/C_{60}/BCP/Ag	Laser scribing	Laser scribing	Laser scribing	93.1	15.55[a]	16.80	S49
2024	Glass/ITO/ZnO/PM6:Y6-C12:PCBM/PEDOT-F/Ag	Laser scribing	Laser scribing	Laser scribing	96.5	14.55	204.11	S50
2024	Glass/ITO/2PACz/PM6:BO-4Cl/PFN-Br/Ag	Laser scribing	Laser scribing	Laser scribing	98	15.74	19.31	S51
2024	Glass/ITO/ZnO/PM6:L8-BO/MoO_3/Ag	Laser scribing	Laser scribing	Laser scribing	98	15.43	11.30	S52
2024	Glass/AgNWs/PEI-Zn/PM6:BTP-eC9:$PC_{71}BM/MoO_3$/Ag	—	Laser scribing	—	91.9	12.90[a]	44.61[a]	S53
						12.04[a]	402.61[a]	
2024	Glass/ITO/4PADCB/D18:L8-BO/PNDIT-F3N/Ag	Laser scribing	Laser scribing	Laser scribing	97	14.98[a]	19.90[a]	S54
2024	Glass/ITO/AZO/PM6:D18:L8-BO/MoO_3/Ag	Laser scribing	Laser scribing	Laser scribing	92.2	14.78[a]	16.96[a]	S55
2024	Glass/ITO/PEDOT:PSS/PM6/BTP-eC9/ZnO/Al	Laser scribing	Laser scribing	Laser scribing	93.8	15.04[a]	30.72[a]	S56
2024	Glass/ITO/PEDOT:PSS/PBQ_x-TF:Ec9-2Cl/PDI-Ph/Ag	Laser scribing	Mechanical scribing	Mechanical scribing	93.04[a]	14.7	23.6	S57
2024	Glass/ITO/PEDOT:PSS/PM6:L8-BO/PDINN/Ag	Laser scribing	Laser scribing	Laser scribing	98	15.70[a]	11.94[a]	S58
2025	Glass/ITO/PEDOT:PSS/PM6:L8-BO/Bis-FIMG/Ag	Laser scribing	Laser scribing	Laser scribing	97	14.94	19.31	S59
2025	Glass/ITO/PEDOT:PSS/PM6:PYIT:L8BO/PNDIT-F3N/Ag	Laser scribing	Laser scribing	Laser scribing	90.37	15.91[a]	20.36[a]	S60
2025	Glass/ITO/PEDOT:PSS/PM6:HD-1:BO-4Cl/PNDIT-F3N/Ag	—	Mechanical scribing	Mask patterning	66.7	10.99[a]	20.24[a]	S61
2025	Glass/ITO/$InCl_3$/PM6:BTP-eC9/C60/BCP/Ag	Laser scribing	Laser scribing	Laser scribing	95.5	16.45	15.6	S62

[a] Calculated values from the corresponding papers.

improved the wettability of blade-coated photoactive films. This refined technique has enabled significant performance gains. Pushing the boundaries of the GFF, R. Sun *et al.* employed a thread-wiping method for P2 line formation, yielding a GFF greater than 90% in the PM6:Y6 OSC module (Fig. 3C and D).[68] Notably, J. Hou's group implemented mechanical scribing for the fabrication of printed OSC modules, reporting a GFF of 94% and module PCEs of 15.52% (23.6 cm^2) and 13.00% (32.52 cm^2) (Fig. 3E and F).[69]

Despite the advantages of mechanical scribing, including its low equipment cost, operational simplicity, and potential high-throughput processing capabilities, its applications remain limited compared with those of laser-based techniques. Owing to its inherently physical nature, mechanical scribing poses challenges with respect to achieving high resolutions at large scales and exhibits persistent risks of damaging the underlying layers. These factors can compromise the yields and long-term stability of devices, representing the fundamental tradeoffs of this patterning approach.

3.2 Monolithic OSC modules based on printed patterns

As the development of OSCs predates that of PSCs, the concept of fabricating modules at a large scale using printing processes was first pioneered in the OSC field.[37,38,56,97–99] Printing technologies constitute a cornerstone of this effort, providing a pathway to low-cost, high-throughput manufacturing through additive patterning. In contrast with subtractive methods such as scribing, which remove pre-deposited material, printing enables the direct deposition of functional inks only where needed, thereby minimizing material waste and potentially integrating the deposition and patterning procedures into a single step. Printing methods, including slot-die coating, screen printing, inkjet printing, gravure printing, and spray coating, have been extensively investigated, with each approach presenting a distinct balance among its resolution, throughput, and material compatibility.

A comprehensive exploration of roll-to-roll compatible printing technologies conducted by F.C. Krebs and his coworkers demonstrated the viability of fully printed, roll-to-roll fabricated OSC modules.[38,56,75–78,97,100–102] In their monumental works, emphasis was placed on the deposition of functional layers and the patterning strategies required for fabricating monolithic modules.[56] Slot-die coating was employed to deposit uniform zinc oxide (ZnO) nanoparticle layers, P3HT:PCBM photoactive layers, and PEDOT:PSS layers in stripe patterns aligned with the prepatterned ITO substrate (Fig. 4A). The monolithic module design featured multiple serially connected subcells, which were established by precisely patterning the bottom ITO electrode *via* etching (P1) and the top silver electrode *via* screen printing (P3) (Fig. 4B). While this research provided critical insights into scalable roll-to-roll (R2R) fabrication techniques, it also revealed a key challenge, namely, significant aperture losses, which could reach 50%, thus fundamentally limiting the efficiency of the constructed module. To address this issue, the relationship between the subcell geometry and performance was systematically investigated. As shown in Fig. 4C, this study revealed that 13-mm-wide stripes with a 2-mm interconnection gap

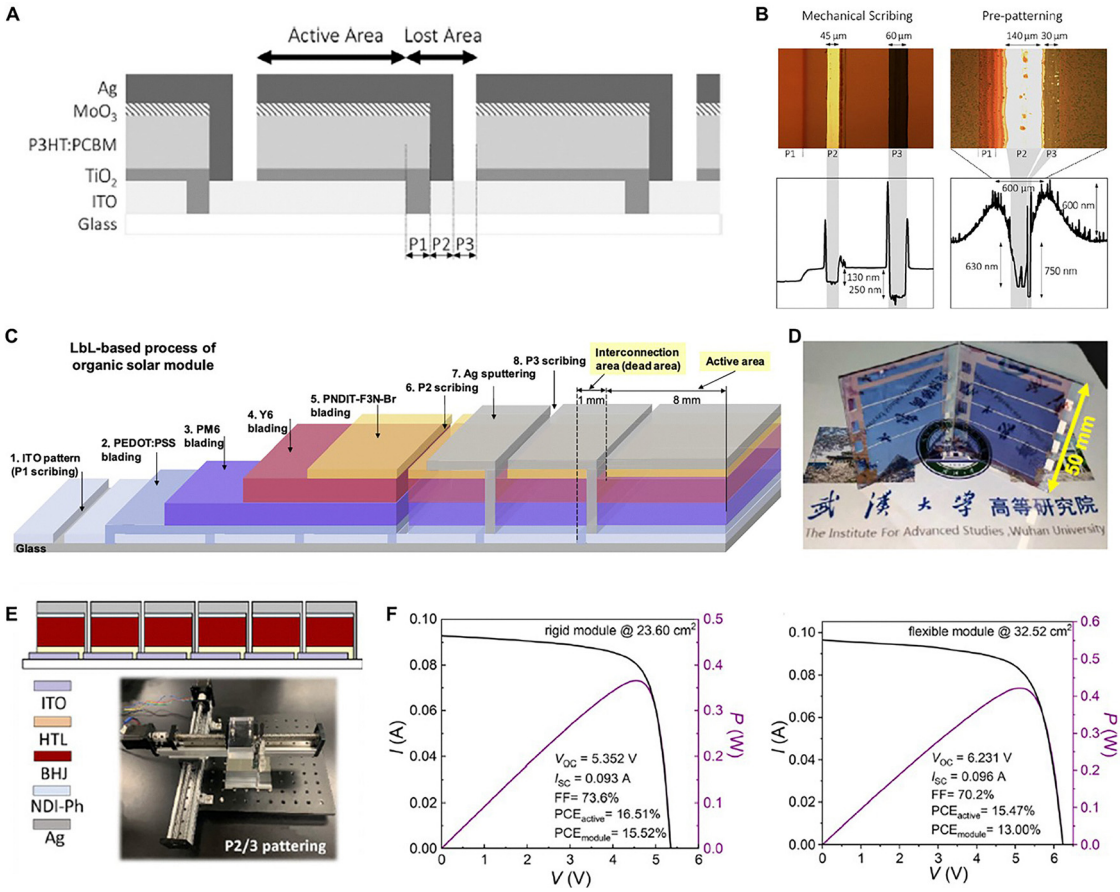

Fig. 3 OSC modules based on mechanical patterning. (A) Schematic representation of the archetypal organic photovoltaic module. Three patterning steps are involved: P1 separates the bottom electrode between individual cells, P2 removes the active layer to allow contact between the anode and cathode of adjacent cells, and P3 separates the top electrodes of adjacent cells. (B) Optical micrographs and profilometer scans of mechanically scribed (left) and aerosol jet pre-patterned (right) layers, after completion of the entire device stack including the P1, P2, and P3 steps. Note that spacing between P1, P2, and P3 is included to increase production yield. The P1 pattern is difficult to observe in the pre-patterning case due to its falling in the material pile-up to either side of the pre-patterning line. Reproduced with permission from Tait *et al.*,[95] Copyright 2016 Elsevier. (C) Process flow diagram of the layer by layer (LbL) based process for large-area solar modules. (D) Image of solar modules based on LbL PM6/Y6 film with an active area of 11.52 cm^2 and an optimal GFF of 91.4%. Reproduced with permission from Sun *et al.*,[68] Copyright 2020 Elsevier. (E) Device structure diagram of OSC modules. (F) *J*–*V* and *P*–*V* curves of rigid (left) and flexible (right) large-area OSC modules under AM 1.5G, 100 mW cm^{-2} illumination. Reproduced with permission from Wang *et al.*,[69] Copyright 2020 Royal Society of Chemistry.

offered an optimal balance between minimizing the induced geometric losses (maximizing the GFF) and mitigating the resistive losses caused by the ITO. Y.-F. Shen *et al.* also successfully demonstrated series connected flexible OSC modules using a slot-die coating without a P2 laser patterning process, achieving a calculated GFF of 71.4% (Fig. 4D and E).[103]

The primary advantage of this fully printed approach remains its potential for low-cost, high-throughput production.[99,104] However, the resolution limits of printing techniques often make it difficult to achieve the fine patterning that is required for attaining a very high GFF. Consequently, the field has largely evolved toward a hybrid fabrication strategy. In this now-common approach, printing and coating methods are used to deposit large-area functional layers, while the critical P2 interconnection line is selectively patterned using high-precision laser scribing to maximize both the performance and yield.[58–60,105–107] When additional post-patterning steps such as mechanical or laser scribing are employed, material degradation and substrate damage may occur, and the need for extra tooling increases the incurred processing costs.[108] Accordingly, a module fabrication route that relies exclusively on printing is expected to provide technical and economic advantages, provided that high-quality patterning can be achieved. Patterned printing processes encounter two overarching challenges, namely, (i) uniform deposition over large areas and (ii) high-precision pattern definition, both of which are critical for achieving consistent module performance.

Large-area film nonuniformity arises from fluid dynamics effects and surface tension gradients, leading to edge thickening (edge-bead/edge effects) in stripe-shaped meniscus coatings and coffee-ring deposition during inkjet and spray processes.[109–111] The edge effect can be mitigated through surface-energy modification (substrate treatment), solvent-system engineering (cosolvents/boiling-point tuning), coating parameter optimization (the flow rate, web speed, and gap), and controlled ambient conditions

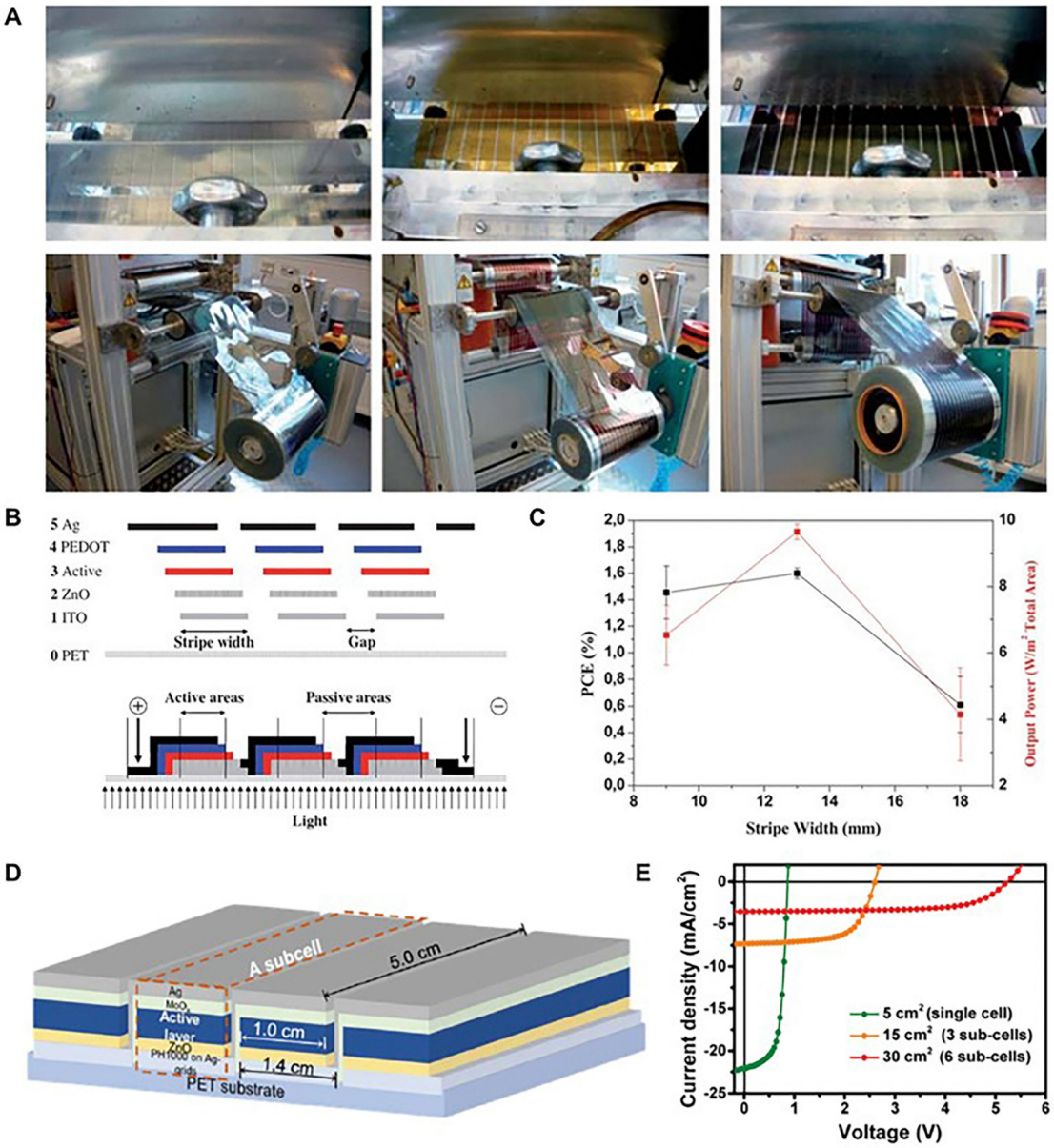

Fig. 4 OSC modules based on the printed patterning process. (A) The slot-die coating of ZnO nanoparticles (left), P3HT:PCBM (middle) and PEDOT:PSS (right). The wet films are shown above and the corresponding dried films are shown below. (B) Serially connected OSC modules with a slight shift (C) the PCE and power that can be extracted from a module aperture as a function of stripe. Reproduced with permission from Krebs *et al.*,[56] Copyright 2010 Royal Society of Chemistry. (D) Scheme of module structures. (E) *J*–*V* curves of the large-area device and modules. Reproduced with permission from Shen *et al.*,[103] Copyright 2023 Wiley-VCH GmbH.

(temperature and humidity), thereby enabling a uniform thickness up to the substrate edges.[112–114] The coffee-ring effect can be suppressed by tailoring evaporation kinetics, compensating for Marangoni flows, increasing the ink viscosity (polymer/additive), and adjusting the wettability of the substrate to maintain a uniform solute distribution during the drying process.[115–117] With respect to patterning precision, the specific requirements vary by printing modality; however, the common principles involve robust mask or digital pattern designs, accurate droplet/meniscus placements and registrations, and process windows that ensure selective deposition only at the intended locations.

3.3 Monolithic OSC modules utilizing laser scribing

The laser scribing technique has emerged as a preferred module patterning approach because of its high precision, high speed, and noncontact nature.[73,107] Unlike mechanical scribing, which involves direct contact with the substrate and can induce physical damage or wear, laser scribing employs focused laser pulses to ablate specific regions of the target material. The laser energy is absorbed by the target layer, causing rapid localized heating and material removal through photothermal and photomechanical processes such as melting, vaporization, and, at higher fluences, explosive boiling or stress-assisted delamination.

From a fundamental perspective, when photons are absorbed by an organic semiconductor or an electrode layer, they are converted into heat within an ultrashort time window. With respect to nanosecond pulses, thermal diffusion is predominant, often resulting in molten rims or heat-affected zones, whereas femtosecond or picosecond pulses confine the energy deposition process before thermal relaxation occurs, enabling the removal of material primarily through nonequilibrium ablation and mechanical stress release.[73,118] This process can be tuned by adjusting the laser wavelength, pulse duration, and fluence to match the optical absorption and thermal conductivity of each layer in the OSC stack, ensuring selective removal without damaging the underlying layers.

One of the main advantages of laser scribing for OSC modules is the ability to achieve very narrow and well-defined interconnection lines (P1, P2, P3), which minimize the dead area and thereby increase the GFF. This is particularly crucial, as the PCEs of OSC modules exceed 10%, and further module efficiency gains rely strongly on maximizing the active area.[119–121] Moreover, the noncontact and mask-free nature of laser scribing makes it compatible with roll-to-roll and large-area printing processes, aligning well with the low-cost and flexible manufacturing concepts of OSC technology.[48,118] However, several technical challenges remain. First, the optical absorption spectra of organic semiconductors vary widely depending on their donor–acceptor systems, requiring precise wavelength selection processes for achieving effective ablation. Second, the relatively low thermal stability of organic materials increases the risk of chemical decomposition or residue formation at the scribe edges, which can introduce leakage pathways or contact resistance. Finally, optimizing the overlap ratio, repetition rate, and scanning speed is essential for balancing complete material removal with thermal damage minimization. Addressing these issues is the key to translating the intrinsic advantages of laser scribing into scalable and reliable OSC module fabrication procedures.

Prior to the adoption of laser scribing in OSCs, the GFFs of modules generally remained below 70% because of the resolution limits of conventional etching and printing methods. Laser scribing was introduced as a high-precision tool to overcome this barrier. P. Kubis *et al.* first demonstrated laser-scribed OSC modules formed using femtosecond laser pulses (<350 fs).[122] While the PCE of these modules was modest at 1.38% because of the limitations of the photoactive materials that were available at the time, this study was significant for achieving a GFF of 83% and demonstrating the potential to reach GFF values higher than 98%. Following this proof-of-concept study, G. D. Spyropoulos *et al.* applied laser scribing to fabricate flexible, roll-to-roll compatible tandem OSC modules.[123] The high precision of the utilized laser enabled the P2 interconnection width to be dramatically reduced from 325 μm to just 25 μm. As a direct result, the GFF of the module increased from 80% to 94%, increasing the PCE from 5.38% to 5.70% (Fig. 5A). Crucially, the well-defined scribe did not introduce significant parasitic resistance, as the average series resistance of the module remained comparable to that of a single cell (Fig. 5B). Furthermore, the flexible modules demonstrated excellent mechanical robustness; bending tests indicated that the observed performance degradation was caused primarily by the intrinsic failure of the

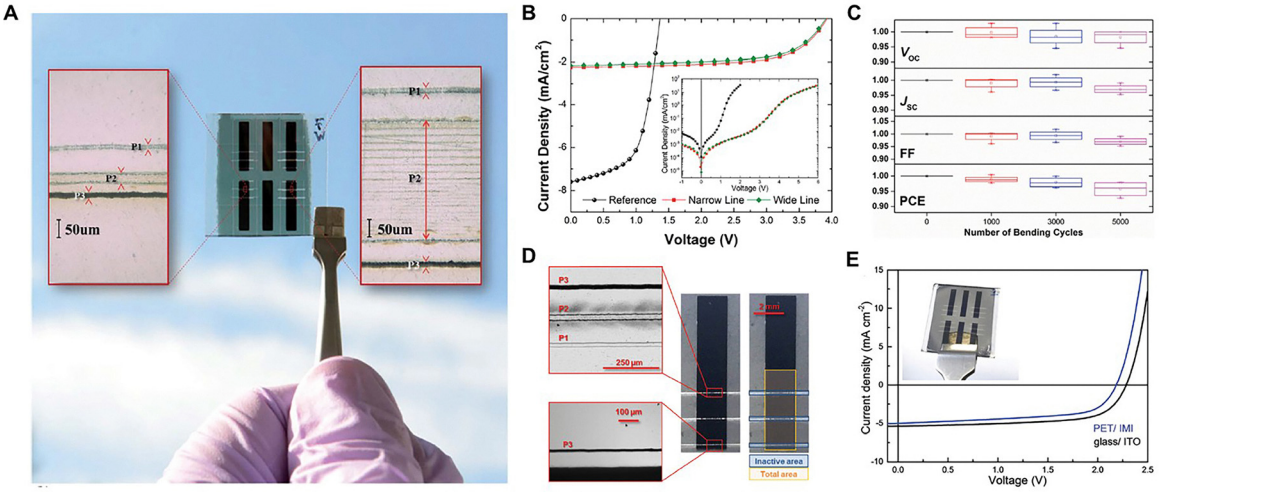

Fig. 5 OSC modules based on the laser scribing technique. (A) Photograph of one of the 9 substrates carrying two reference single tandem cells (center) and two pairs of tandem modules (left and right), with narrow (~25 μm, left) and wide (~325 μm, right) P2 line patterning. The insets present top views from an optical microscope displaying the lines P1–P3. The wide P2 line was realized by laser hatching (scanning many single lines parallel to each other). (B) *J*–*V* characteristics of reference tandem cells (black spheres) and tandem modules with narrow (~25 μm, red squares) and wide (~325 μm, green diamonds) P2 lines under illumination. (C) Normalized device characteristics of flexible tandem modules after 1000, 3000, and 5000 bending cycles. Reproduced with permission from Spyropoulos *et al.*,[123] Copyright 2014 Royal Society of Chemistry. (D) Optical micrographs of a solar module with three interconnected subcells. The insets on the left represent optical magnifications of the interconnection region, where the laser lines P1, P2 and P3 are highlighted. The photo-inactive (dead area, blue) and total area (yellow) of the module are highlighted as well. (E) *J*–*V* curves of flexible and rigid modules prepared using the ternary blend PBTZT-*stat*-BDTT-8 : PTB7-th : $PC_{70}BM$ (0.5 : 0.5 : 1.5) as the photoactive layer. The inset shows a photograph of a glass/ITO substrate including 4 modules and 2 reference cells (center). Reproduced with permission from Gasparini *et al.*,[124] Copyright 2017 Royal Society of Chemistry.

functional layers rather than the laser-scribed interconnections (Fig. 5C). This technique has also been successfully applied to state-of-the-art material systems. N. Gasparini *et al.* used laser scribing to narrow the inactive area in ternary blended OSC modules, achieving a GFF of 90% (Fig. 5D).[124] This led to module PCEs of 8.16% on glass and 6.83% on flexible substrates based on a PET/ITO–Ag–ITO structure (Fig. 5E).

While OSC modules employing laser scribing have reported relatively high PCEs compared with those of contemporaneous unit devices, many early demonstrations were limited to small active areas of approximately 1 cm^2 and did not incorporate printing-based deposition.[87–89,91] As the field has matured, laser scribing has become a widely adopted strategy for conducting line patterning during OSC module fabrication, enabling the development of large-area, nonfullerene based modules. Since 2022, highly efficient OSC modules approaching 15% PCEs have been realized by employing laser-defined series interconnections.[121,125] A representative study performed by Z. Liu *et al.* engineered gradient-based vertical phase separation in the BHJ photoactive layer and implemented laser scribing for the P1, P2, and P3 processes, as described in Fig. 6A.[126] By introducing a volatile solid additive through layer-by-layer doctor blade coating processes, the OSC module achieved a PCE of 16.04% on a 28.82 cm^2 active area with a GFF of 93.8%. Given the complex multilayer stacks of monolithic OSC modules, laser patterning must be both selective and precise, avoiding causing collateral damage to the adjacent regions. Additionally, these results imply that the difference between the PCEs of a small-area unit cell and a large-area OSC module remarkably decreases to 12.8%.

Z. Jin *et al.* successfully scaled up laboratory unit cells to large-area OSC modules through laser scribing-based P1, P2, and P3 processes, featuring an inactive area of 250 μm at each subcell, resulting in a GFF of 95.5% (Fig. 6B and C).[91] As a result, the $InCl_3$ based module achieved uniform distribution of PCEs and a remarkable module PCE of 16.5% at the aperture area of 15.6 cm^2 with an open circuit voltage (V_{OC}) of 6.01 V, a short circuit current density (J_{SC}) of 3.80 mA cm^{-2}, and a fill factor (FF) of 72.3% (Fig. 6D and E). R. Basu *et al.* uniformly coated the stacked layers in OSCs, resulting in very homogenous PCE distributions over a 165 × 165 mm^2 substrate composed of 216 small devices (Fig. 6F and G).[40] According to a simulation of PCE losses (summarized in Fig. 6H), the lowest overall losses were determined for 38 subcells with an active area width of 3.63 mm. Finally, OSC modules (204 cm^2) fabricated by

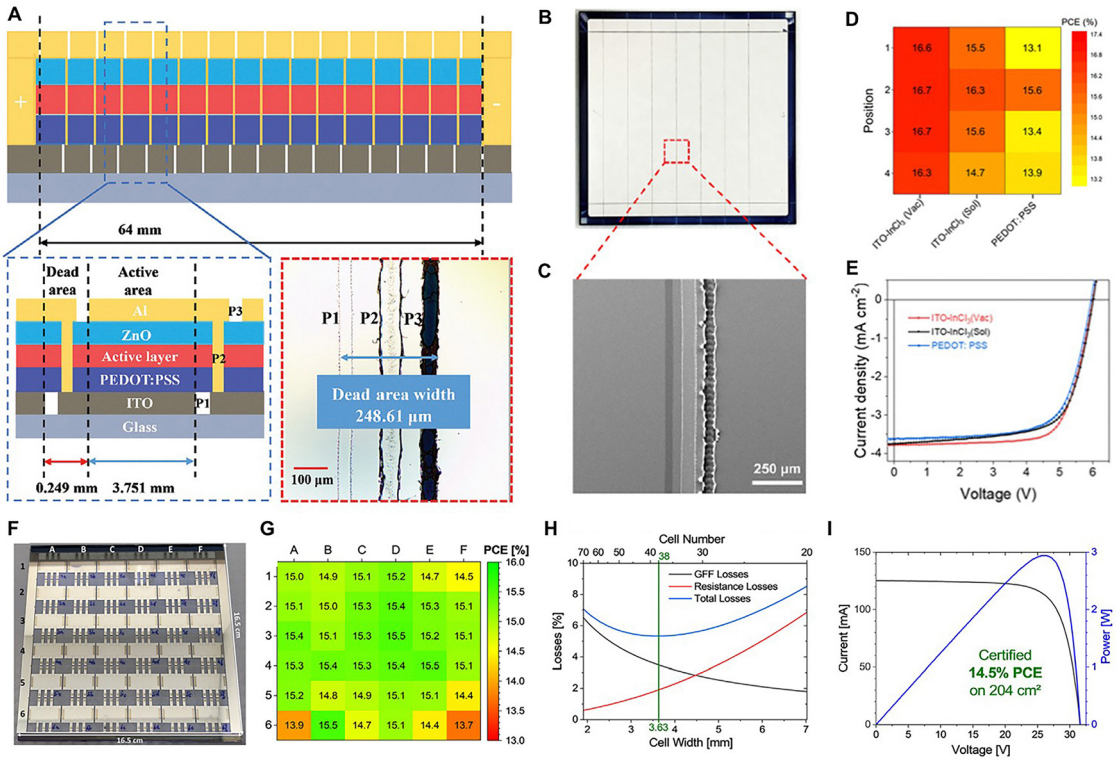

Fig. 6 OSC modules based on the laser scribing technique. (A) Schematic of the large-area blade-coated OSC module consisting of 16 serially connected subcells and a photograph depicting the dead zone width between subcells. Reproduced with permission from Liu *et al.*,[126] Copyright 2025 Wiley-VCH GmbH. (B) Photograph of an organic solar module with seven tandem cell stripes and a total aperture area of 15.6 cm^2. (C) SEM image of scribing lines indicating the P1–P3 interconnections. (D) PCE distribution of each submodule (3.9 cm^2) on PEDOT:PSS, $InCl_3$ (Sol), and $InCl_3$ (Vac)-based solar modules (15.6 cm^2). (E) *J*–*V* characteristics of PEDOT:PSS, ITO–$InCl_3$ (Sol), and ITO–$InCl_3$ (Vac) based modules with an aperture area of 15.6 cm^2. Reproduced with permission from Jin *et al.*,[91] Copyright 2025 Royal Society of Chemistry. (F) Photograph of a 165 × 165 mm^2 substrate comprising 216 individual solar cells. (G) Respective power conversion efficiency (PCE) of such a set of solar cells (averaged in groups of six) with the layer stack glass/ITO/ZnO/PM6:Y6-C12:$PC_{61}BM$/PEDOT-F/Ag. (H) Simulated PCE loss analysis of a 143 × 143 mm module based on PM6:Y6-C12:$PC_{61}BM$ as a function of subcell number. (I) Certified current–voltage and power–voltage measurements performed by Fraunhofer ISE (Freiburg, Germany) on this module. Reproduced with permission from Basu *et al.*,[40] Copyright 2024 Elsevier.

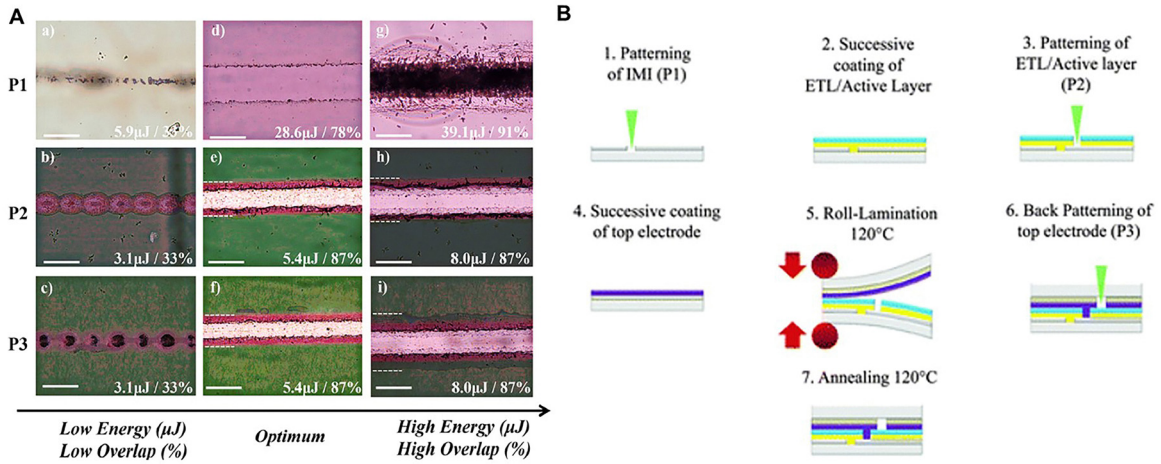

Fig. 7 Laser scribing techniques. (A) Optical microscopy images for below (A)–(C), optimum (D)–(F), and above (G)–(I) ablation threshold of P1, P2, and P3 processes. The white line indicates a 40 μm scale and dashed line represents heat-affected zone outer boundaries. Reproduced with permission from Kapnopoulos *et al.*,[107] Copyright 2022 MDPI. (B) Step-wise fabrication route of solution-processed roll laminated modules. Reproduced with permission from Spyropoulos *et al.*,[127] Copyright 2016 Royal Society of Chemistry.

accelerated, nonhalogenated blade coating and laser scribing techniques under ambient air achieved a PCE of 14.55% with a GFF of 96.5% and an exceptionally high FF of 76%, which was comparable to that of small-area cells (Fig. 6I).

Building on this requirement, C. Kapnopoulos *et al.* optimized picosecond laser parameters, with particular attention paid to the pulse energy and overlap rate, to realize flexible OSC modules using fully laser-defined P1, P2, and P3 processes (Fig. 7A).[107] In addition to standard opaque OSC modules, laser scribing has also enabled the fabrication of specialized semi-transparent OSC modules, which are critical for BIPV applications. Achieving this, however, requires even greater control over the patterning process to avoid damaging the delicate, multilayered stacks of these devices. To mitigate the risk of thermal damage and alignment errors, advanced laser processing strategies have been developed. L. Lucera *et al.* employed ultrashort laser pulses to facilitate monolithic interconnection of OSC modules. This highly precise ablation process reduced the dead zone width to below 100 μm, enabling the demonstration of roll-coated flexible modules with an unprecedented GFF of 98.5%.[48] In related work, G. D. Spyropoulos *et al.* demonstrated a depth-resolved laser patterning method that mitigates the alignment errors and thermal damage induced during the P3 patterning of laminated top electrodes (Fig. 7B).[127] By transmitting a femtosecond laser through the laminated top electrode, this method enables the selective removal of only the top metal layer, thereby allowing accurate P3 line formation and achieving a high GFF without causing collateral damage. Such advances in depth control and patterning precision have been instrumental for progressing OSC modules toward large-area, commercially relevant manufacturing schemes.

3.4 Other designs for OSC modules

While advancing series-connected OSC modules, a new self-aligned architecture that alternates normal and inverted subcells has been developed to simultaneously curb the lateral resistance losses and aperture losses of large-area designs.[128] This "alternating normal-inverted" layout forms efficient series interconnections on a single, continuous transparent electrode by using alternating interfacial layers, thereby obviating vertical metal–metal interconnects in the SCR and minimizing the P2-related dead area (Fig. 8A). Rather than dedicating space to a laser-scribed P2 trench for recombination contacts, the module sequences conventional and inverted subcells by selectively employing different charge-transport layers, *i.e.*, the HTL for conventional subcells and the ETL for inverted subcells, while sharing the same continuous TCO. Polyethyleneimine (PEI) plays a dual, thickness-dependent role (Fig. 8B): in inverted subcells, a PEI-induced interfacial dipole lowers the work function of the ITO and acts as an effective ETL; in normal subcells, an ultrathin PEI layer permits tunneling-assisted carrier transport, enabling full-area coating without blocking the transfer of charge across the shared electrode. This interfacial asymmetry provides self-aligned, post-patterning-free series links between adjacent subcells, eliminating the need for P2 laser scribing while preserving the optical aperture. As a result, this alternative module design attains a high GFF of approximately 96% without P2 scribing and demonstrates robust series interconnections across its subcells (Fig. 8C). The architecture thus relaxes the traditional tradeoff between aperture losses and sheet resistance-induced voltage drops by reducing the gap count and maintaining a continuous current-collection plane.

Another practical "post-P2 patterning-free" architecture, demonstrated by S. Hong *et al.*, achieves series connections by selectively depositing the photoactive layer without patterning the underlying charge transport layers.[81] In this design, the active layer is precisely printed *via* slot-die coating only in the designated active areas, yielding a high GFF of 90% without any subtractive post-patterning of a P2 line (Fig. 8D). The resulting module structure consists of the full device stack (ITO/ETL/active layer/HTL/Ag) in the active regions. In the SCR, however, the top silver electrode of one subcell directly overlaps the

exposed ETL/HTL bilayer of the adjacent subcell. This vertically stacked ETL/HTL interface functions as a charge recombination junction, which is essential for series connections. Carriers photogenerated from adjacent subcells are collected by their respective electrodes and then transported to this charge recombination junction (CRJ), where they recombine to complete the series circuit and enable voltage addition (Fig. 8E). The electrical behavior of this CRJ is critical for the performance of the constructed module. Each SCR can be represented by an equivalent circuit consisting of a recombination diode in parallel with a shunt resistor (R_{sh}) and in series with a series resistor (R_s); the effective parameters depend on the ETL/HTL polarity and interfacial energetics. For example, ETL/HTL junction (*e.g.*, ZnO/MoO_3) contacts typically favor forward recombination with low R_s, whereas the reverse-biased configuration results in a higher R_{sh}, which suppresses leakages. This configuration facilitates efficient, low-loss charge recombination between neighboring subcells, optimizing the overall performance of the constructed module (Fig. 8F).

A P2-free route to module fabrication can be further realized through self-aligned patterning based on surface energy engineering, in which surface energy-guided patterning ensures that each subcell is clearly defined and consistently connected in series, minimizing unwanted overlaps and maximizing the active area available for light absorption.[129] This approach involves the selective deposition of a hydrophobic self-assembled monolayer (SAM) on the substrate to create controlled surface energy contrasts, with the SAM retained specifically in the SCRs where interelectrode contact is formed (Fig. 8G). These hydrophobic regions, which are characterized by low wettability, repel the processing solution, thereby directing the flow along adjacent hydrophilic tracks. This selective wetting scheme establishes well-defined boundaries and enables self-aligned coatings to be applied precisely in the desired areas, ensuring the accurate registration of series-connected electrodes without any post-patterning (*e.g.*, scribing) steps (Fig. 8H). By exploiting surface energy contrasts to control wettability, the method provides a uniform line geometry and subcell alignment

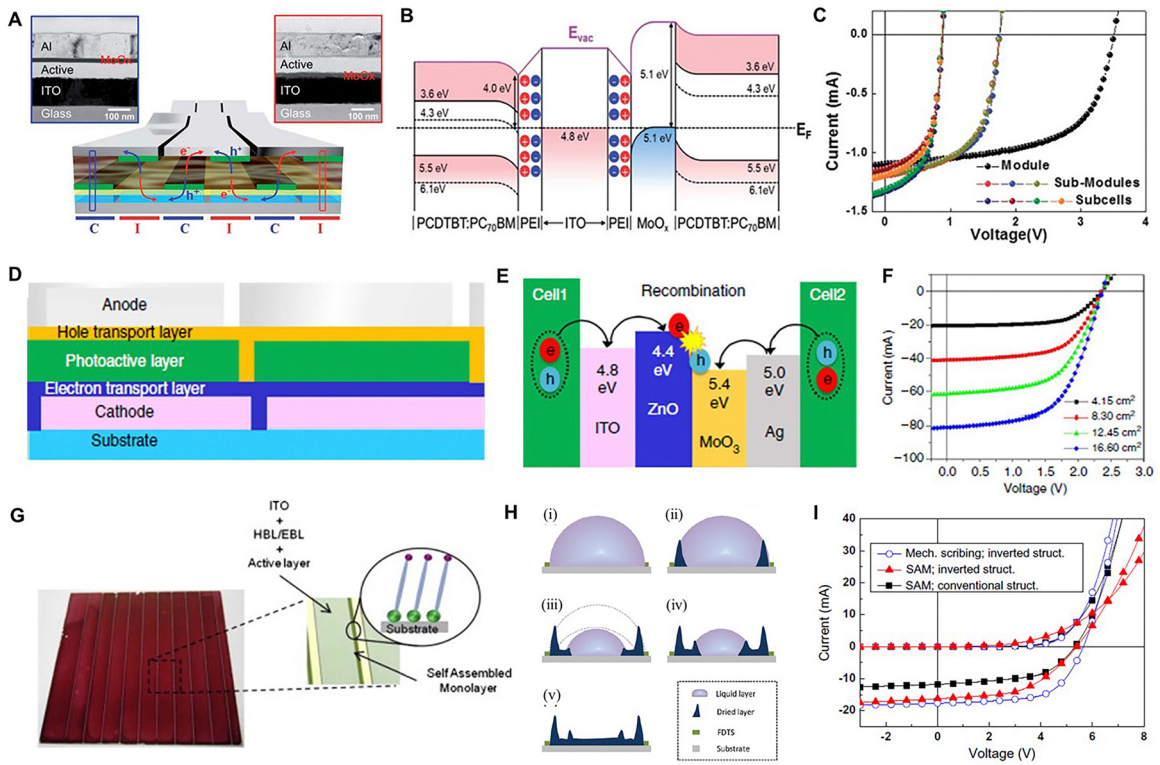

Fig. 8 Other OSC module structures. (A) Schematic illustration of alternative OSC module architecture. TEM images of the dual subcell stacks in (blue) the conventional and (red) the inverted configuration. (B) The energy diagram drawn from the measured CPD values describes the energy band structures of the self-aligned dual charge-selecting substructure and the surface of the active layer. (C) The photovoltaic characteristics in the alternative OSC modules. PEI: polyethleneimine, KPFM: Kelvin probe force microscopy, CPD: contact potential difference. Reproduced with permission from Lee *et al.*,[128] Copyright 2013 Royal Society of Chemistry. (D) Conceptual module structure consisting of pattern-less electron-transport and hole-transport layers and one patterned photoactive layer. (E) Energy level diagrams of series connection region components. (F) *I*–*V* characteristics of OSC modules of various sizes depending on module lengths from 1 to 4 cm. Reproduced with permission from Hong *et al.*,[81] Copyright 2016 Nature Publishing Group. (G) Image of a SAM is used for the patterning of the photoactive layer. (H) Graphical sketch of the drying process of the photoactive layer: (i) material in liquid phase pinned between two FDTS lines (ii) accumulation of material at the pinned edges caused by the coffee ring effect, (iii) secondary pinning of the liquid material known as the stick–slip effect, (iv) accumulation of material at the edges of the second pinning and (v) profile of the dried layer with two pinning contacts. FDTS: 1*H*,1*H*,2*H*,2*H*-perfluorodecyltrichlorosilane (I) *I*–*V* characteristics of SAM patterned modules for both inverted and conventional cell designs. A fully mechanically scribed module with the inverted design is also shown for comparison. Reproduced with permission from Etxebarria *et al.*,[129] Copyright 2013 Elsevier.

across the module, offering an efficient and reliable route to achieving series interconnections in OSC modules (Fig. 8I).

4. PSC modules

PSCs have been considered promising solar-energy technologies that are capable of competing with or displacing silicon solar cells, driven by their rapid PCE increases to nearly 27% and by their compatibility with large-area processing.[36] Whereas silicon requires approximately five decades to approach its present efficiency plateau, PSCs achieved comparable laboratory efficiencies in approximately 15 years, catalyzing efforts toward the commercialization of all-perovskite and perovskite/silicon tandem modules.[20,130–133] In 2009, Miyasaka and his coworkers first demonstrated perovskite materials as visible-light sensitizers for solar cells, reporting a PCE of 3.8% with $CH_3NH_3PbI_3$ on TiO_2.[134] In 2012, all-solid-state PSCs were reported using $CH_3NH_3PbI_3$ perovskite nanocrystals as the photoactive layer and spiro-OMeTAD as the HTL, achieving a PCE of 9.7% with *ex situ* stability over 500 h.[135] In 2014, a solvent engineering method that yields highly uniform, highly crystalline perovskite films *via* an intermediate phase was introduced; this protocol has since become a mainstay for high-efficiency PSCs.[136] Since then, the advancements have been multifaceted. Compositional engineering has shifted from simple $CH_3NH_3PbI_3$ to more robust and efficient mixed-cation/halide perovskites (*e.g.*, incorporating formamidinium (FA^+) and cesium (Cs^+)).[137–140] Simultaneously, the optimization of ETLs and HTLs and sophisticated interfacial engineering methods have been crucial for increasing the performance of devices to their current height.[141–145] This remarkable success in laboratory-scale cells has now shifted the research focus to the critical challenge of translating these achievements into large-area, high-performance modules.

Since 2013, PSCs have surpassed OSCs in terms of their PCEs, exhibiting a rapid increase in efficiency that catalyzed research on large-area PSC modules, in parallel with efforts executed across other next-generation photovoltaics.[71,146–149] The first significant milestone was achieved by Di Carlo's group, which first reported dye-sensitized solar cell modules based on a solid electrolyte using P3HT (a donor polymer that later became widely used in the photoactive layers of OSCs) with a PCE of 5.1% over a 1 6.8-cm^2 active area.[71] Although the PCEs of large-area PSC modules initially lagged behind those of small-area devices, steady progress followed, with the PCEs of printed modules exceeding 10% by 2016.[150] As the printing of functional layers and patterning processes matured, the performance of PSC modules advanced sufficiently to be listed on the NLR module chart, with some reports approaching or exceeding 20% (Fig. 1D and Table 2). Notably, the efficiency gap between small-area cells and large-area modules has been narrowed by increasing the GFF, which was achieved by reducing the interconnection width *via* high-precision processes such as laser scribing.[151–170] However, beyond PCE gains, the long-term operational stability of large-area modules has emerged as a critical challenge, particularly when potentially damaging processes such as laser scribing are used.[72,171] Therefore, the following sections discuss module-level performance improvements with an emphasis on architectural designs.

4.1 Monolithic PSC modules based on mechanical patterning

In the early stage of the PSC module development process, spin coating was used to form solution-processable functional layers, and a series of interconnections were defined by mechanical patterning.[39,71,172,173] For successive patterning, a solvent that is capable of selectively dissolving a given layer was applied to a swab-like tool to expose the SCR. When metal–oxide charge–transport layers were located at the bottom, water or alcohols were used prior to conducting postdeposition annealing, which converted the precursor into a dense film. Perovskite films, being susceptible to water and alcohols, were likewise patterned with solvent-wetted tools to open contacts between the transparent bottom electrode and the top electrode.

In one of the first reported PSC modules, a spin-coated $CH_3NH_3PbI_3$ photoactive layer and a P3HT HTL were mechanically patterned using a mixed solvent consisting of *N*,*N*-dimethylformamide and chlorobenzene, after which an Au top electrode was deposited through a shadow mask to complete the series interconnection.[71] The striped active area had a width of 7 mm, whereas the total inactive (patterned) region spanned 3.5 mm, yielding a GFF of 67% and a correspondingly reduced PCE for the module over the aperture area. Because the manual process relies on solvent dissolution, overly aggressive solvents can increase the patterned gap beyond the intended design, thereby decreasing the fraction of the active area. Although manual, solvent-assisted mechanical patterning provides a convenient pathway for demonstrating the transition from small-area devices to large-area modules, its scalability is constrained by the difficulty of achieving a high GFF and a precise line definition scheme, which ultimately limits the PCE of the constructed module.

To attain improved precision and avoid potential solvent-induced damage, the field has progressed to solvent-free mechanical patterning, primarily using knife-blade scribing.[174,175] Without using a dissolving solvent, an early demonstration performed by T.J. Marks and his coworkers utilized this method for implementing the P2 process in eight cells connected to 5×5 cm^2 total area modules, achieving a GFF of 60%.[174] Although some early reports labeled as utilizing mechanical patterning did not always specify their solvent use statuses, such mechanically defined modules generally exhibited lower PCEs than their small-area counterparts did, largely because their GFF values were less than approximately 70%. In 2016, W. Qiu *et al.* demonstrated high-efficiency PSC modules patterned by knife scribing, reaching a 13.6% PCE at a 4 cm^2 aperture with a GFF of 91%.[150] Both P2 and P3 were scribed with a knife mounted on a computer-controlled XYZ stage under nitrogen, yielding a narrow inactive gap of 0.43 mm between adjacent 4.57 mm wide active stripes. In 2017, K. Zhu formulated perovskite precursor inks to enable spin/printing with a wide processing window and high crystallinity and then fabricated a 12.6 cm^2 four-subcell module *via* mechanical P2/P3 scribing, achieving a total area PCE of 11.7% with an 88% GFF.[176]

Table 2 Representative papers reporting module PCEs calculated on the aperture module area, explicitly considering GFF in PSC modules from 2014 to 2025

Year	Device structure	P1	P2	P3	GFF (%)	Module PCE (%)	Module area (cm^2)	Ref.
2014	Glass/FTO/c-TiO_2/nc-TiO_2/$CH_3NH_3PbI_{3-x}Cl_x$/P3HT/Au	—	Mechanical patterning	Mask patterning	67.2[a]	3.43[a]	25	S63
2014	Glass/FTO/BL-TiO_2/scaffold+perovskite/perovskite/P3HT/Au	Laser scribing	Laser scribing	—	70	9.1	15.43	S64
2015	Glass/FTO/c-TiO_2/nc-TiO_2/$MAPbI_3$/P3HT/Au	—	Laser scribing	Laser scribing	73	4.3	100	S65
2016	Glass/ITO/TiO_2/$MAPbI_{3-x}Cl_x$/spiro-OMeTAD/Au	Laser scribing	Mechanical scribing	Mechanical scribing	91	12.6	4	S66
2016	Glass/bl-TiO_2/Mp-TiO_2/ZrO_2/carbon	—	Screen printing	Screen printing	70[a]	7.53[a]	100	S67
2017	Glass/FTO/c-TiO_2/$MAPbI_3$/spiro-OMeTAD/Ag	—	Mechanical scribing	Mechanical scribing	88	11.7[a]	12.6	S68
2017	Glass/FTO/c-TiO_2/m-TiO_2+graphene/graphene oxide-Li/$MAPbI_3$/spiro-OMeTAD/Au	Laser scribing	—	—	73	9.20[a]	69.3[a]	S69
2017	Glass/FTO/c-TiO_2/m-TiO_2/ZrO_2/$MAPbI_3$/(graphite/carbon)	Laser scribing	Screen printing	Screen printing	49[a]	5.10[a]	100	S70
2018	Glass/FTO/TiO_2/CsFAMAPb$(I_{0.83}Br_{0.17})_3$/spiro-OMeTAD/Au	Laser scribing	Laser scribing	Laser scribing	92	16.6	14	S71
2018	Glass/FTO/cTiO_2/$MA_{0.7}FA_{0.3}PbI_3$/spiro-OMeTAD/Au	Laser scribing	Mechanical scribing	Mechanical scribing	87.3	16.3	10.36	S72
2018	Glass/ITO/PTAA/$MAPbI_3$/C60/BCP/Cu	Laser scribing	Laser scribing	Laser scribing	93.4	15.3	33.0	S73
2018	Glass/ITO/c-TiO_2/$MAPbI_{3-x}Cl_x$/spiro-OMeTAD/Au	Laser scribing	Laser scribing	Laser scribing	95	11.2	149.5	S74
2018	Glass/FTO/c-TiO_2/m-TiO_2/$MAPbI_3$/spiro-OMeTAD/Au	Laser scribing	Mechanical scribing	Mechanical scribing	92.4	12.6	354.45	S75
2018	Glass/ITO/PTAA/PFN/$MAPbI_3$/PCBM/PFN/Ag	Chemical etching	Electrochemical patterning	Mask patterning	94.1	14.1	9.06	S76
2019	Glass/FTO/SnO_2/$[CsPbI_3]_{0.05}$ $[(FAPbI_3)_{0.85}(MAPbBr_3)_{0.15}]_{0.95}$/spiro-OMeTAD/Au	Laser scribing	Laser scribing	Mechanical scribing	95.5	15.3 14.0	25 100	S77
2019	Glass/FTO/SnO_2/$Cs_{0.1}FA_{0.9}PbI_{2.9}Br_{0.1}$/spiro-OMeTAD/Au	—	Laser scribing	Mechanical scribing	90	9.34	91.8	S78
2019	Glass/FTO/d-TiO_2/mp-TiO_2/$(FAPbI_3)_{0.95}(MAPbBr_3)_{0.05}$/DHA/P3HT/Au	Laser scribing	Laser scribing	Laser scribing	94.4	17.1	24.97	S79
2019	Glass/FTO/TiO_2/$FAPb(I_{0.85}Br_{0.15})_3$/spiro-OMeTAD/Au	—	Mechanical patterning	Mask patterning	40	5.88[a]	25	S80
2019	Glass/ITO/SnO_2/$MAPbI_3$/PTAA/Au	—	Mechanical scribing	Mechanical scribing	80.7	11.5	27.25	S81
2019	Glass/FTO/TiO_2/$MAPbI_3$/spiro-OMeTAD/Au	Laser scribing	Laser scribing	Laser scribing	86.7	12.74[a]	54.21[a]	S82
2019	Glass/FTO/c-TiO_2/mTiO_2/$MAPbI_3$/fMoS_2/spiro-OMeTAD/Au	Laser scribing	Laser scribing	Laser scribing	88	11.79[a]	122.73[a]	S83
S2020	Glass/FTO/NiO_x/$CsPbI_2Br$/ZnO@C60/Ag	Laser scribing	Laser scribing	Laser scribing	75	9.14[a]	14.56[a]	S84
2020	Glass/ITO/PTAA/PFN/$MAPbI_3$/C60/BCP/Ag	—	—	—	90	15.96[a]	3.0	S85
2020	Glass/FTO/SnO_2/e$(CsPbI_3)_{0.05}((FAPbI_3)_{1-x}(MAPbBr_3)_x)_{0.95}$/spiro-OMeTAD/Au	Laser scribing	Laser scribing	Laser scribing	90.8	17.88	25.49	S86
2020	Glass/ITO/PTAA/$FA_{0.92}Cs_{0.08}PbI_3$/C_{60}/BCP/Cu	—	Laser scribing	Laser scribing	93.0	17.8	21.5	S87
2020	Glass/FTO/TiO_2/$FA_{0.91}Cs_{0.09}PbI_3$(23%MACl)/[M4N]BF4/spiro-OMeTAD/Au	Laser scribing	Laser scribing	Laser scribing	85.7	16.80[a]	9.24[a]	S88
2020	PEN/ITO/SnO_2/ZSO/$(FAPbI_3)_{0.95}(MAPbI_3)_{0.05}$/spiro-OMeTAD/Au	Laser scribing	Laser scribing	Laser scribing	90	15.5	100	S89
2020	Glass/ITO/NiO_x/$(Cs_{0.17}FA_{0.83})PbI_3$/C60/BCP/Ag	Laser scribing	Laser scribing	—	90	13.68[a]	6.56[a]	S90
2021	Glass/FTO/cTiO_2/mTiO_2/GO-X/$Cs_{0.06}FA_{0.78}MA_{0.16}Pb(I_{0.83}Br_{0.17})_3$/spiro-OMeTAD/Au	Laser scribing	Laser scribing	—	88	14.17[a]	18.18[a]	S91
2021	Glass/ITO/PTAA/$FA_{0.92}Cs_{0.08}PbI_3$/C60/BCP/Cu	—	Laser scribing	Laser scribing	92	18.6	29.5	S92
2021	Glass/FTO/c-TiO_2/m-TiO_2/$(FAPbI_3)_{0.95}(MAPbBr_3)_{0.05}$/spiroMeOTAD/Au	Laser scribing	Laser scribing	Laser scribing	94.36	20.4	31	S93
2021	Glass/ITO/PTAA/$MA_{0.6}FA_{0.4}PbI_3$/C60/BCP/Cu	Laser scribing	Laser scribing	Laser scribing	92	19.2	50	S94
2021	Glass/FTO/NiMgLiO/$FA_{0.83}Cs_{0.17}PbI_{2.83}Br_{0.17}$/LiF/C60/BCP/Bi/Ag	Laser scribing	Laser scribing	—	92.7	15.42	22.41[a]	S95
2021	Glass/ITO/SnO_2/$Cs_{0.05}FA_{0.54}MA_{0.41}Pb(I_{0.98}Br_{0.02})_3$/spiro-OMeTAD/Au	Laser scribing	Laser scribing	Mechanical scribing	89	14.55	22.4	S96
2021	Glass/FTO/c-TiO_2/SnO_2/perovskite/spiro-OMeTAD/Au	Laser scribing	Laser scribing	Laser scribing	90	15.2	12	S97
2021	Glass/FTO/SnO_2/$Cs_{0.05}FA_{0.85}MA_{0.1}PbI_{2.85}Br_{0.15}$/spiro-OMeTAD/Au	—	Laser scribing	Mechanical scribing	90.05	15.62 11.80	22.4 100	S98
2022	Glass/FTO/c-TiO_2/m-TiO_2/$MAPbI_3$,GVL/ZrO_2/carbon	Laser scribing	Mechanical scribing	Mechanical scribing	80	7.24[a]	275[a]	S99
2022	Glass/FTO/SnO_2/1D,3D perovskite/spiro-OMeTAD/Au	Laser scribing	Laser scribing	Laser scribing	80	15.68[a]	22.5	S100
2022	Glass/FTO/c-TiO_2/m-TiO_2/$Cs_{0.05}MA_{0.14}FA_{0.81}PbI_{2.58}Br_{0.42}$/spiro-OMeTAD/Au	Laser scribing	Laser scribing	Laser scribing	91	17.03[a] 10.83[a]	2.47[a] 210.99[a]	S101
2022	Glass/FTO/Zn_2SnO_4/perovskite/spiro-OMeTAD/Au	Laser scribing	Laser scribing	Laser scribing	88	19.88	34.36	S102
2022	Glass/FTO/c-TiO_2/m-TiO_2/$FAPbI_3$/OAI/spiro-MeOTAD/Au	Laser scribing	Laser scribing	Laser scribing	95.6	20.72[a]	20.92[a]	S103
2022	Glass/FTO/NiO_x/SRE/perovskite/PCBM/BCP/Ag	Laser scribing	Laser scribing	Laser scribing	85.7	15.94[a]	203.03	S104
2022	Glass/FTO/SnO_2/$FA_{0.88}Cs_{0.12}PbI_3$/spiro-OMeTAD/Au	Laser scribing	Laser scribing	Laser scribing	96	21.4	22.4	S105
2022	Glass/ITO/PTAA/$Cs_{0.25}FA_{0.75}Pb(I_{0.85}Br_{0.15})_3$/C60/$SnO_2$/Au/PEDOT:PSS/$Cs_{0.2}FA_{0.8}Pb_{0.5}Sn_{0.5}I_3$/PCBM/C60/BCP/Cu	—	Laser scribing	Laser scribing	93.8	21.6	14.3	S106
2023	Glass/FTO/b-TiO_2/np-SnO_2/$(FAPbI_3)_{0.95}(MAPbBr_3)_{0.05}$/spiro-OMeTAD/Au	Laser scribing	Laser scribing	Laser scribing	92	20.15	81	S107
2023	Glass/FTO/SnO_2/$(Cs_{0.05}(MA_{0.17}FA_{0.83})_{0.95}Pb(I_{0.83}Br_{0.173}$/PEAI/spiro-OMeTAD/Au	Laser scribing	Laser scribing	Laser scribing	93	16.13	201	S108
2023	Glass/ITO/PTAA:BCP/$CsFAPbI_3$/C60/BCP/Cu	—	Laser scribing	Laser scribing	94.7	21.8	26.9	S109
2023	Glass/FTO/TiO_2/SnO_2/$CsMAFAPbI_3$/PEAI/spiro-MeOTAD/Au	Laser scribing	Laser scribing	Laser scribing	93	21.4	27.8	S110
2023	Glass/FTO/bl-TiO_2/mp-TiO_2/$FAPbI_3$/PTAA/Au	Laser scribing	Laser scribing	Laser scribing	93.1	18.54	224.89	S111

Table 2 (*continued*)

Year	Device structure	P1	P2	P3	GFF (%)	Module PCE (%)	Module area (cm^2)	Ref.
2023	MgF_2/glass/ITO/NiO_x/Me-4PACz/TEACl/$Cs_{0.1}FA_{0.9}PbI_3$/TEACl/LiF/C60/BCP/Cu	Laser scribing	Laser scribing	Laser scribing	90.8	20.5	4	S112
2023	PEN/ITO/SP-NiO_x/SAMs/$(CsPbI_3)_{0.13}(FAPbI_3)_{0.85}(MAPbBr_3)_{0.2}$/C60/BCP/Au	Laser scribing	Laser scribing	Laser scribing	93	18.17	61.26	S113
2024	PET/TCE/SnO_2/$FA_{0.45}MA_{0.55}PbI_3$/HTAB/P3HT/carbon/Ag	—	Slot-die coating (R2R)	Screen printing (R2R)	75	8.25[a]	66[a]	S114
2024	Glass/FTO/NiO_x/Me-4PACz, NA/$FA_{0.95}Cs_{0.05}PbI_3$/PI/$PC_{61}BM$/BCP/Ag	Laser scribing	Laser scribing	Laser scribing	97.5	23.06	11.1	S115
2024	Glass/FTO/NiO_x/Me-4PACz/$FA_{0.93}MA_{0.02}Cs_{0.05}PbI_{2.94}Br_{0.06}$/PEACl/PCBM/$SnO_2$/Cu	Laser scribing	Laser scribing	Laser scribing	94.7	22.73	14.61	S116
2024	Glass/FTO/SnO_2/CsMAFAPbI$_3$/PEAI/spiro-OMeTAD/Au	Laser scribing	Laser scribing	Laser scribing	91	21.1	31	S117
2024	Glass/FTO/c-TiO_2/c-SnO_2/$Cs_{0.05}MA_{0.05}FA_{0.9}PbI_3$/PEDOT:PSS doped spiro-OMeTAD/MoO_x/ITO/Au	Laser scribing	Laser scribing	Laser scribing	96.5	23.2	27.2	S118
2024	Glass/FTO/SnO_2@TiO_2/PMMA:PCBM/$Cs_{0.05}MA_{0.05}FA_{0.9}Pb(I_{1-x}Br_x)_3$/PEAI/spiro-MeOTAD:PDCBT/MoO_3/Cr/Au	Laser scribing	Laser scribing	Laser scribing	95.74	23.3	27.22	S119
2024	Glass/ITO/CbzNaph/$Cs_{0.05}FA_{0.95}PbI_3$/PEAI/C60/BCP/Ag	Laser scribing	Laser scribing	Laser scribing	92.4	22.43	15.45	S120
2024	Glass/FTO/NiO_x/$Cs_{0.05}MA_{0.05}FA_{0.9}PbI_3$/PCBM/BCP/Ag	Laser scribing	Laser scribing	Laser scribing	95.7	20.2	29	S121
2024	Glass/FTO/SAMs/$Cs_{0.1}FA_{0.9}PbI_3$/PEAI/C60/ALD-SnO_2/Au	Laser scribing	Laser scribing	Laser scribing	97	23.28	22.96	S122
2024	Glass/ITO/SnO_2/2-step perovskite/spiro-OMeTAD/Au	Laser scribing	Laser scribing	Laser scribing	93.7	21.13	29	S123
2025	Glass/ITO/Bi-SnO_2/$FAPbI_3$/spiro-OMeTAD/Au	—	Mechanical scribing	Mechanical scribing	87	17.92[a]	14.94[a]	S124
2025	Glass/ITO/SnO_2/perovskite/spiro-OMeTAD/Au	Laser scribing	Laser scribing	Laser scribing	96	22.76	57.20	S125
2025	Glass/FTO/SnO_2/perovskite/spiro-OMeTAD/Au	Laser scribing	Laser scribing	Laser scribing	95	23.29	25	S126
2025	Glass/ITO/SnO_2/perovskite/spiro-OMeTAD/Au	Laser scribing	Laser scribing	Laser scribing	95.2	20.19	750	S127
2025	Glass/FTO/NiO_x/2-PACz/$FA_{0.90}Cs_{0.05}MA_{0.05}PbI_{2.95}Br_{0.05}$/C60/BCP/Ag	Laser scribing	Mechanical scribing	Mechanical scribing	81.1	18.73[a]	13.31[a]	S128
2025	Glass/ITO/SnO_2/perovskite/spiro-OMeTAD/Au	Laser scribing	Mechanical scribing	Mask patterning	97.3	19.88	14.1	S129

[a] Calculated values from the corresponding papers.

Pushing the boundaries of this technique, H.B. Lee *et al.* developed a mechanical scribing methodology using a 3D direct ink-writing platform in 2025, wherein a metal needle traversed at 2 mm s^{-1} to pattern the stacked layers (Bi–SnO_2/perovskite/spiro-OMeTAD) (Fig. 9A).[70] The P3 line was subsequently mechanically defined to complete a six-subcell, series-connected PSC module, as shown in Fig. 9B and C. The inactive interconnection span from P1 to P3 measured approximately 855 μm, yielding a GFF of 87% when calculated as the photoactive-to-total-area ratio (Fig. 9D and E). The resulting module delivered a peak PCE of 20.6% at an active area of 13.0 cm^2, with a stabilized PCE exceeding 19% under 500 s of maximum power point tracking (MPPT) and demonstrating consistent device-to-device performance. C. Zuo *et al.* successfully fabricated PSC utilizing P2 mechanical scribing and P3 mask patterning processes illustrated in Fig. 9F.[177] Especially, the mechanical scribing process enables the formation of straight P2 lines with an average width of 19.6 μm, achieving a narrow dead area of 193 μm from of P1 to P3 as shown in Fig. 9G. The PSC modules based on laser-free scribing process achieved a module PCE of 19.88% at the aperture area of 14.1 cm^2 with a high GFF of 97.3% (Fig. 9H).

Under the reported test conditions, mechanical scribing did not result in power-related degradation, suggesting potential stability advantages over laser-based approaches. Further work is warranted to increase the GFF and scale the module area; to date, this represents one of the highest-efficiency PSC modules that has been realized *via* mechanical patterning.

4.2 Monolithic PSC modules based on printed patterns

The solubility of perovskite precursors and charge transport materials allows for the use of various printing processes in PSC fabrication schemes, including doctor blade coating, slot-die coating, spray coating, ink-jet printing, and screen printing.[51,178–182] Concurrently, cell-level efficiency advancements have led to progress in the fabrication of modules at a larger scale using these printing technologies.[20,21,28,44] However, in contrast with OSCs, the primary role of these techniques in PSC module production tasks has been scalable large-area coating, not direct patterning. To date, very few reports of fully printed PSC modules have been published, with most studies relying on lower-resolution methods such as screen printing, typically for the production of less sensitive layers that are compatible with paste processing.[65,66,183] Thus, the dominant fabrication strategy has become a hybrid approach: functional layers are deposited uniformly over a large area using a printing method, and the necessary P1–P2–P3 interconnection lines are subsequently created using a subtractive method such as laser scribing.

Meniscus-based techniques such as doctor blade coating and slot die coating are highly scalable, roll-to-roll-compatible, high-throughput printing processes.[44,153,169,184–188] Doctor blade coating is effective for scaling from small-area devices to larger substrates, but laser scribing is typically needed to define series interconnects because the process results in the formation of a continuous meniscus along a long blade, yielding wide, planar films rather than inherently patterned features. Moreover, its reliance on continuous solution feeding and the

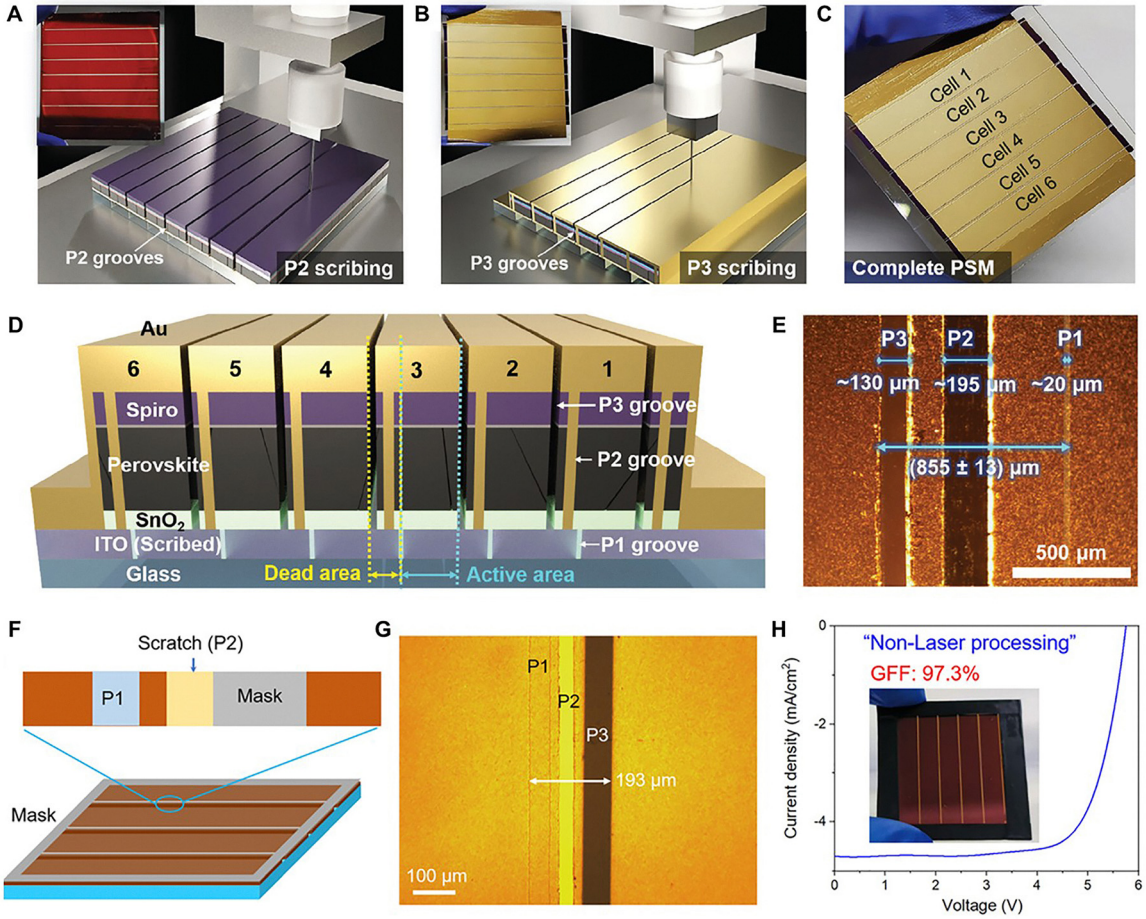

Fig. 9 PSC modules based on the mechanical scribing technique. Schematic illustration of the low-cost mechanical scribing process of the PSC module performed using a 3D-DIW instrument for (A) P2 and (B) P3 scribing. Schematic images showing the (C) six series-connected cells and (D) P1–P2–P3 electrical interconnections between the adjacent cells in the mechanically-scribed PSC modules. (E) Optical microscopic image showing the P1, P2, P3 grooves and dead areas on the PSC modules. Reproduced with permission from Lee *et al.*,[70] Copyright 2025 Wiley-VCH GmbH. (F) Illustration of a mask with metal grids on a perovskite film. (G) Optical microscopy image of P1, P2, and P3 lines in a module. (H) *J*–*V* curve and photo of the module with non-laser processed P2 and P3 lines. Reproduced with permission from Zuo *et al.*,[177] Copyright 2025 Royal Society of Chemistry.

absence of native pattern selectivity limit the suitability of doctor blade coating as a stand-alone commercial patterning process for PSC modules. While patterned slot-die coating is a mature technology for OSCs, its application regarding PSCs remains a significant research challenge because of the complex crystallization dynamics of perovskite inks.[44,184–187] Therefore, developing a reliable, one-dimensional patterning-based slot-die coating technology specifically for perovskite layers is considered a critical step. Success in this area would enable the development of a truly scalable, low-cost printing process, greatly enhancing the commercial viability of PSC modules.

In addition to meniscus coating methods, spray coating has been investigated as a viable approach for achieving large-area deposition in PSC modules.[189–193] During spray processes, droplets are dispersed and subsequently coalesce into a wet film that, upon solvent removal, yields uniform layers; this route has been applied to ETLs, HTLs, and the perovskite absorber. B. Tyagi *et al.* developed antisolvent-free spray-coated PSCs and PSC modules by employing a propylene carbonate additive in a PbI_2 film.[190] The performance of the devices was improved because of the reduced number of defects and grain boundaries, resulting in a PCE of 19.3% for small-area cells and a module PCE of 15.8% for an area of 13 cm^2. Although spray coating, in principle, enables direct pattern formation *via* a nozzle or mask design, peer-reviewed demonstrations of fully pattern-printed PSC modules (without subsequent laser scribing steps) have not yet been reported. Inkjet printing, which is another noncontact droplet-based technique, involves the formation of films by ejecting micrometer-scale droplets from nozzle arrays onto predefined substrate regions, offering facile digital patternability, high resolutions, strong material efficiency, and good design flexibility.[194,195] These attributes have accelerated the development of PSCs, with high-efficiency inkjet-processed devices being increasingly reported; however, at the module level, inkjet-deposited layers are typically complemented by laser scribing to define P2/P3 interconnects.

PSC modules produced by printing processes such as doctor blade coating, slot-die coating, spray coating, and inkjet printing have, to date, been fabricated primarily with mechanical or laser scribing rather than with fully printed pattern formation

techniques.[44,153,169,184,188–191,193–195] In contrast, screen printing has yielded PSC module structures in which portions of the interconnects (most commonly when carbon or silver paste is used) are defined by a printed pattern.[65,66] Mhaisalkar and his coworkers demonstrated monolithic PSC modules using a screen-printing workflow in combination with perovskite infiltration. The screen mesh (stencil) was engineered to stabilize the infiltration process by reducing the interstripe gap to 1 mm, resulting in module PCEs of 10.46% and 10.74% for active areas of 31 cm^2 and 70 cm^2, respectively.[66] Although the GFF of this method was lower than that of its laser-scribed counterparts, the screen-printed modules delivered PCEs near 11%, with only 0.65% device-to-device variations across 18 samples.

F. D. Rossi *et al.* demonstrated a screen-printed PSC module composed of TiO_2, ZrO_2, and carbon electrodes as mesoporous stacks, as described in Fig. 10A.[65] In this module, the P1 line of the FTO bottom electrode was patterned by the laser scribing technique, but the P3 line of the carbon electrode was patterned *via* a screen-printed patterning process that was enabled by a stencil mesh design (Fig. 10B). In addition, patterning the TiO_2 layer *via* screen printing can improve the series connections between neighboring subcells, resulting in increases in the PCEs of PSC modules (Fig. 10C). Because perovskite precursor inks typically exhibit low viscosity and limited colloidal stability, preparing dense, defect-lean perovskite layers through screen printing remains challenging for high-efficiency PSC modules.[178] In contrast, the screen printing process used for

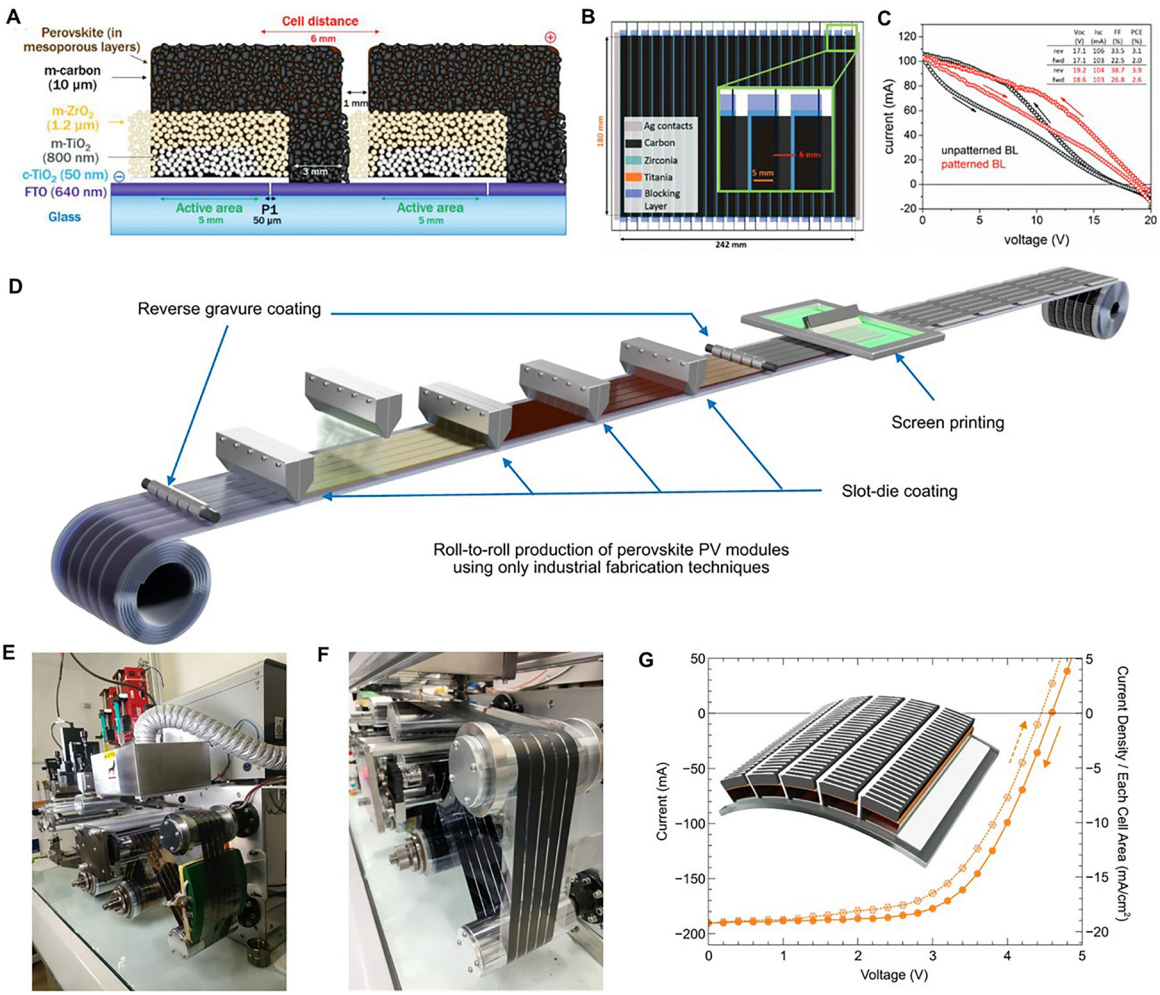

Fig. 10 PSC modules based on the printed patterning method. (A) Cross-section schematics of adjacent cells in the module with the nominal thickness of each layer, highlighting the laser-etched FTO, patterning of TiO_2 blocking layer and the electrical vertical connection, ensured by the carbon back contact. (B) Module schematics, showing the different overlapping layers, the dimensions of the active area for both the individual single cell and the whole module as well as the distance between adjacent cells (inset). (C) *I-V* curves for the best modules with unpatterned and patterned blocking layer (BL) (after 144 h at ambient conditions and 48 h of 70% RH treatment). Reproduced with permission from Rossi *et al.*,[65] Copyright 2018 Wiley-VCH GmbH. (D) Schematic illustration of roll-to-roll production of modules using slot-die coating, reverse gravure (RG) coating and screen printing. (E) Image showing the deposition of the perovskite layer using a 5-channel SD coater. The deposition of non-stoichiometric perovskite precursor solution, blow-drying, and the conversion to perovskite by SD coating the MAI solution were carried out in one coating run. (F) Image showing the RG-coated carbon film on the TCE/ETL/perovskite/HTL stack. (G) Current–voltage curves of a R2R produced module. Inset shows a schematic illustration of the module structure. Reproduced with permission from Weerasinghe *et al.*,[196] Copyright 2024 Springer Nature.

mesoporous scaffolds (*e.g.*, meso-TiO_2 or meso-ZrO_2) and carbon electrodes is considerably more tractable because of their higher-viscosity rheology. The systematic optimization of ink properties (*e.g.*, viscosity, surface tension, and solvent volatility) and mesh designs (*e.g.*, the thread count, emulsion thickness, and opening) is expected to improve screen-printed PSC modules and could reduce or eliminate the reliance on P2/P3 laser scribing.

In 2023, Vak and his coworkers first demonstrated fully roll-to-roll-fabricated PSC modules without laser-scribed patterning, indicating that completely printed patterning of P2 and P3 lines is possible for monolithic module designs.[196] The structure of a PSC module consists of gravure-printed SnO_2, slot-die-coated perovskite and P3HT layers, a gravure-printed carbon electrode, and a screen-printed silver grid, as illustrated in Fig. 10D. Although the gap between the striped subcells is slightly wider than that of the reported laser-scribed modules due to the limitation of the delicate patterned coating of the composed layers provided by printing methods, this enables the cost-effective, high-throughput fabrication of PSC modules (Fig. 10E and F). As a result, the fully roll-to-roll printed PSC modules had 11% module PCE and a 75% GFF (Fig. 10G).

4.3 Monolithic PSC modules utilizing laser scribing

Laser scribing has become an indispensable technique for the fabrication of PSC modules, where precise interconnections between subcells are critical for achieving high PCEs.[151–170] As PSCs transition from small-area devices to large-area modules, minimizing the induced cell-to-module losses relies heavily on the ability to form narrow and defect-free P1, P2, and P3 scribe lines that maximize the GFF. In 2015, an early demonstration performed by Carlo and his coworkers introduced a CO_2 laser to pattern the PbI_2 layer and the P3HT HTL, yielding a module PCE of 4.3% with a GFF of 73% over a large area of 100 cm^2.[39] A CO_2 laser emits infrared radiation at a wavelength of approximately 10.6 μm; this long wavelength is strongly absorbed by many materials, particularly organic compounds. With such an effective photothermal coupling, CO_2 laser irradiation has been explored for use in perovskite film annealing as a potential replacement for conventional thermal annealing.[197]

Based on these developments, laser technology has recently expanded into the film formation stage through laser annealing processes. For instance, Z. Chu *et al.* employed a 455 nm nanosecond laser to induce the complete crystallization of perovskite films within 25 seconds, achieving a PCE of 24% in a 100 cm^2 module.[198] Although lasers are increasingly employed for high-throughput annealing and crystallization, this review focuses on their primary role as a scribing technique for the monolithic series interconnection of modules. During laser scribing, multiple processing variables, including the wavelength, fluence (or power density), pulse duration, repetition rate, spot size, scan speed, and pulse overlap, govern the scribe quality and, ultimately, the performance of the developed module.[199–201] Since 2017, nanosecond laser pulses at 532 nm have been adopted to scribe P2 and P3 lines in laser-patterned PSC modules.[201–203]

State-of-the-art PSC modules typically employ nanosecond or picosecond laser scribing techniques, achieving GFF values of up to 95–99%.[141,152,163,165–167,169] When precise laser scribing is employed, the inactive area is reduced, allowing the stripe width to be decreased to approximately 5 mm, thereby mitigating the ohmic losses that are associated with the finite sheet resistance of transparent electrodes such as FTO and ITO. Liu *et al.* reported highly efficient p–i–n PSC modules developed by introducing phosphonic acid SAMs with multiple aromatic carboxylic acids, which reduced the interfacial energy loss and improved the quality of the perovskite film.[141] The NA-Me4PACz combination yielded superior buried-interface quality and higher perovskite crystallinity, leading to further improvements in the PCE. Utilizing spin coating for film deposition and laser scribing for series interconnection, a module PCE of 23.06% was achieved on an 11.1 cm^2 aperture with a GFF of 97.5%. Jen and his coworkers demonstrated inverted PSC modules produced *via* the spin-coating method and laser scribing technique to complete the monolithic module design process, as described in Fig. 11A.[164] Bilayer interface engineering can effectively passivate defects in the perovskite photoactive layer, thus minimizing the PCE gap that arises with increasing area, resulting in a module PCE of 21.43% at an aperture area of 15.45 cm^2 with a GFF of 92.4% (Fig. 11B).

Recent breakthroughs have continued to push the performance boundaries of PSC modules, driven by innovations in both materials and scalable processing techniques. Yang *et al.* developed liquid-crystal-based additives to suppress coprecipitation and aggregation in large-area perovskite films, enabling uniform defect passivation and yielding modules with a PCE of 21.1% at a module area of 31 cm^2.[161] In addition, these modules retained their initial PCEs after 1200 h of damp-heat testing (85% relative humidity, 85 °C). Ding *et al.* demonstrated PSC modules with a PCE of 23.30% on a 27.22 cm^2 aperture by incorporating methyltetrahydrotriazinium and dimethylammonium cations to increase the crystallinity of perovskite film and by employing laser scribing to achieve a high GFF of 96.5% (Fig. 11C–E).[163] Zhu *et al.* reported large-area PSC modules with a 57.20 cm^2 aperture, achieving a PCE of 22.76% *via* doctor blade coating in combination with laser scribing of the P1, P2, and P3 lines (Fig. 11F and G).[169] Overall, PSC modules exceeding 20% PCEs have been realized in both the n–i–p and p–i–n configurations, with many of the highest-performing methods relying on laser scribing to define their subcell interconnects.

Although laser scribing offers a patterning resolution of tens of micrometers, it can also introduce factors that degrade device performance and stability through process-induced damage and residue formation. At the fundamental level, laser scribing of perovskite films involves coupled photothermal and photomechanical processes.[199–201] The absorbed photons excite carriers that relax *via* nonradiative pathways, transferring energy to the lattice within ultrashort timescales. With respect to nanosecond pulses, extended interaction times promote significant thermal diffusion, often resulting in melting, PbI_2 decomposition, and the redeposition of molten material in a thermally dominated ablation regime.[199–201] In contrast, picosecond or femtosecond

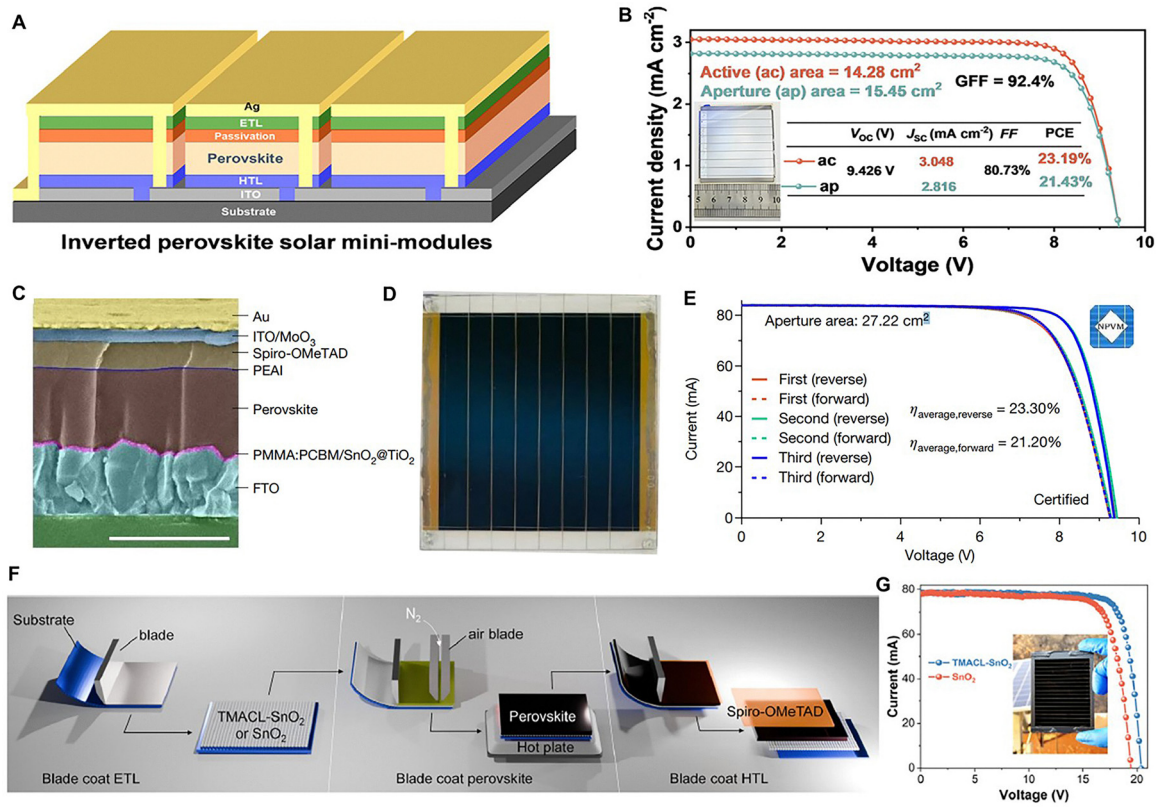

Fig. 11 Efficient PSC modules based on laser scribing techniques. (A) The device structure of the inverted perovskite solar mini-module in this work. (B) The *J*–*V* curve of bilayer-treated mini-module with 8 subcells. The inset is a picture of a 5 × 5 cm^2 mini-module. Reproduced with permission from Wang *et al.*,[164] Copyright 2024 Elsevier. (C) Cross-sectional SEM image of the target device. Scale bar, 1 μm. (D) Picture of one PSC module. (E) *I*–*V* curves of three consecutive tests from forward and reverse scans for the certified PSC module. Reproduced with permission from Ding *et al.*,[163] Copyright 2024 Nature Publishing Group. (F) Schematic illustration showing the tri-layer blade-coating manufacturing for TMACL–SnO_2 or pristine SnO_2 ETLs, perovskites, and HTL that is capable of both flexible and rigid substrates. (G) *I*–*V* curves of modules using different ETLs under AM 1.5G. Inset is a photography of the module. Reproduced with permission from Zhu *et al.*,[169] Copyright 2025 Elsevier.

pulses deposit energy faster than lattice relaxation can occur, leading to confined heating, explosive boiling, or stress-assisted liftoff processes.[72,199–201] C. Wang *et al.* demonstrated the distinct advantages of utilizing a femtosecond laser for the monolithic interconnection of perovskite solar mini-modules. The precision of the ultrashort pulses allowed for the complete removal of functional layers during P2 scribing without causing any damage to the underlying conductive substrate, effectively preventing contact resistance issues and securing a high GFF of 98.3%.[204]

Accordingly, ultrashort-pulse scribing can produce cleaner trenches with steep sidewalls and reduced debris, which is particularly beneficial for P2 scribing, where selective removal of the perovskite and charge-transport layers must be achieved without damaging the underlying transparent conductive oxide. However, mitigation of laser-induced damage should not rely solely on the use of ultrashort pulses or on optimization of the laser fluence, pulse duration, overlap, and scanning speed. Additional practical strategies include depth-selective patterning to confine ablation to the target layer, inert gas-assisted scribing to suppress thermochemical by-products and residue redeposition, and stack engineering with thermally robust diffusion/barrier layers to inhibit ion migration and interfacial reactions under local thermal stress.[127,205,206] More fundamentally, the thermal burden associated with P2/P3 can be further reduced through scribe-minimized or scribe-free interconnection schemes, such as modified monolithic layouts incorporating diffusion–barrier formation, and mask-defined non-laser patterning.[160,207]

D. Jiang *et al.* effectively described the disadvantages of the laser scribing technique for the fabrication of conventional monolithic PSC modules.[207] In monolithic PSC modules, efficient P1, P2, and P3 line patterning is essential for attaining proper operations (Fig. 12A). During P1 scribing, where rigid transparent electrodes (FTO or ITO) are patterned, the subsequent layers are not yet deposited, so inflicting collateral damage on the upper stacks is not a concern. In contrast, P2 and P3 scribing can induce thermal and photochemical damage in adjacent layers, the redeposition of ablated material, mechanical stress, and chemical decomposition at the scribed interfaces. Localized heating may degrade the perovskite absorber, ETL/HTL, and electrodes, whereas incomplete ablation can leave conductive residues that create shunts and leakage pathways (Fig. 12B). During P2 scribing, exposure of the perovskite to hot metal and reactive species may accelerate phase changes (*e.g.*, perovskite → PbI_2), promote halide losses or ion diffusion,

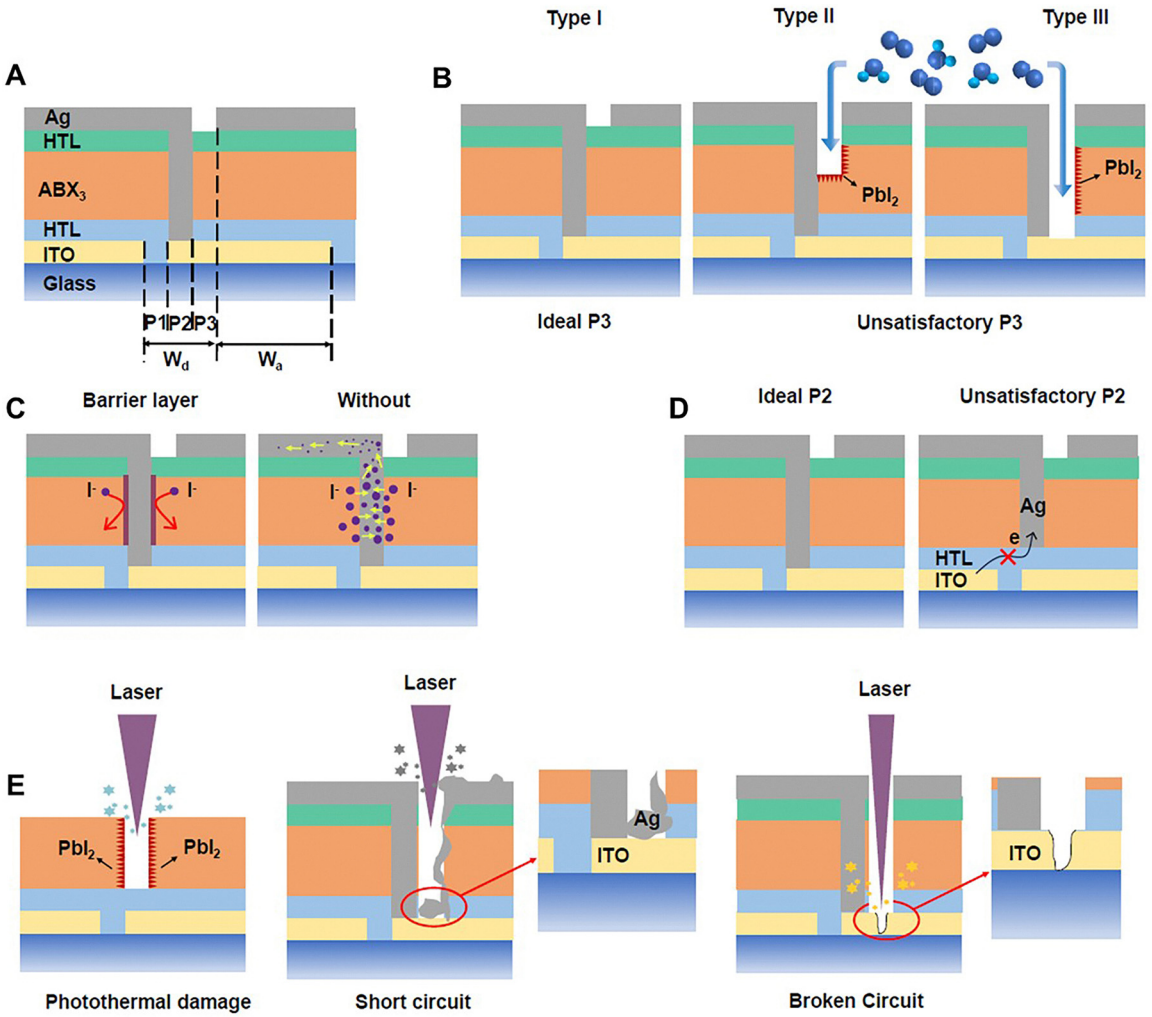

Fig. 12 Interconnection diagram for PSC modules. (A) Three patterns P1, P2 and, P3 in the "dead zone" Wd. (B)–(E) Various non-ideal interconnections in PSC modules. Reproduced with permission from Jiang *et al.*,[207] Copyright 2024 Elsevier.

and facilitate interdiffusion at buried interfaces (Fig. 12C). In addition, the misalignment of the P2 trench or insufficient removal down to the transport layer reduces the effective recombination contact, leading to series-resistance penalties and current losses (Fig. 12D). For both P2 and P3, localized thermal decomposition processes can leave PbI_2 residues, drive the metal particle redeposition procedure into the device stack, or unintentionally over-etch the bottom electrode, any of which may compromise the functionality of the constructed module (Fig. 12E).

These detrimental effects result in electrical shunting, increased nonradiative recombination effects, and reduced device efficiency and stability, which have spurred research into two complementary mitigation strategies: (1) optimizing the scribing parameters, including the laser wavelength, fluence (power density), pulse duration, repetition rate, spot size, scanning speed, and pulse overlap, and (2) introducing protective barrier layers. A strategic study conducted by Schultz *et al.* demonstrated that replacing nanosecond pulses with picosecond pulses for P2 scribing improves the performance of perovskite solar modules by reducing PbI_2 debris, minimizing thermal damage, and producing cleaner, steeper scribes with lower series resistance and higher fill factors.[208] Under ns pulses, a low fluence leaves significant residues that decrease as the fluence increases with a concomitant broadening of the scribe width; splashes and solidified rims indicate strong thermal effects. In contrast, ps scribing yields sharply defined trench edges even at low fluences (Fig. 13A and B).

Consequently, ps pulses favor a stress-assisted ablation regime with minimal collateral damage, whereas ns pulses drive thermally dominated ablations with heat diffusion, splashing, and residue formation; these distinct mechanisms are schematically illustrated in Fig. 13C. Further process-level solutions, as reported by Udalova *et al.*, explore whether directing an inert gas (*e.g.*, Ar) flow onto the scribe zone suppresses the formation of the PbI_2/PbO_x associated with photo- and thermochemical pathways (Fig. 13D).[205] Another strategy involves engineering the device stack to include a diffusion barrier.[206] Bi *et al.* introduced low-dimensional diffusion barriers based on thermally stable Al_2O_3 at the perovskite/top-electrode interface to inhibit halide

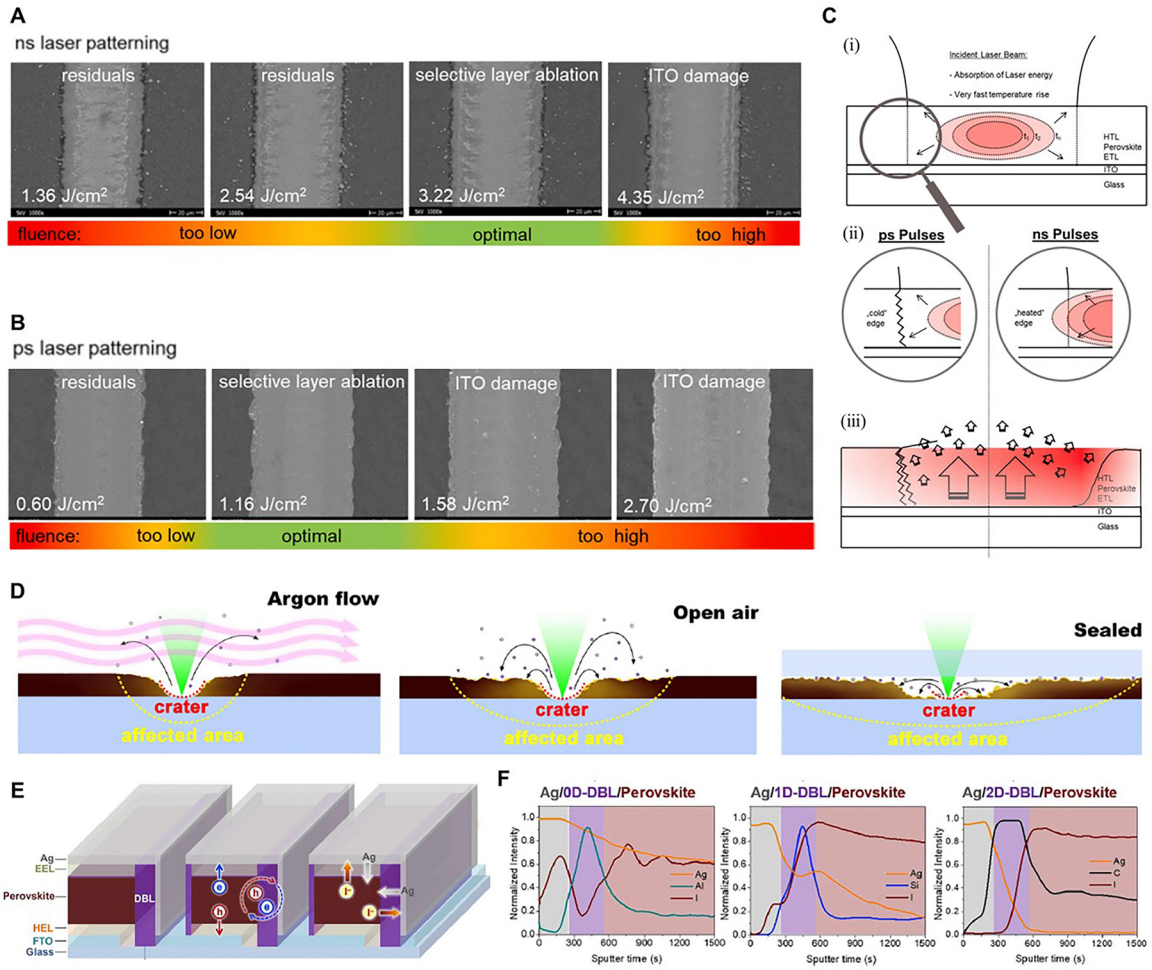

Fig. 13 Laser scribing techniques for PSC modules. SEM images of (A) ns and (B) ps laser patterned P2 scribe-lines at different fluences. (C) Simplified illustration of the ablation mechanisms postulated for ps pulses (left) and ns pulses (right). (i) Incident light absorption, (ii) heat propagation across the outer edge of the incident beam within the sample and (iii) resulting mechanisms of mechanically stress-assisted (ps, left) and thermally driven (ns, right) ablation. Reproduced with permission from Schultz *et al.*,[208] Copyright 2020 Elsevier. (D) Three cross-section schemes of the perovskite film during (left) green laser irradiation under argon flow, (middle) open ambient air, and (right) sealed with a thin glass slide are shown. Reproduced with permission from Udalova *et al.*,[205] Copyright 2020 American Chemical Society. (E) Illustration of the diffusion process and interfacial charge transfer (solid lines) and recombination (dotted circle) in PSC module (EEL is the electron extraction layer and HEL is the hole extraction layer). (F) The depth profile of diffused iodide and Ag in (left) Ag/0D-DBL/perovskite film with aluminum signal, (middle) Ag/1D-DBL/perovskite film with silicon signal, and (right) Ag/2D-DBL/perovskite film with carbon signal, respectively. Reproduced with permission from Bi *et al.*,[206] Copyright 2019 Elsevier.

migration (Fig. 13E). Notably, compared with their 0D/1D counterparts, low-temperature solution-processed 2D barrier layers more effectively block ion diffusion pathways (Fig. 13F). While these measures alleviate scribing-induced degradations, they remain technically demanding and add to the overall incurred manufacturing cost.

Compared with OSC modules, PSC modules demand distinct laser processing conditions because of their material compositions. Higher laser fluences are often required for PSCs, primarily because their crystalline perovskite absorbers are significantly denser (*e.g.*, $FAPbI_3$ at $\sim$4.2 g cm^{-3}) than the polymeric layers in OSCs (*e.g.*, PM6:Y6 at $\sim$1.2 g cm^{-3}).[209] This greater mass per unit volume necessitates more energy to reach the ablation threshold. Precise fluence control is therefore essential for achieving complete layer removal while preserving the integrity of the transparent electrode. The degradation pathways of PSCs further complicate the scribing process. In contrast with the relatively hydrophobic organic films in OSCs, perovskite absorbers are hygroscopic and chemically unstable once decomposed. Local laser heating accelerates their breakdown into PbI_2 and volatile organics, producing weak points that are highly susceptible to moisture ingresses. Grain boundaries, which are inherent to polycrystalline perovskites, serve as rapid ion migration pathways, and laser-induced defects or halide vacancies can exacerbate ion drift issues. These combined effects increase the risk of long-term instability in laser-defined interconnects.

Thus, the advantages of laser scribing in PSC modules must be coupled with stability-oriented considerations. Beyond geometrical precision and inactive area minimization, a successful implementation requires controlled decomposition residues, reduced moisture penetration pathways, and limited ion migration

triggered at grain boundaries. By addressing these issues, the well-documented benefits of laser interconnection, such as aperture ratios exceeding 90% and reduced cell-to-module losses, can be translated into PSC modules that achieve not only high efficiency but also reliable long-term operations.

4.4 Other designs for PSC modules

Laser scribing is the dominant patterning method for high-efficiency PSC modules, but its potential for inducing damage has spurred research into alternative, scribe-less interconnection strategies. One novel approach is electrochemical patterning, which involves the formation of an *in situ* conductive link without the mechanical or thermal ablation of the device layers.[210] This method exploits the intrinsic ionic conductivity of the perovskite material. As schematically described in Fig. 14A, instead of creating a P2 scribe, an electric field is applied across the SCR, which drives the migration of mobile metal ions (Ag^+) from the electrode through the device, forming conductive, metal-filamentary nanoelectrodes that bridge the top electrode of one cell to the bottom electrode of the next cell. Utilizing this electrochemical method to form the P2 connection, a total inactive area of 600 μm comprising P1, P2, and P3 was achieved, resulting in a certified module PCE of 14.1% in a 9.06 cm^2 area with a high GFF of 94.1% (Fig. 14b). However, this innovative technique presents its own challenges. The process of applying a precise voltage to each individual SCR can be complex to scale, and there are concerns that the continued diffusion of metal ions during operations could be a long-term stability risk.

Recent research has further explored several module designs to address the challenges faced by conventional laser scribing, focusing on providing improved stability, simplifying the fabrication process, and maximizing the GFF.[160,207,211–216] One approach, which was reported by H. Zhou *et al.*, improved the performance of a large-area PSC module with a uniform film at a constant low temperature by modifying the monolithic process with a novel P1.5 scribing step that created a natural diffusion barrier layer (DBL) at the interconnection (Fig. 14C).[160] The resulting modules achieved a certified PCE of 22.73% on a 14.625 cm^2 aperture with a GFF of 94.7% (Fig. 14D). With the suppressed ion interdiffusion process and metal–halide reactions resulting from the P1.5 step, the module retained more than 82% of its initial performance after 328 h of aging at 25 °C and 30–40% relative humidity (Fig. 14E). Other strategies aim to eliminate the

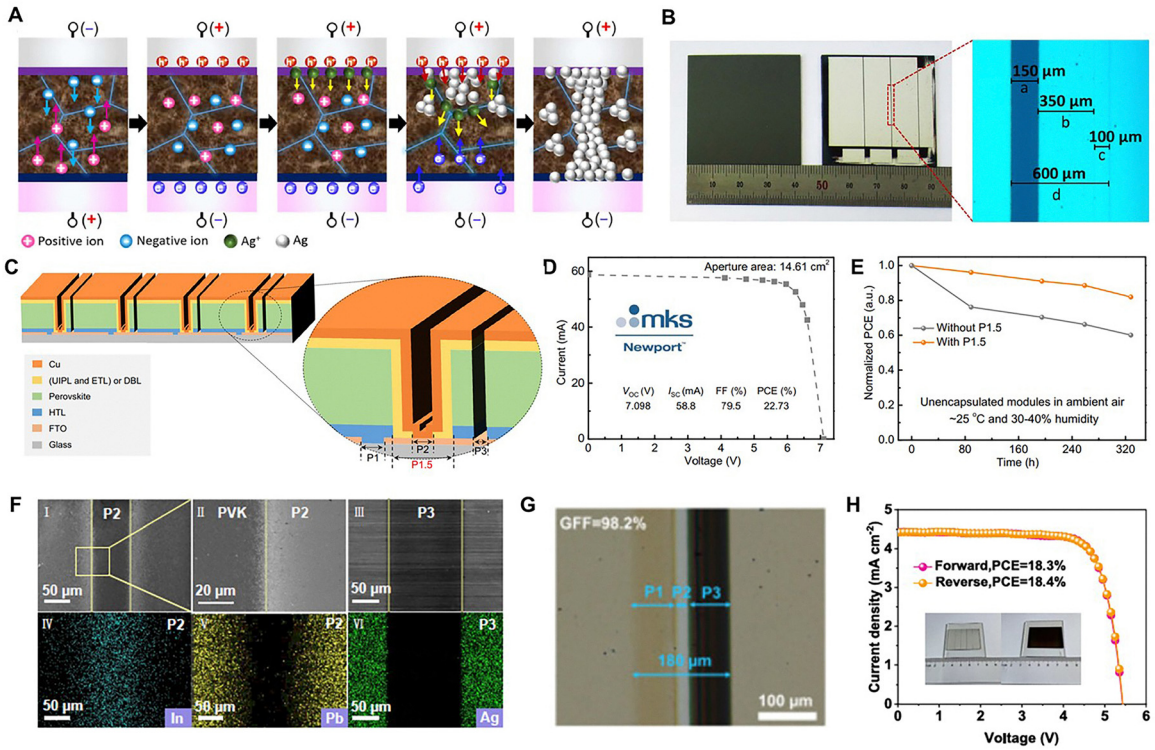

Fig. 14 Other PSC module structures. (A) Scheme of the SFN formation process *via* ion migration and electrochemical reaction. (B) (Left) Photograph of the large-area perovskite film and completed module (total area of 9.06 cm^2) and (right) optical microscopy image of a module region near the SCR ((A) width between the Ag electrodes; (B) width of the SCR; (C) width between the ITO electrodes; (D) total width of the inactive area). Reproduced with permission from Hong *et al.*,[210] Copyright 2018 American Association for the Advancement of Science. (C) Schematic diagram of the structure of a module with a DBL built at the interconnection interface by P1.5. UIPL is the upper interface passivation layer. (D) Certified quasi-steady-state *I*–*V* measurement conducted at Newport, including the performance parameters. The certified aperture area of this module is 14.61 cm^2. (E) Aging stability tracking of modules in ambient air (25 °C, 30–40% humidity). Reproduced with permission from Zhou *et al.*,[160] Copyright 2024 Nature Publishing Group. (F) SEM images (I–III) and EDS results (IV–VI) of the P2 and P3 channels prepared *via* AWM. (G) The microscopic image of the interconnection of a module with a GFF of 98%. (H) *J*–*V* curves of a PSM with an active area of 12 cm^2. Reproduced with permission from Jiang *et al.*,[207] Copyright 2024 Elsevier.

subtractive scribing procedure altogether. Jiang *et al.* developed an adjustable wire mask (AWM) to pattern all-vapor-phase–processed PSC modules without laser scribing.[207] As shown in Fig. 14F, the AWM enables clean definitions of the P2 and P3 lines, which are free of metal residue and Pb contamination within the P2 trench. Eliminating laser patterning reduced the perovskite decomposition risk and resulted in a GFF of 98% with a module PCE of 18.4% (Fig. 14G and H).

Additionally, novel interconnection geometries have been explored to push the limits of the GFF. Pakocevic *et al.* proposed a point-contact interconnection by locally removing P2 from a circular motif to establish contact between the top and bottom electrodes, thereby minimizing the inactive area and achieving a near-ideal GFF of 99%.[216] However, the PCE of their module lagged behind that of its laser- or mechanically scribed counterparts because of increased contact resistance in the interconnection region. This highlights the critical tradeoff between geometric gains and electrical performance in module architectures. Despite the development of novel module designs, the conventional series-connected architecture remains foundational to most high-performance PSCs. Even advanced concepts, such as a P4 scribe for clearing edges and narrowing the dimensions of subcells, are still derivatives of this monolithic approach.[211–214] However, degradation risks arise when laser patterning is used for P2 and P3 scribes because at P2, the scribing process can create a direct and unstable interface between the top metal electrode and the perovskite absorber, and at P3, the functional and/or perovskite layers become exposed to laser-induced thermal and photochemical stresses. The issues associated with P3 can be mitigated by tighter process control and cleaner scribed trench formation schemes, but the direct metal-layer that is contact inherent to P2 scribing is difficult to avoid without additional protective or buffer layers.

To address this constraint at the architectural level, an alternative n–i–p and p–i–n module design, analogous to the P2-free strategies explored in OSCs, has been proposed for PSCs (Fig. 15).[217] In this structure, the perovskite photoactive film remains fully continuous and unpatterned, thereby preventing direct contact between the top electrode and the adjacent layers in the interconnection region. The series connection is instead formed by the selective deposition of alternating ETLs and HTLs, creating a sequence of conventional and inverted subcells. Although such a configuration is a promising candidate for scalable manufacturing, it imposes strict requirements regarding the precise, high-resolution deposition of the charge-transport layers (HTL/ETL), which may complicate high-throughput production processes.

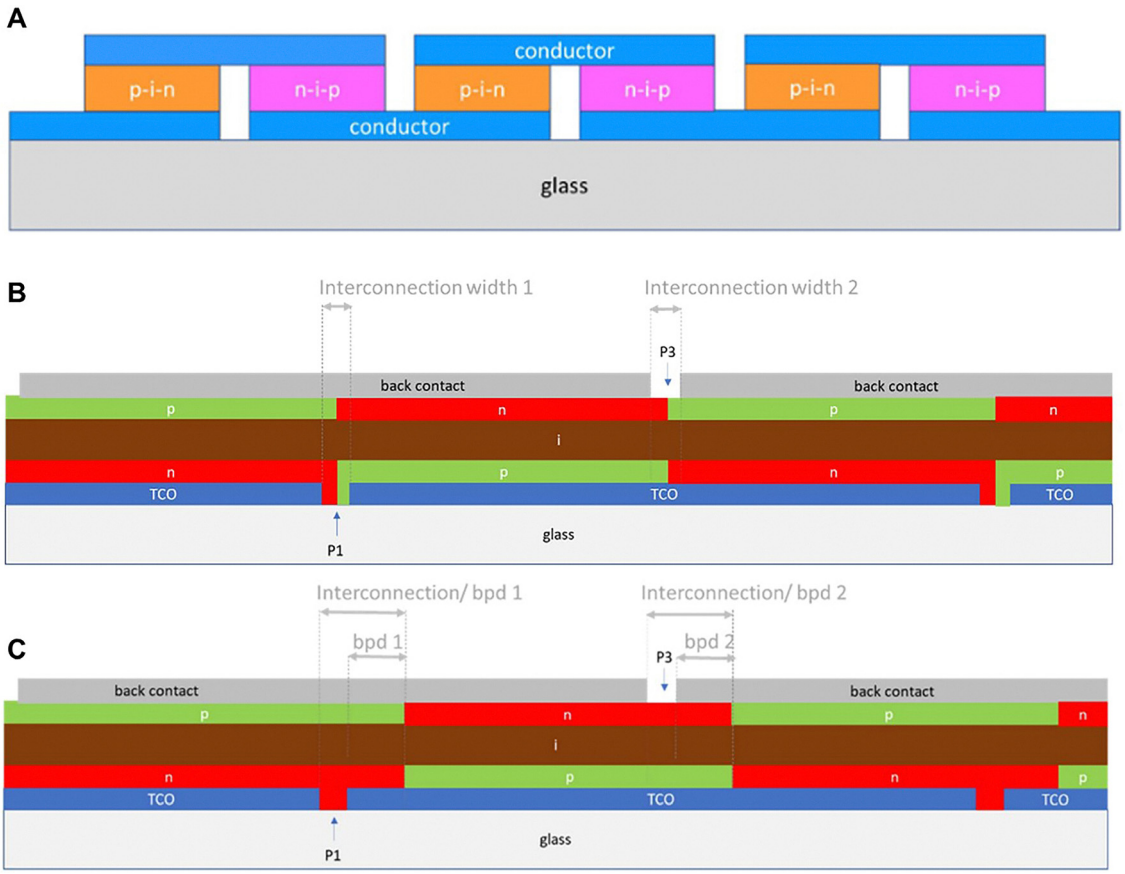

Fig. 15 Alternative PSC module designs. (A) Solar module comprising solar cells with regular (n–i–p) and inverse (p–i–n) structures side-by-side. Adjacent cells are alternatingly connected through front contact and back contact. (B) More accurate representation of this solar module. (C) Same module structure but with included bypass diodes (bpd). Reproduced with permission from Boschloo *et al.*,[217] Copyright 2023 American Chemical Society.

5. Challenges posed by monolithic OSC and PSC modules

As discussed above, the implementation of fine patterning has substantially enhanced the GFF, and continuous advancements in materials and interfacial engineering have collectively contributed to a remarkable improvement in the overall efficiency of modules. To realize highly efficient monolithic modules, patterning approaches are primarily categorized into mechanical scribing, printing patterning, and laser scribing, among which laser scribing has been predominantly adopted as the method of choice for fabricating modules with optimal efficiency.[151–170] Among these approaches, laser scribing processes employing various wavelengths (*e.g.*, 355 nm, 532 nm, 1064 nm, and 10.6 μm) have been widely adopted in the fabrication of high-efficiency OSC and PSC modules (Table S1). However, a major limitation in comparing laser scribing studies across the literature is the absence of standardized criteria for defining scribe quality and its long-term impact. In numerous studies, the effectiveness of P1, P2, or P3 patterning is inferred primarily from optical micrographs or final module PCE values, even though these indicators alone do not fully serve the electrical and durability implications of the scribed region.

To accelerate the commercialization of OSC and PSC modules, establishing a standardized characterization framework for evaluating scribing quality is therefore imperative. Currently, the field lacks uniform metrics, making it difficult to benchmark performance across different laboratories. Therefore, we propose a multi-dimensional evaluation protocol that encompasses four complementary categories: (i) geometrical and morphological metrics, including trench width precision, line edge roughness, recrystallization index, and the extent of the heat-affected zone; (ii) chemical and compositional markers, specifically a debris generation index and the quantification of decomposition products, such as PbI_2 in PSCs; (iii) electrical figures of merit, emphasizing sheet-to-sheet isolation resistance (R_{iso}) for P1, contact resistance (R_c) at the P2 interface, and leakage or shunting behavior in P3; and (iv) durability metrics, which track the evolution of these characteristics under operational or environmental aging.

In practice, such an assessment requires a synergistic combination of structural and localized electrical analyses. Geometrical and morphological features can be defined through optical microscopy, scanning electron microscopy (SEM), and profilometry for trench depth and edge profiles. Spatially resolved techniques, such as laser beam-induced current (LBIC), can analyze local resistance changes and defects by mapping short-circuit currents.[218] Furthermore, the adoption of inline *operando* diagnostics, including bright-field microscopy combined with photoluminescence (PL) and electroluminescence (EL) imaging, provides a non-destructive pathway to map inactive dead zones and identify localized shunt pathways.[219] Additionally, dark lock-in thermography (DLIT) performed under reverse bias conditions can detect localized heating caused by leakage current.[220] Examining these multi-dimensional indicators together will identify the spatial correlation between laser-induced material deformation and electrical defects, facilitating the development of high-yield manufacturing processes and accurate predictions of long-term module stability.[221]

In the monolithic designs of OSC and PSC modules, P1 patterning involves etching rigid oxide-based transparent electrodes such as ITO or FTO, for which the laser scribing process is considered the most suitable method for achieving precise patterning. Although the laser scribing process can enable fine patterning of the P2 and P3 lines, it is also associated with the drawback of inducing degradations in the surrounding areas. The potential for inflicting thermal damage when lasers with longer pulse durations are used can result in incomplete or uneven scribing effects, affecting the performance of the constructed device, as described above. From a practical perspective, the long-term and operational stability of OSC and PSC modules depends on several key factors: robust active and charge-transport materials, stable buried interfaces, damage-minimized P2/P3 patterning, protective or scribe-free module architectures, and uniform large-area processing. Because degradation often originates from unstable interconnection regions, interfacial reactions, and coating nonuniformity, meaningful progress in module stability requires the combined optimization of materials, interfaces, interconnection design, and scalable fabrication. Mechanical scribing can avoid such drawbacks of laser scribing but faces challenges that arise from its physical contact nature.[95,175] The direct force exerted by a needle or blade during the process has the potential to cause scratches, microcracks, or even the delamination of delicate, thin-film layers (Fig. 16a). As damage accumulates, the integrity of the underlying transparent electrode is compromised or parasitic shunting paths are created, severely degrading the performance and yield of the device. Another challenge is the generation of residues and particulate contamination. In contrast with ablation-based methods, mechanical scribing displaces material, which can accumulate as burrs along the edge of the scribe line or be redeposited as debris. These contaminants possibly interfere with the subsequent layer deposition steps or create electrical shorts within the interconnection region. Furthermore, mechanical scribing is constrained by an inherent resolution limit, which is determined by the physical dimensions of the scribing tip. This complicates the achievement of ultranarrow interconnection widths that are possible with other methods, thus imposing a limit on the maximum attainable GFF. Finally, ensuring long-term process reliability is a significant hurdle for industrial-scale manufacturing cases, as the physical wear suffered by the scribing tool over time can lead to process drift and a loss of reproducibility.

An ideal module fabrication strategy would aim to achieve a high GFF while eliminating the P2 scribing process. Printing-based patterning methods, including slot-die, screen, and inkjet printing, offer inherent compatibility with roll-to-roll manufacturing.[196,222–224] In this approach, functional materials are deposited only within defined regions, without the need for subsequent etching or scribing; however, film uniformity and alignment accuracy limitations generally result in lower GFFs and PCEs than those of laser-defined architectures. The fundamental challenge lies in ink engineering. Each printing method,

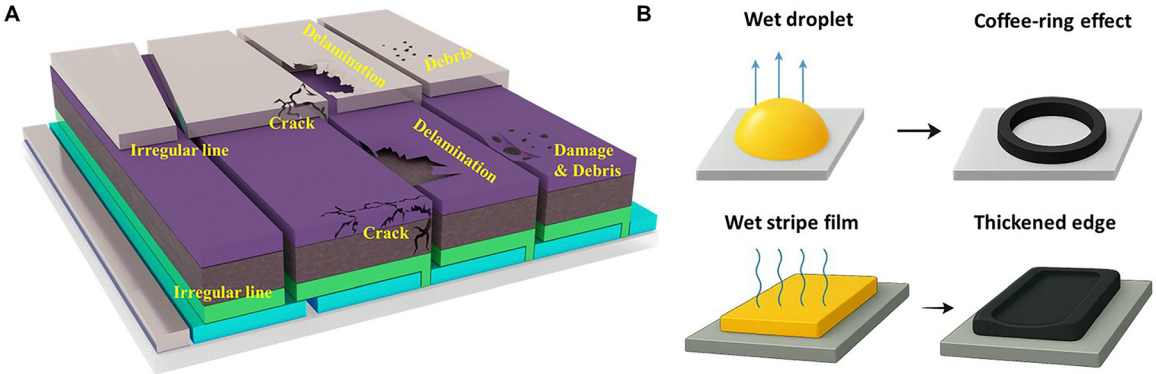

Fig. 16 Mechanical and printed patterning issues. (A) Mechanical patterning issues causing irregular lines, cracks, delamination, debris, and damage to the component layers. (B) Printed pattering issues caused by the coffee ring and inverse coffee ring effects.

be it an inkjet, screen, or slot-die approach, demands inks with precisely tailored rheological properties, including exact viscosity, surface tension, and drying kinetics values. The development of stable, jettable, or spreadable inks, especially for chemically sensitive materials such as perovskites, is a nontrivial task that directly affects the quality of the final film. Even with a well-formulated ink, achieving deposition uniformity over large areas is complicated by the complex fluid dynamics observed during drying, which frequently leads to performance-degrading defects such as the coffee-ring effect in droplet-based methods such as inkjet printing and edge effects (film thickening at the boundaries) in meniscus-based methods such as slot-die coating (Fig. 16B).

Finally, printing-based patterning faces an inherent resolution limit. The precision of this method is often constrained by physical factors such as ink spreading on the substrate, satellite droplet formation during inkjet printing, or the mesh size and ink bleeding during screen printing. This limited resolution makes it difficult to fabricate the narrow, high-precision interconnection lines that are required to achieve a high GFF, which is why a fully printed, high-efficiency module remains a significant research goal. This type of printing pattern is expected to be more useful if the conductivity of the bottom transparent electrode can be increased, allowing for the coating of wider stripes (~2 cm). Additionally, P2 lines can be uniformly patterned with widths of 300–500 μm, and these printing methods could serve as strong alternatives. Recent advances in solution engineering, surface energy modification, and process control are narrowing this gap, with prepatterned printing emerging as a promising low-cost, scalable alternative for the implementation of future modules.[196]

Fine patterning based on printing can also be realized through integration with 3D printing technology. With the recent development of 3D printing technology, D. Vak *et al.* conducted pioneering research applying this approach to OSC modules, utilizing a 3D printer integrated with a slot-die coater to deposit the P3HT:PCBM photoactive layer (Fig. 17A).[225] They successfully demonstrated P3HT films with both point and slot nozzles equipped with a 3D printer, as shown in Fig. 17B. Although the gap width between each pair of stripes was not narrow enough (2 mm) to avoid overlapping subcells, the first 3D-printed OSC module was fabricated without the P2 laser scribing process (Fig. 17C). Y.-J. Heo *et al.* demonstrated the production of large-area OSC modules using a 3D printing process without laser-scribed P2 line patterning, achieving a 4.8% PCE in a 10 cm^2 active area (Fig. 17D and E).[226]

L. Mao *et al.* developed the Maobi printing technique, which is also called the ink brush method, and it was equipped with a 3D printing machine (Fig. 17F).[227] All stacked layers were slightly shifted to ensure series connections, and the OSC modules exhibited 6.3% PCE in an active area of 18 cm^2 (Fig. 17G). S.S. Sangale *et al.* also attempted to fabricate 3D-printed PSCs with a slot-die head, and the coating conditions, such as the feeding rate, coating speed, and substrate temperature, were controlled by software (Fig. 17H).[228] In this research, the PSC module structure was completed *via* P2 mechanical scribing processes instead of direct perovskite layer patterning (Fig. 17I). The proposed PSC module achieved a PCE of up to 17.66% for an 8.64 cm^2 active area, which demonstrated that 3D printing can be applied not only to OSCs but also universally to PSCs and that it may become an important tool for future module fabrication scenarios (Fig. 17J).

Thus far, we have discussed efficient module architectures aimed at improving the GFF, providing enhanced efficiency and stability, and reducing the incurred processing costs. In view of the GFF, a commonly overlooked aspect is that silicon-based solar cells calculate the PCE on the basis of the entire wafer area, and both the cell and module scales are significantly larger than those of OSCs and PSCs. In accordance with the commercialized silicon wafer sizes of M6 (166 × 166 mm^2), M10 (182 × 182 mm^2), and M12 (210 × 210 mm^2), an area of approximately 200 cm^2 is considered the minimum size for the submodules of OSC and PSC panels.[229–231] In fact, the area that is currently used at the cell level in silicon-based solar cells has been adopted at the large-area module level in OSCs and PSCs. In practical GFF calculations, the intercell spacing, defined by a strip width of approximately 1 cm, is typically regarded as the effective module area, whereas the areas outside the active regions constituting the module are generally neglected.[232] Therefore, it is necessary to develop deposition technologies,

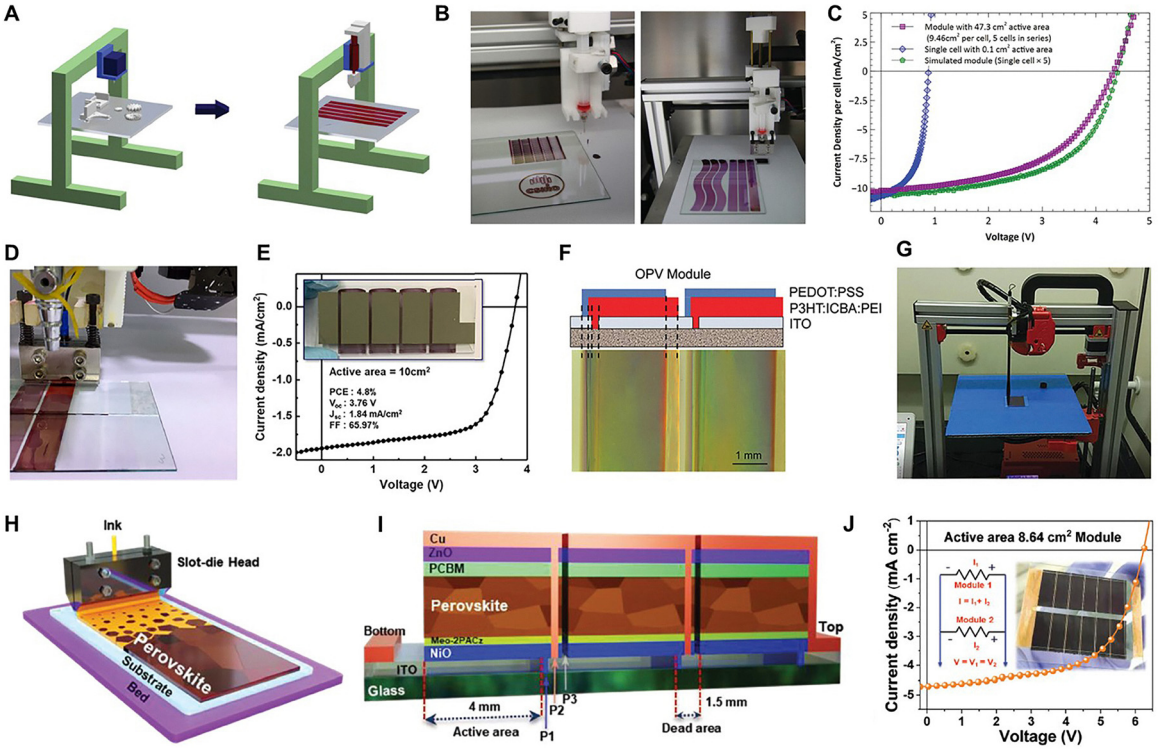

Fig. 17 The 3D printer employed for solution processing. (A) Schematic illustration of this work. A 3D printer was modified for solution processing for the fabrication of solar cells by printing new parts for modification of function of the printer. (B) Demonstration of capabilities of the modified 3D printer: (left) in printing mode with a point nozzle and (right) in coating mode with a slot nozzle. (C) *J*–*V* curve of a module with 47.3 cm^2 of active area and a single cell with 0.1 cm^2 of active area. Both devices were fabricated at the same coating conditions. Reproduced with permission from Vak *et al.*,[225] Copyright 2015 Wiley-VCH GmbH. (D) Photographic image of slot-die-coated large area photovoltaic modules during printing process and (E) corresponding current density–voltage curves of the champion cell. Reproduced with permission from Heo *et al.*,[226] Copyright 2017 American Chemical Society. (F) Schematic structure of the module (cross-sectional view) and an optical image (top view) of two adjacent cells (part of eight subcells) in the module. (G) Picture of the motor-driven, computer-controlled Maobi coating setup. Reproduced with permission from Mao *et al.*,[227] Copyright 2018 Royal Society of Chemistry. (H) Schematic of slot-die coating process. (I) Schematic architecture of minimodule with series-interconnections between subcells. (J) *J*–*V* curves of the convergence minimodule configured by connecting the upper and lower electrodes in parallel and connecting the subcells in series. The inset shows an image of the convergence minimodule and the designed electronic circuit. Reproduced with permission from Sangale *et al.*,[228] Copyright 2023 Wiley-VCH GmbH.

module architectures, and module interconnection strategies that can minimize substrate margins, similar to the approaches used in silicon-based solar cells.

Recent demonstrations have exemplified the move from laboratory-scale fabrication to the real-world deployment of large-area organic and perovskite solar modules. Following the initial park-scale implementations, Krebs and his coworkers established that organic solar cell modules can be integrated into outdoor environments with an aggregate output exceeding 1300 W over an expansive 88.2 m^2 active area, confirming their scalability and viability for the generation of distributed energy, as shown in Fig. 18A.[233] The ''infinity'' concept-based module, featuring large-scale serial connections of more than 7000 single-junction subcells, enables exceedingly high open-circuit voltages of up to 5.6 kV, as validated through a prototype-level implementation and field testing.[234] Parallel progress in perovskite technologies has provided further evidence of industrial upscaling. Han and his coworkers achieved printable triple mesoscopic PSC modules with certified efficiencies exceeding 10% over a 100 cm^2 area, culminating in the assembly of a 7 m^2 solar panel composed of these cells, as depicted in Fig. 18B.[235] Notably, a 110 m^2 perovskite PV array, fabricated *via* screen printing with individual triple mesoscopic modules exceeding 3600 cm^2 each, is manufactured by Wonder Solar, marking a tangible step toward commercial applications of large-area perovskite solar systems.[236]

To evaluate potential upscaling methodologies, it is essential to consider the multifaceted trade-offs among patterning precision, throughput, and manufacturing cost. For high-precision interconnection with minimal thermal damage, ultrafast lasers, such as picosecond or femtosecond, are generally preferred over conventional nanosecond lasers. These ultrafast lasers enable near-cold ablation, thereby reducing the heat-affected zone and preserving the structural integrity of the surrounding organic or perovskite layers. Conversely, while laser-based processes offer superior resolution, mechanical scribing holds distinct advantages in terms of high-throughput for certain module architectures. By circumventing thermal issues, it remains a viable option for rapid mass production in which processing speed is prioritized over extreme precision. Furthermore, to maximize

Fig. 18 Installations of OSC and PSC modules. (A) Photograph of the helium-filled balloon with attached solar cells and an *I*–*V*-curve (left). The photograph on the right shows three installation scenarios combined – balloon, wooden solar park structure (with just 2 stripes of solar cells), and tubes (flat, and blown-up in the background). Reproduced with permission from Espinosa *et al.*,[233] Copyright 2014 Royal Society of Chemistry. (B) Image of 7 m^2 printable perovskite solar panels. Reproduced with permission from Hu *et al.*,[235] Copyright 2017 Wiley-VCH GmbH.

cost-competitiveness, direct patterning approaches, such as inkjet printing, slot-die coating, and screen printing, should be considered. These techniques can reduce material waste and simplify processing by eliminating the redundant steps typically associated with conventional subtractive scribing methods.

The evolution from individual modules to either large single-area modules or panelized systems represents a crucial technological advance for OSC and PSC technologies. The success of this transition will determine whether these emerging photovoltaic technologies can achieve the scale, reliability, and cost-effectiveness that are required for widespread commercial adoption and if they can compete effectively with established silicon photovoltaic systems.

6. AI for the design and fabrication of OSC and PSC modules

The development of high-performance OSC and PSC modules involves navigating a complex, high-dimensional space consisting of materials, processing parameters, and device architectures. The traditional trial-and-error approaches are often slow and resource-intensive. To accelerate the path to commercialization, artificial intelligence (AI) and machine learning (ML) have emerged as powerful tools for guiding research and development processes in a more systematic, data-driven manner.[237–240] The applications of AI can be broadly categorized into three key areas, *i.e.*, material discovery, process optimization, and performance analysis, yielding commercialized manufacturing techniques, as illustrated in Fig. 19. The performance of OSCs and PSCs is fundamentally dictated by the properties of their constituent materials. AI/ML models can rapidly accelerate the discovery of new, high-performance materials through high-throughput virtual screening schemes.

In most current studies, their primary role is to prioritize promising candidates within predefined chemical spaces rather than to autonomously generate entirely new material classes. X. Cai *et al.* combined ML with high-throughput density functional theory (DFT) calculations to screen a staggering 180 038 electrically neutral compounds. This process allowed them to narrow the search to just 597 candidates with suitable stability and band gaps.[241] A. Mannodi-Kanakkithodi

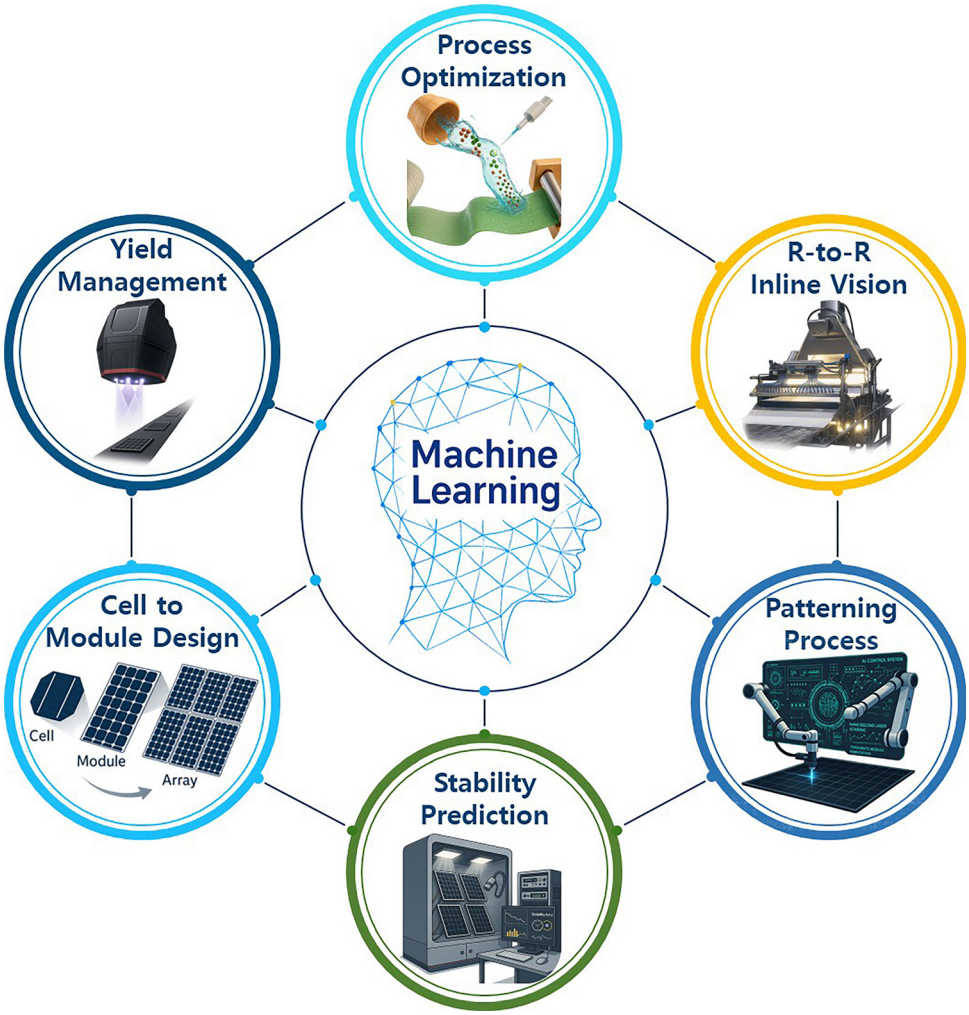

Fig. 19 Integration of AI/ML throughout the entire workflow for designing and fabricating high-performance OSC and PSC modules. The cycle includes cell-to-module design, process optimization, roll-to-roll inline vision (for quality control), precise patterning, stability prediction, and overall yield management procedures.

et al. used a data-driven framework to screen 17 955 compounds from a predicted dataset. By applying ML models to predict stability, band gap, and defect tolerance, they identified 574 promising candidates, significantly speeding up the identification of viable alloys.[242] By training on large datasets of known materials, these models can predict key properties, such as bandgaps, energy levels (HOMO/LUMO), and chemical stability, of novel candidate molecules or perovskite compositions based solely on their structures. This allows researchers to computationally screen vast chemical libraries and identify the most promising candidates for synthesis, dramatically reducing their experimental effort and time costs. More advanced inverse design approaches even allow AI to generate entirely new molecular structures that are tailored to have specific, desired sets of properties.

Implementing high-performance materials in a large-area module requires precise control over the fabrication process. The quality of a printed or coated layer, for example, depends on a multitude of parameters, including the ink formulation, coating speed, substrate temperature, and drying conditions. Bayesian optimization and other ML algorithms are exceptionally well suited for exploring this vast parameter space.[243–246] By intelligently selecting which experiments to perform next, these methods can efficiently identify the optimal processing conditions for maximizing the quality of films and the performance of devices with a minimal number of experimental runs. For monolithic cell integration, the quality of P1–P3 patterning depends on the underlying processing conditions such as the wavelength, fluence, pulse duration, repetition rate, spot size, scan speed, overlap, and gas purge in such laser scribing techniques. AI accelerates the recipe development process by learning variables that map these inputs to the scribing width, recrystallization/debris generation index, edge roughness, isolation resistance, and electrical figures of merit (*e.g.*, R_{sh}, R_s, and FF). Multiobjective Bayesian optimization searches the Pareto front to minimize the dead area and thermal budget with optimal isolation, while physics-regularized losses penalize solutions that violate basic thermal diffusion or ablation scaling conditions. Inline vision based on bright-field, PL/EL, and infrared imaging provides automatic labels for clean or

damaged scribed trenches, enabling continuous drift corrections to be implemented as the optics age or substrates vary.

For large-area solar panel arrays in real-field applications, the module design is delicately engineered to balance the resistive loss (*i.e.*, the finite TCO conductivity and bus topology) against the aperture loss (*i.e.*, the dead width of the scribe). Physics-informed ML facilitates rapid sweeps over the stripe width/pitch, P2/P3 spacing, and busbar/finger grids using differentiable proxies for the cell-to-module loss and optical transfer modeling. The constraints that must be considered include the minimum trench pitch for the yield, encapsulation keep-outs, and aesthetic targets for semitransparent/BIPV modules. The optimizer produces a range of layouts (n–i–p, p–i–n, alternating normal/inverted, and P2-free) along with the predicted PCE, GFF, and manufacturability index. In terms of industrial-scale production, AI is poised to enable smart manufacturing. By integrating *in situ* metrology (*e.g.*, cameras and spectrometers) into a roll-to-roll production line, AI models can analyze data in real time to detect defects, predict performance, and provide automated feedback for controlling and adjust process parameters on the fly.[247] This capability is critical for ensuring the high-yield, consistent production of large-area modules. For semitransparent OSC/PSC modules, AI balances the average visible transmittance (AVT) and haze against the PCE by cotuning the optical cavity thickness, transparent conductor, and scribe geometry. For flexible modules, mechanics-aware models incorporate neutral-axis placement and fatigue proxies to avoid scribe-initiated crack propagation, guiding the substrate thickness, grid reinforcement, and interconnect routing choices.

Finally, the long-term stability of modules is a primary concern for their commercial viability. AI/ML models can be trained on accelerated aging data to predict the operational lifetimes of new device architectures under various environmental stressors (*e.g.*, heat, humidity, and light).[248] This data-driven approach can significantly shorten the protracted process of stability testing. Furthermore, AI can be used for advanced diagnostics; by analyzing performance data such as *J*–*V* curves or PL images, machine learning can identify specific degradation modes or defect signatures, helping researchers rapidly diagnose and address the root causes of performance losses.[249]

7. Conclusions and outlook

Over the past two decades, advances in materials, processing methods, and architecture have rapidly elevated OSC and PSC modules from proofs of concepts to competitive thin-film technologies, positioning them as viable next-generation alternatives to silicon. However, the translation of their record-breaking small-cell efficiencies into commercially relevant, large-area modules remains a central challenge, primarily because of the cell-to-module performance gap. This review provides a comprehensive overview of the module designs and fabrication techniques that have been developed to bridge this gap, highlighting a discernible evolutionary path and persistent challenges. A monolithic, series-connected architecture has been established as the foundational design for both OSCs and PSCs, born from the necessity of mitigating the resistive losses induced by transparent conductive oxides. The implementation of this design has driven the evolution of patterning technologies, as well as mechanical, printing-defined, and laser scribing techniques. Mechanical routes, on the other hand, offer low tooling costs but face precision, damage risk, and scalability limits. Printing-defined approaches promise additive, roll-to-roll compatibility, but they demand stringent ink rheology and deposition control, and in PSCs, they are often complemented by subtractive steps. Laser scribing, which is now prevalent in record-setting modules, results in narrow P1–P3 features and high GFFs exceeding 95%, but the associated thermal/chemical liabilities (*e.g.*, PbI_2 residues and collateral damage) demand a careful selection process for the wavelength, pulse regime, and fluence, especially for hygroscopic, ion-migrating perovskites.

In response to these challenges, innovative P2-free or scribeless module architectures have emerged. These designs, which incorporate alternating n–i–p/p–i–n structures on a continuous TCO, selective active-layer deposition, and *in situ* electrochemical patterning, signify a paradigm shift, with aims of eliminating the problematic P2 scribing process entirely, maximizing the GFF and providing enhanced stability. These novel designs illustrate viable paths to lower cell-to-module losses without relying exclusively on high-energy ablative steps, but they also introduce their own set of fabrication complexities, such as the necessity for the high-resolution, selective deposition of functional layers. From a future perspective, the maturation of AI/ML across the materials discovery, process tuning, and module layout optimization domains has the potential to shorten development cycles and stabilize manufacturing procedures. The data-driven optimization of coating/printing windows and P1–P3 recipes, coupled with inline vision for closed-loop control, facilitates systematic reductions in the dead width and thermal budget while maintaining isolation. At the array level, physics-informed optimization enables the codesign of the stripe pitch, interconnect spacing, and bus topology under practical constraints (*e.g.*, yields, keep-outs, and AVT/haze targets for BIPVs). Finally, learning from accelerated aging process and *operando* diagnostics offers a principled route for predicting and extending the lifetimes of modules.

To realize the commercialization of PSCs and OSCs, a phased market entry strategy is currently unfolding. The first wave of commercialization is already emerging in the low-light and indoor photonics market. Unlike silicon, PSCs and OSCs maintain high conversion efficiencies under indoor lighting (LED, fluorescent), making them ideal power sources for internet of things (IoT) devices and self-powered electronics. Following this initial phase, specialized applications such as BIPV and VIPV present significant opportunities. Their lightweight, flexible, and semi-transparent nature allows for seamless integration into windows, facades, and curved vehicle surfaces—areas where conventional c-Si panels are structurally or aesthetically limited. For the large-scale utility market traditionally dominated by

silicon, the current research trend is shifting toward perovskite/silicon tandem solar cells. This strategy aims to surpass the Shockley–Queisser limit of single-junction cells, offering a viable path to compete with established power generation infrastructures. However, the broader commercialization of single-junction PSCs and OSCs will still require simultaneous progress in efficiency, long-term stability (beyond 20 years), and cost-competitiveness, together with advances in scalable manufacturing, encapsulation reliability, and production yield. In this sense, commercialization is likely to proceed first in niche and application-specific markets, expanding into larger energy markets as these technological and manufacturing barriers are progressively resolved.

In summary, the successful closure of the cell-to-module gap for both OSCs and PSCs is contingent upon integrative progress in terms of the following: (i) an architecture that minimizes the inactive area without incurring resistive penalties, (ii) a patterning scheme that is precise yet gentle for sensitive stacks, (iii) a deposition method that scales with uniformity and registration, and (iv) an AI-assisted fabrication strategy that turns variability into controllable parameters. A comprehensive approach for addressing the aforementioned factors has been identified as the most effective strategy for producing modules that are highly efficient, durable, and cost effective.

Author contributions

J. L., S. H. and N. J. J. conceived the idea and supervised the project. J. W. L. and Y.-H. S. wrote the first draft, including the preparation of the figures and tables. H. J. J. and E. C. C. assisted in reviewing the literature and compiling the published module results data. H. H. P. and B. J. K. provided the available discussion. K. K. assisted in preparing the figures. J. L., S. H. and N. J. J. revised the manuscript.

Conflicts of interest

There are no conflicts to declare.

Data availability

Supplementary information (SI): which includes Table S1 providing a comprehensive summary of laser scribing parameters—including various wavelengths (355 nm, 532 nm, 1064 nm, and 10.6 μm)—employed in the fabrication of high-efficiency organic and perovskite solar cell modules as reported in the literature. See DOI: https://doi.org/10.1039/d5ee07830j.

Data availability is not applicable to this article as no new data were created or analyzed in this study.

Acknowledgements

This work was supported by a Korea Institute of Energy Technology Evaluation and Planning (KETEP) and the Ministry of Climate, Energy & Environment (MCEE) of the Republic of Korea (No. 20223030010360 and RS-2025-02309702) and by a grant received from the KRICT Core project (KS2622-20). This work was also supported by a National Research Foundation of Korea (NRF) grant funded by the Korean government (MSIT) (RS-2023-00278803).

References

1 M. Srivastava, B. Ramasubramanian, U. K. Ghorui, G. K. Dalapati, V. Selvaraj, A. Kumar, S. Biring, C. S. Ribeiro, S. Ghosh, S. Krishnamurthy and S. Chakrabortty, *Energy Technol.*, 2025, **13**, 2402405.
2 A. A. Khan, C. Reichel, P. Molina, L. Friedrich, D. M. Subasi, H. Neuhaus and S. Nold, *Sol. Energy Mater. Sol. Cells*, 2024, **269**, 112724.
3 A. Aleksandra, B. P. Sara, J. Małgorzata, B. Brian, P. Davide and C. Miguel, *Prog. Photovoltaics*, 2024, **32**, 607–622.
4 E. Ravishankar, R. E. Booth, C. Saravitz, H. Sederoff, H. W. Ade and B. T. O'Connor, *Joule*, 2020, **4**, 490–506.
5 N. A. Ludin, N. I. Mustafa, M. M. Hanafiah, M. A. Ibrahim, M. Asri Mat Teridi, S. Sepeai, A. Zaharim and K. Sopian, *Renewable Sustainable Energy Rev.*, 2018, **96**, 11–28.
6 N. Li, X. Niu, Q. Chen and H. Zhou, *Chem. Soc. Rev.*, 2020, **49**, 8235–8286.
7 C. Battaglia, A. Cuevas and S. De Wolf, *Energy Environ. Sci.*, 2016, **9**, 1552–1576.
8 A. R. Zanatta, *Results Opt.*, 2022, **9**, 100320.
9 A. M. Oni, A. S. M. Mohsin, M. M. Rahman and M. B. Hossain Bhuian, *Energy Rep.*, 2024, **11**, 3345–3366.
10 M. Di Sabatino, R. Hendawi and A. S. Garcia, *Crystals*, 2024, **14**, 167.
11 X. Wang, X. Tian, X. Chen, L. Ren and C. Geng, *Sol. Energy Mater. Sol. Cells*, 2022, **248**, 111976.
12 S. Pizzini, *Sol. Energy Mater. Sol. Cells*, 2010, **94**, 1528–1533.
13 F. Rehman, I. H. Syed, S. Khanam, S. Ijaz, H. Mehmood, M. Zubair, Y. Massoud and M. Q. Mehmood, *Energy Adv.*, 2023, **2**, 1239–1262.
14 P. P. Boix, K. Nonomura, N. Mathews and S. G. Mhaisalkar, *Mater. Today*, 2014, **17**, 16–23.
15 N. Marinova, S. Valero and J. L. Delgado, *J. Colloid Interface Sci.*, 2017, **488**, 373–389.
16 S. Bi, X. Leng, Y. Li, Z. Zheng, X. Zhang, Y. Zhang and H. Zhou, *Adv. Mater.*, 2019, **31**, e1805708.
17 A. Machin and F. Marquez, *Materials*, 2024, **17**, 1165.
18 M. Riede, D. Spoltore and K. Leo, *Adv. Energy Mater.*, 2020, **11**, 2002653.
19 A. Distler, C. J. Brabec and H. J. Egelhaaf, *Prog. Photovoltaics*, 2020, **29**, 24–31.
20 P. Zhu, C. Chen, J. Dai, Y. Zhang, R. Mao, S. Chen, J. Huang and J. Zhu, *Adv. Mater.*, 2024, **36**, e2307357.
21 X. Liu, J. Zhang, B. Wang, G. Tong, J. Yang, Y. Shi, Z. Chen, L. K. Ono, Y. Jiang and Y. Qi, *Joule*, 2025, **9**, 102056.
22 I. Burgués-Ceballos, L. Lucera, P. Tiwana, K. Ocytko, L. W. Tan, S. Kowalski, J. Snow, A. Pron, H. Bürckstümmer, N. Blouin and G. Morse, *Joule*, 2021, **5**, 2261–2272.

23 M. Giannouli and K. Sudhakar, *Int. J. Photoenergy*, 2021, **2021**, 1–19.
24 T. D. Siegler, A. Dawson, P. Lobaccaro, D. Ung, M. E. Beck, G. Nilsen and L. L. Tinker, *ACS Energy Lett.*, 2022, **7**, 1728–1734.
25 J. Bing, L. G. Caro, H. P. Talathi, N. L. Chang, D. R. McKenzie and A. W. Y. Ho-Baillie, *Joule*, 2022, **6**, 1446–1474.
26 J. Liu, T. Ye, D. Yu, S. F. Liu and D. Yang, *Angew. Chem., Int. Ed.*, 2023, **62**, e202307225.
27 M. Seri, F. Mercuri, G. Ruani, Y. Feng, M. Li, Z.-X. Xu and M. Muccini, *Energy Technol.*, 2021, **9**, 2000901.
28 B. Kang and F. Yan, *Energy Environ. Sci.*, 2025, **18**, 3917–3954.
29 F. Li, F. R. Lin and A. K. Jen, *Adv. Mater.*, 2024, **36**, e2307161.
30 S. Hong, G. Kim, B. Park, J.-H. Kim, J. Kim, Y. Pak, J. Kim, S. Kwon and K. Lee, *J. Mater. Chem. A*, 2020, **8**, 18659–18667.
31 E. M. Hutter, M. C. Gelvez-Rueda, A. Osherov, V. Bulovic, F. C. Grozema, S. D. Stranks and T. J. Savenije, *Nat. Mater.*, 2017, **16**, 115–120.
32 P. Cheng and Y. Yang, *Acc. Chem. Res.*, 2020, **53**, 1218–1228.
33 M. H. Miah, M. U. Khandaker, M. B. Rahman, E. A. M. Nur and M. A. Islam, *RSC Adv.*, 2024, **14**, 15876–15906.
34 M. Jahandar, S. Kim, Y. H. Kim and D. C. Lim, *Adv. Energy Sustainability Res.*, 2022, **4**, 2200117.
35 M. A. Green, E. D. Dunlop, M. Yoshita, N. Kopidakis, K. Bothe, G. Siefer and X. Hao, *Prog. Photovoltaics*, 2023, **31**, 651–663.
36 M. A. Green, E. D. Dunlop, M. Yoshita, N. Kopidakis, K. Bothe, G. Siefer, X. Hao and J. Y. Jiang, *Prog. Photovoltaics*, 2025, **33**, 795–810.
37 F. C. Krebs, *Sol. Energy Mater. Sol. Cells*, 2009, **93**, 394–412.
38 F. C. Krebs, *Sol. Energy Mater. Sol. Cells*, 2009, **93**, 1636–1641.
39 S. Razza, F. Di Giacomo, F. Matteocci, L. Cinà, A. L. Palma, S. Casaluci, P. Cameron, A. D'Epifanio, S. Licoccia, A. Reale, T. M. Brown and A. Di Carlo, *J. Power Sources*, 2015, **277**, 286–291.
40 R. Basu, F. Gumpert, J. Lohbreier, P.-O. Morin, V. Vohra, Y. Liu, Y. Zhou, C. J. Brabec, H.-J. Egelhaaf and A. Distler, *Joule*, 2024, **8**, 970–978.
41 B. Zhang, F. Yang and Y. Li, *Small Sci.*, 2023, **3**, 2300004.
42 H. Gu, J. Zhu, H. Chen, G. Zeng, X. Chen, X. Tang, J. Xia, T. Zhang, B. Zhang, J. Zhang, J. Ding, Y. Li and Y. Li, *Giant*, 2024, **18**, 100286.
43 W. I. Jeong, J. Lee, S. Y. Park, J. W. Kang and J. J. Kim, *Adv. Funct. Mater.*, 2010, **21**, 343–347.
44 S. S. Sangale, H. Son, S. W. Park, P. Patil, T. K. Lee, S. N. Kwon and S. I. Na, *Adv. Mater.*, 2025, **37**, e2420093.
45 N. K. Tran Ho, C. C. Tseng, C. T. Wang, Y. J. Chen, S. H. Lin, Y. R. Lin, L. S. Yang, V. Q. Le, H. F. Meng, Y. C. Chao, H. W. Zan and S. F. Horng, *Sol. RRL*, 2024, **8**, 2400101.
46 Y. Galagan, H. Fledderus, H. Gorter, H. H. t Mannetje, S. Shanmugam, R. Mandamparambil, J. Bosman, J. E. J. M. Rubingh, J. P. Teunissen, A. Salem, I. G. de Vries, R. Andriessen and W. A. Groen, *Energy Technol.*, 2015, **3**, 834–842.
47 F. Di Giacomo, L. A. Castriotta, F. Matteocci and A. Di Carlo, *Adv. Energy Mater.*, 2024, **14**, 2400115.
48 L. Lucera, F. Machui, P. Kubis, H. D. Schmidt, J. Adams, S. Strohm, T. Ahmad, K. Forberich, H. J. Egelhaaf and C. J. Brabec, *Energy Environ. Sci.*, 2016, **9**, 89–94.
49 J. D. Servaites, M. A. Ratner and T. J. Marks, *Energy Environ. Sci.*, 2011, **4**, 4410–4422.
50 M. A. Green, A. Ho-Baillie and H. J. Snaith, *Nat. Photonics*, 2014, **8**, 506–514.
51 B. Parida, A. Singh, A. K. Kalathil Soopy, S. Sangaraju, M. Sundaray, S. Mishra, S. F. Liu and A. Najar, *Adv. Sci.*, 2022, **9**, e2200308.
52 M. Z. Li, C. C. Lee, S. Biring, I. S. Hsu, D. Luo, R. Estrada, Y. S. Wu, C. C. Yang and S. W. Liu, *Sol. RRL*, 2020, **5**, 2000564.
53 H. Li, J. Zhou, L. Tan, M. Li, C. Jiang, S. Wang, X. Zhao, Y. Liu, Y. Zhang, Y. Ye, W. Tress and C. Yi, *Sci. Adv.*, 2022, **8**, eabo7422.
54 J. Lee, K. Lee, K. Kim and N.-G. Park, *Sol. RRL*, 2022, **6**, 2200623.
55 N. S. Kang, B.-K. Ju and J.-W. Yu, *Sol. Energy Mater. Sol. Cells*, 2013, **116**, 219–223.
56 F. C. Krebs, T. Tromholt and M. Jorgensen, *Nanoscale*, 2010, **2**, 873–886.
57 J. García Cerrillo, A. Distler, F. Matteocci, K. Forberich, M. Wagner, R. Basu, L. A. Castriotta, F. Jafarzadeh, F. Brunetti, F. Yang, N. Li, A. N. Corpus-Mendoza, A. Di Carlo, C. J. Brabec and H.-J. Egelhaaf, *Sol. RRL*, 2023, **8**, 2300767.
58 F. Ye, Z. Chen, X. Zhao, J. Chen and X. Yang, *Adv. Funct. Mater.*, 2015, **25**, 4453–4461.
59 E. Pascual-San-José, G. Sadoughi, L. Lucera, M. Stella, E. Martínez-Ferrero, G. E. Morse, M. Campoy-Quiles and I. Burgués-Ceballos, *J. Mater. Chem. A*, 2020, **8**, 9882–9895.
60 N. Agrawal, M. Zubair Ansari, A. Majumdar, R. Gahlot and N. Khare, *Sol. Energy Mater. Sol. Cells*, 2016, **157**, 960–965.
61 C. S. Pathak, H. Choi, H. Kim, J. Lim, S.-K. Cho, D. S. Ham and S. Song, *Sol. RRL*, 2024, **8**, 2300860.
62 M. Yang, D. H. Kim, T. R. Klein, Z. Li, M. O. Reese, B. J. Tremolet de Villers, J. J. Berry, M. F. A. M. van Hest and K. Zhu, *ACS Energy Lett.*, 2018, **3**, 322–328.
63 A. Cheknane, H. S. Hilal, F. Djeffal, B. Benyoucef and J.-P. Charles, *Microelectron. J.*, 2008, **39**, 1173–1180.
64 S. Haas, S. Krumscheid, A. Bauer, A. Lambertz and U. Rau, *Prog. Photovoltaics*, 2012, **21**, 972–979.
65 F. De Rossi, J. A. Baker, D. Beynon, K. E. A. Hooper, S. M. P. Meroni, D. Williams, Z. Wei, A. Yasin, C. Charbonneau, E. H. Jewell and T. M. Watson, *Adv. Mater. Technol.*, 2018, **3**, 1800156.
66 A. Priyadarshi, L. J. Haur, P. Murray, D. Fu, S. Kulkarni, G. Xing, T. C. Sum, N. Mathews and S. G. Mhaisalkar, *Energy Environ. Sci.*, 2016, **9**, 3687–3692.
67 J. Yang, D. Vak, N. Clark, J. Subbiah, W. W. H. Wong, D. J. Jones, S. E. Watkins and G. Wilson, *Sol. Energy Mater. Sol. Cells*, 2013, **109**, 47–55.
68 R. Sun, Q. Wu, J. Guo, T. Wang, Y. Wu, B. Qiu, Z. Luo, W. Yang, Z. Hu, J. Guo, M. Shi, C. Yang, F. Huang, Y. Li and J. Min, *Joule*, 2020, **4**, 407–419.

69 J. Wang, Y. Wang, M. Du, Y. Yu, C. Wang, W. Wang, Q. Guo, Y. Cui, S. Zhang and J. Hou, *Energy Environ. Sci.*, 2024, **17**, 8368–8378.
70 H. B. Lee, A. Mohamed, N. Kumar, N. H. Zain Karimy, V. V. Satale, B. Tyagi, D. H. Kim and J. W. Kang, *Small Methods*, 2025, **9**, 2400850.
71 F. Matteocci, S. Razza, F. Di Giacomo, S. Casaluci, G. Mincuzzi, T. M. Brown, A. D'Epifanio, S. Licoccia and A. Di Carlo, *Phys. Chem. Chem. Phys.*, 2014, **16**, 3918–3923.
72 Y. Jeong, Y. Kim, H. Lee, S. Ko, S. S. Ham, H. R. Jung, J. H. Choi, W. M. Kim, J. H. Jeong, S. Yoon, D. J. Hwang and G. Y. Kim, *Sol. RRL*, 2024, **8**, 2301040.
73 E. Feng, C. Zhang, J. Chang, Y. Han, H. Li, Q. Luo, C.-Q. Ma, H.-L. Yip, L. Ding and J. Yang, *Cell Rep. Phys. Sci.*, 2024, **5**, 101883.
74 G. Yu, J. Gao, J. C. Hummelen, F. Wudl and A. J. Heeger, *Science*, 1995, **270**, 1789–1791.
75 D. Angmo, M. Hösel and F. C. Krebs, *Sol. Energy Mater. Sol. Cells*, 2012, **107**, 329–336.
76 M. Helgesen, J. E. Carlé, B. Andreasen, M. Hösel, K. Norrman, R. Søndergaard and F. C. Krebs, *Polym. Chem.*, 2012, **3**, 2649–2655.
77 M. Hösel, R. R. Søndergaard, M. Jørgensen and F. C. Krebs, *Adv. Energy Mater.*, 2014, **4**, 1301625.
78 D. Angmo and F. C. Krebs, *Energy Technol.*, 2015, **3**, 774–783.
79 J. D. Chen, C. Cui, Y. Q. Li, L. Zhou, Q. D. Ou, C. Li, Y. Li and J. X. Tang, *Adv. Mater.*, 2015, **27**, 1035–1041.
80 Z. He, B. Xiao, F. Liu, H. Wu, Y. Yang, S. Xiao, C. Wang, T. P. Russell and Y. Cao, *Nat. Photonics*, 2015, **9**, 174–179.
81 S. Hong, H. Kang, G. Kim, S. Lee, S. Kim, J. H. Lee, J. Lee, M. Yi, J. Kim, H. Back, J. R. Kim and K. Lee, *Nat. Commun.*, 2016, **7**, 10279.
82 C. Zhan, X. Zhang and J. Yao, *RSC Adv.*, 2015, **5**, 93002–93026.
83 J. Zhang, H. S. Tan, X. Guo, A. Facchetti and H. Yan, *Nat. Energy*, 2018, **3**, 720–731.
84 J. Yuan, Y. Zhang, L. Zhou, G. Zhang, H.-L. Yip, T.-K. Lau, X. Lu, C. Zhu, H. Peng, P. A. Johnson, M. Leclerc, Y. Cao, J. Ulanski, Y. Li and Y. Zou, *Joule*, 2019, **3**, 1140–1151.
85 J. Yuan and Y. Zou, *Org. Electron.*, 2022, **102**, 106436.
86 R. Zeng, F. Han, W. Zhong, M. Zhang, S. Tan, Y. Lin, J. Deng, G. Zhou, L. Kan, L. Zhu, X. Gao, J. Zhu, W. Zhao, S. Xu, X. Xue, B. Hao, Z. Zhou, X. Wu, C. Wang, Z. Fink, Z. Tang, H. Jing, T. P. Russell, Y. Zhang and F. Liu, *Adv. Mater.*, 2025, **37**, e2501812.
87 W. Shi, Q. Han, W. Zhao, R. Wang, L. Li, G. Song, X. Chen, G. Long, Z. Yao, Y. Lu, C. Li, X. Wan and Y. Chen, *Energy Environ. Sci.*, 2025, **18**, 5356–5364.
88 H. Chen, Y. Huang, R. Zhang, H. Mou, J. Ding, J. Zhou, Z. Wang, H. Li, W. Chen, J. Zhu, Q. Cheng, H. Gu, X. Wu, T. Zhang, Y. Wang, H. Zhu, Z. Xie, F. Gao, Y. Li and Y. Li, *Nat. Mater.*, 2025, **24**, 444–453.
89 C. Chen, L. Wang, W. Xia, K. Qiu, C. Guo, Z. Gan, J. Zhou, Y. Sun, D. Liu, W. Li and T. Wang, *Nat. Commun.*, 2024, **15**, 6865.
90 C. Li, J. Song, H. Lai, H. Zhang, R. Zhou, J. Xu, H. Huang, L. Liu, J. Gao, Y. Li, M. H. Jee, Z. Zheng, S. Liu, J. Yan, X. K. Chen, Z. Tang, C. Zhang, H. Y. Woo, F. He, F. Gao, H. Yan and Y. Sun, *Nat. Mater.*, 2025, **24**, 433–443.
91 Z. Jin, C. Shen, H. Hu, C. Han, Y. Bai, M. Yang, Q. Liu and Z. Ge, *Energy Environ. Sci.*, 2025, **18**, 5552–5563.
92 T. Chen, X. Zheng, D. Wang, Y. Zhu, Y. Ouyang, J. Xue, M. Wang, S. Wang, W. Ma, C. Zhang, Z. Ma, S. Li, L. Zuo and H. Chen, *Adv. Mater.*, 2024, **36**, e2308061.
93 J.-H. Lee, W.-S. Chung, N.-G. Park and K. Kim, *Curr. Appl. Phys.*, 2010, **10**, e185–e188.
94 P.-T. Tsai, K.-C. Yu, C.-J. Chang, S.-F. Horng and H.-F. Meng, *Org. Electron.*, 2015, **22**, 166–172.
95 J. G. Tait, L. La Notte, D. Melkonyan, R. Gehlhaar, D. Cheyns, A. Reale and P. Heremans, *Sol. Energy Mater. Sol. Cells*, 2016, **144**, 493–499.
96 S. Dong, K. Zhang, X. Liu, Q. Yin, H.-L. Yip, F. Huang and Y. Cao, *Sci. China: Chem.*, 2018, **62**, 67–73.
97 F. C. Krebs and K. Norrman, *ACS Appl. Mater. Interfaces*, 2010, **2**, 877–887.
98 Y. Galagan, I. G. de Vries, A. P. Langen, R. Andriessen, W. J. H. Verhees, S. C. Veenstra and J. M. Kroon, *Chem. Eng. Process.*, 2011, **50**, 454–461.
99 P. Kopola, T. Aernouts, R. Sliz, S. Guillerez, M. Ylikunnari, D. Cheyns, M. Välimäki, M. Tuomikoski, J. Hast, G. Jabbour, R. Myllylä and A. Maaninen, *Sol. Energy Mater. Sol. Cells*, 2011, **95**, 1344–1347.
100 C. M. Amb, M. R. Craig, U. Koldemir, J. Subbiah, K. R. Choudhury, S. A. Gevorgyan, M. Jorgensen, F. C. Krebs, F. So and J. R. Reynolds, *ACS Appl. Mater. Interfaces*, 2012, **4**, 1847–1853.
101 T. R. Andersen, H. F. Dam, M. Hösel, M. Helgesen, J. E. Carlé, T. T. Larsen-Olsen, S. A. Gevorgyan, J. W. Andreasen, J. Adams, N. Li, F. Machui, G. D. Spyropoulos, T. Ameri, N. Lemaître, M. Legros, A. Scheel, D. Gaiser, K. Kreul, S. Berny, O. R. Lozman, S. Nordman, M. Välimäki, M. Vilkman, R. R. Søndergaard, M. Jørgensen, C. J. Brabec and F. C. Krebs, *Energy Environ. Sci.*, 2014, **7**, 2925–2933.
102 N. Li, P. Kubis, K. Forberich, T. Ameri, F. C. Krebs and C. J. Brabec, *Sol. Energy Mater. Sol. Cells*, 2014, **120**, 701–708.
103 Y. F. Shen, H. Zhang, J. Zhang, C. Tian, Y. Shi, D. Qiu, Z. Zhang, K. Lu and Z. Wei, *Adv. Mater.*, 2023, **35**, e2209030.
104 S. Hong, J. Lee, H. Kang and K. Lee, *Sol. Energy Mater. Sol. Cells*, 2013, **112**, 27–35.
105 G. Wang, M. A. Adil, J. Zhang and Z. Wei, *Adv. Mater.*, 2019, **31**, e1805089.
106 B. Lee, L. Lahann, Y. Li and S. R. Forrest, *Sustainable Energy Fuels*, 2020, **4**, 5765–5772.
107 C. Kapnopoulos, A. Zachariadis, E. Mekeridis, S. Kassavetis, C. Gravalidis, A. Laskarakis and S. Logothetidis, *Materials*, 2022, **15**, 8218.
108 E. Jiang, C. Baretzky, D. Müller, O. Fischer, B. Zimmermann and U. Würfel, *Sol. RRL*, 2024, **8**, 2400303.
109 C. Girotto, D. Moia, B. P. Rand and P. Heremans, *Adv. Funct. Mater.*, 2010, **21**, 64–72.

110 X. Peng, J. Yuan, S. Shen, M. Gao, A. S. R. Chesman, H. Yin, J. Cheng, Q. Zhang and D. Angmo, *Adv. Funct. Mater.*, 2017, **27**, 1703704.
111 G. Park, Y. Cho, S. Jeong, J. Park, S.-J. Yoon and C. Yang, *J. Mater. Chem. A*, 2023, **11**, 12185–12193.
112 S. Hong, M. Yi, H. Kang, J. Kong, W. Lee, J.-R. Kim and K. Lee, *Sol. Energy Mater. Sol. Cells*, 2014, **126**, 107–112.
113 S. Hong, B. Park, C. Balamurugan, J. Lee and S. Kwon, *Heliyon*, 2023, **9**, e18209.
114 X. Zhou, X. Liu, X. Dong, T. Liu, K. Feng, Q. Luo, R. Tian, S. Xiong, L. Sun, J. Chen, Z. Zhang, R. Wei and Y. Zhou, *Adv. Funct. Mater.*, 2025, **35**, e07399.
115 C. Tian, J. Zhang, Y. Shen, H. Zhang, Z. Zhang, D. Qiu, L. Zhang and Z. Wei, *Sol. RRL*, 2023, **7**, 2300349.
116 L. Li, Z. Huang, X. Meng, Z. Xing, B. Fan, J. Li and Y. Chen, *Adv. Mater.*, 2024, **36**, e2310752.
117 K. Kim, J.-h Jang, S. Hong, H. Kang and J. Lee, *J. Mater. Res. Technol.*, 2024, **31**, 3480–3488.
118 P. Kubis, J. Winter, A. Gavrilova, M. Hennel, S. Schlosser, I. Richter, A. Distler, M. Heyder, S. Kery, P. Lenk, S. Geiger, C. J. Brabec, H. P. Huber and H. J. Egelhaaf, *Prog. Photovoltaics*, 2019, **27**, 479–490.
119 B. Zhang, W. Chen, H. Chen, G. Zeng, R. Zhang, H. Li, Y. Wang, X. Gu, W. Sun, H. Gu, F. Gao, Y. Li and Y. Li, *Energy Environ. Sci.*, 2024, **17**, 2935–2944.
120 Z. Jia, Z. Chen, X. Chen, J. Yao, B. Yan, R. Sheng, H. Zhu and Y. Yang, *Photonics Res.*, 2021, **9**, 324–330.
121 D. Wang, Y. Li, G. Zhou, E. Gu, R. Xia, B. Yan, J. Yao, H. Zhu, X. Lu, H.-L. Yip, H. Chen and C.-Z. Li, *Energy Environ. Sci.*, 2022, **15**, 2629–2637.
122 P. Kubis, N. Li, T. Stubhan, F. Machui, G. J. Matt, M. M. Voigt and C. J. Brabec, *Prog. Photovoltaics*, 2013, **23**, 238–246.
123 G. D. Spyropoulos, P. Kubis, N. Li, D. Baran, L. Lucera, M. Salvador, T. Ameri, M. M. Voigt, F. C. Krebs and C. J. Brabec, *Energy Environ. Sci.*, 2014, **7**, 3284–3290.
124 N. Gasparini, L. Lucera, M. Salvador, M. Prosa, G. D. Spyropoulos, P. Kubis, H.-J. Egelhaaf, C. J. Brabec and T. Ameri, *Energy Environ. Sci.*, 2017, **10**, 885–892.
125 J. Y. Fan, Z. X. Liu, J. Rao, K. Yan, Z. Chen, Y. Ran, B. Yan, J. Yao, G. Lu, H. Zhu, C. Z. Li and H. Chen, *Adv. Mater.*, 2022, **34**, e2110569.
126 Z. Liu, Y. Fu, J. Wu, X. Yi, M. Zhao, M. Huang, J. Liu and Z. Xie, *Adv. Funct. Mater.*, 2024, **35**, 2401558.
127 G. D. Spyropoulos, C. O. Ramirez Quiroz, M. Salvador, Y. Hou, N. Gasparini, P. Schweizer, J. Adams, P. Kubis, N. Li, E. Spiecker, T. Ameri, H.-J. Egelhaaf and C. J. Brabec, *Energy Environ. Sci.*, 2016, **9**, 2302–2313.
128 J. Lee, H. Back, J. Kong, H. Kang, S. Song, H. Suh, S.-O. Kang and K. Lee, *Energy Environ. Sci.*, 2013, **6**, 1152–1157.
129 I. Etxebarria, J. G. Tait, R. Gehlhaar, R. Pacios and D. Cheyns, *Org. Electron.*, 2013, **14**, 430–435.
130 L. Meng, J. You and Y. Yang, *Nat. Commun.*, 2018, **9**, 5265.
131 G. Yang, C. Deng, C. Li, T. Zhu, D. Liu, Y. Bai, Q. Chen, J. Huang and G. Li, *Nat. Photonics*, 2025, **19**, 913–924.
132 E. Aydin, T. G. Allen, M. De Bastiani, A. Razzaq, L. Xu, E. Ugur, J. Liu and S. De Wolf, *Science*, 2024, **383**, eadh3849.
133 C. Yang, W. Hu, J. Liu, C. Han, Q. Gao, A. Mei, Y. Zhou, F. Guo and H. Han, *Light: Sci. Appl.*, 2024, **13**, 227.
134 A. Kojima, K. Teshima, Y. Shirai and T. Miyasaka, *J. Am. Chem. Soc.*, 2009, **131**, 6050–6051.
135 H. S. Kim, C. R. Lee, J. H. Im, K. B. Lee, T. Moehl, A. Marchioro, S. J. Moon, R. Humphry-Baker, J. H. Yum, J. E. Moser, M. Gratzel and N. G. Park, *Sci. Rep.*, 2012, **2**, 591.
136 N. J. Jeon, J. H. Noh, Y. C. Kim, W. S. Yang, S. Ryu and S. I. Seok, *Nat. Mater.*, 2014, **13**, 897–903.
137 N. J. Jeon, J. H. Noh, W. S. Yang, Y. C. Kim, S. Ryu, J. Seo and S. I. Seok, *Nature*, 2015, **517**, 476–480.
138 J. J. Yoo, G. Seo, M. R. Chua, T. G. Park, Y. Lu, F. Rotermund, Y. K. Kim, C. S. Moon, N. J. Jeon, J. P. Correa-Baena, V. Bulovic, S. S. Shin, M. G. Bawendi and J. Seo, *Nature*, 2021, **590**, 587–593.
139 P. Zhu, D. Wang, Y. Zhang, Z. Liang, J. Li, J. Zeng, J. Zhang, Y. Xu, S. Wu, Z. Liu, X. Zhou, B. Hu, F. He, L. Zhang, X. Pan, X. Wang, N.-G. Park and B. Xu, *Science*, 2024, **383**, 524–531.
140 R. Chen, J. Wang, Z. Liu, F. Ren, S. Liu, J. Zhou, H. Wang, X. Meng, Z. Zhang, X. Guan, W. Liang, P. A. Troshin, Y. Qi, L. Han and W. Chen, *Nat. Energy*, 2023, **8**, 839–849.
141 S. Liu, J. Li, W. Xiao, R. Chen, Z. Sun, Y. Zhang, X. Lei, S. Hu, M. Kober-Czerny, J. Wang, F. Ren, Q. Zhou, H. Raza, Y. Gao, Y. Ji, S. Li, H. Li, L. Qiu, W. Huang, Y. Zhao, B. Xu, Z. Liu, H. J. Snaith, N. G. Park and W. Chen, *Nature*, 2024, **632**, 536–542.
142 C. Liu, Y. Yang, H. Chen, I. Spanopoulos, A. S. R. Bati, I. W. Gilley, J. Chen, A. Maxwell, B. Vishal, R. P. Reynolds, T. E. Wiggins, Z. Wang, C. Huang, J. Fletcher, Y. Liu, L. X. Chen, S. De Wolf, B. Chen, D. Zheng, T. J. Marks, A. Facchetti, E. H. Sargent and M. G. Kanatzidis, *Nature*, 2024, **633**, 359–364.
143 Q. Tan, Z. Li, G. Luo, X. Zhang, B. Che, G. Chen, H. Gao, D. He, G. Ma, J. Wang, J. Xiu, H. Yi, T. Chen and Z. He, *Nature*, 2023, **620**, 545–551.
144 T. Wu, Z. Qin, Y. Wang, Y. Wu, W. Chen, S. Zhang, M. Cai, S. Dai, J. Zhang, J. Liu, Z. Zhou, X. Liu, H. Segawa, H. Tan, Q. Tang, J. Fang, Y. Li, L. Ding, Z. Ning, Y. Qi, Y. Zhang and L. Han, *Nano-Micro Lett.*, 2021, **13**, 152.
145 B. Dong, M. Wei, Y. Li, Y. Yang, W. Ma, Y. Zhang, Y. Ran, M. Cui, Z. Su, Q. Fan, Z. Bi, T. Edvinsson, Z. Ding, H. Ju, S. You, S. M. Zakeeruddin, X. Li, A. Hagfeldt, M. Grätzel and Y. Liu, *Nat. Energy*, 2025, **10**, 342–353.
146 J. H. Noh, S. H. Im, J. H. Heo, T. N. Mandal and S. I. Seok, *Nano Lett.*, 2013, **13**, 1764–1769.
147 S. D. Stranks, G. E. Eperon, G. Grancini, C. Menelaou, M. J. P. Alcocer, T. Leijtens, L. M. Herz, A. Petrozza and H. J. Snaith, *Science*, 2013, **342**, 341–344.
148 M. Liu, M. B. Johnston and H. J. Snaith, *Nature*, 2013, **501**, 395–398.
149 J. Burschka, N. Pellet, S. J. Moon, R. Humphry-Baker, P. Gao, M. K. Nazeeruddin and M. Gratzel, *Nature*, 2013, **499**, 316–319.

150 W. Qiu, T. Merckx, M. Jaysankar, C. Masse de la Huerta, L. Rakocevic, W. Zhang, U. W. Paetzold, R. Gehlhaar, L. Froyen, J. Poortmans, D. Cheyns, H. J. Snaith and P. Heremans, *Energy Environ. Sci.*, 2016, **9**, 484–489.

151 X. Liu, M. Chen, Y. Zhang, J. Xia, J. Yin, M. Li, K. G. Brooks, R. Hu, X. Gao, Y.-H. Kim, A. Züttel, J. M. Luther, S. Kinge, Y. Feng and M. K. Nazeeruddin, *Chem. Eng. J.*, 2022, **431**, 133713.

152 M. Kim, J. Jeong, H. Lu, T. K. Lee, F. T. Eickemeyer, Y. Liu, I. W. Choi, S. J. Choi, Y. Jo, H.-B. Kim, S.-I. Mo, Y.-K. Kim, H. Lee, N. G. An, S. Cho, W. R. Tress, S. M. Zakeeruddin, A. Hagfeldt, J. Y. Kim, M. Grätzel and D. S. Kim, *Science*, 2022, **375**, 302–306.

153 T. Bu, L. K. Ono, J. Li, J. Su, G. Tong, W. Zhang, Y. Liu, J. Zhang, J. Chang, S. Kazaoui, F. Huang, Y.-B. Cheng and Y. Qi, *Nat. Energy*, 2022, **7**, 528–536.

154 X. Dai, S. Chen, H. Jiao, L. Zhao, K. Wang, Z. Ni, Z. Yu, B. Chen, Y. Gao and J. Huang, *Nat. Energy*, 2022, **7**, 923–931.

155 J. Chung, S. W. Kim, Y. Li, T. Mariam, X. Wang, M. Rajakaruna, M. M. Saeed, A. Abudulimu, S. S. Shin, K. N. Guye, Z. Huang, R. J. E. Westbrook, E. Miller, B. Subedi, N. J. Podraza, M. J. Heben, R. J. Ellingson, D. S. Ginger, Z. Song and Y. Yan, *Adv. Energy Mater.*, 2023, **13**, 2300595.

156 C. Fei, N. Li, M. Wang, X. Wang, H. Gu, B. Chen, Z. Zhang, Z. Ni, H. Jiao, W. Xu, Z. Shi, Y. Yan and J. Huang, *Science*, 2023, **380**, 823–829.

157 P. Shi, Y. Ding, B. Ding, Q. Xing, T. Kodalle, C. M. Sutter-Fella, I. Yavuz, C. Yao, W. Fan, J. Xu, Y. Tian, D. Gu, K. Zhao, S. Tan, X. Zhang, L. Yao, P. J. Dyson, J. L. Slack, D. Yang, J. Xue, M. K. Nazeeruddin, Y. Yang and R. Wang, *Nature*, 2023, **620**, 323–327.

158 Y. Kim, G. Kim, E. Y. Park, C. S. Moon, S. J. Lee, J. J. Yoo, S. Nam, J. Im, S. S. Shin, N. J. Jeon and J. Seo, *Energy Environ. Sci.*, 2023, **16**, 2226–2238.

159 X. Zhang, W. Qiu, S. Apergi, S. Singh, P. Marchezi, W. Song, C. Sternemann, K. Elkhouly, D. Zhang, A. Aguirre, T. Merckx, A. Krishna, Y. Shi, A. Bracesco, C. van Helvoirt, F. Bens, V. Zardetto, J. D'Haen, A. Yu, G. Brocks, T. Aernouts, E. Moons, S. Tao, Y. Zhan, Y. Kuang and J. Poortmans, *ACS Energy Lett.*, 2023, **8**, 2532–2542.

160 H. Zhou, K. Cai, S. Yu, Z. Wang, Z. Xiong, Z. Chu, X. Chu, Q. Jiang and J. You, *Nat. Commun.*, 2024, **15**, 6679.

161 Y. Yang, C. Liu, Y. Ding, B. Ding, J. Xu, A. Liu, J. Yu, L. Grater, H. Zhu, S. S. Hadke, V. K. Sangwan, A. S. R. Bati, X. Hu, J. Li, S. M. Park, M. C. Hersam, B. Chen, M. K. Nazeeruddin, M. G. Kanatzidis and E. H. Sargent, *Nat. Energy*, 2024, **9**, 316–323.

162 Y. Ding, B. Ding, P. Shi, J. Romano-deGea, Y. Li, R. C. Turnell-Ritson, O. A. Syzgantseva, I. Yavuz, M. Xia, R. Yu, M. A. Syzgantseva, J.-N. Audinot, X. Miao, X. Liao, J. Li, P. Dörflinger, V. Dyakonov, C. Liu, Y. Yang, L. Tao, K. G. Brooks, A. Slonopas, J. Pan, L. Zhang, Q. An, Y. Rong, J. Peng, L. Ding, E. Shi, L. Mai, S. Dai, K. Zhao, J. Sheng, R. Wang, P. J. Dyson and M. K. Nazeeruddin, *Science*, 2024, **386**, 531–538.

163 B. Ding, Y. Ding, J. Peng, J. Romano-deGea, L. E. K. Frederiksen, H. Kanda, O. A. Syzgantseva, M. A. Syzgantseva, J. N. Audinot, J. Bour, S. Zhang, T. Wirtz, Z. Fei, P. Dorflinger, N. Shibayama, Y. Niu, S. Hu, S. Zhang, F. F. Tirani, Y. Liu, G. J. Yang, K. Brooks, L. Hu, S. Kinge, V. Dyakonov, X. Zhang, S. Dai, P. J. Dyson and M. K. Nazeeruddin, *Nature*, 2024, **628**, 299–305.

164 J. Wang, L. Bi, X. Huang, Q. Feng, M. Liu, M. Chen, Y. An, W. Jiang, F. R. Lin, Q. Fu and A. K. Y. Jen, *eScience*, 2024, **4**, 100308.

165 Y. Liu, B. Ding, G. Zhang, X. Ma, Y. Wang, X. Zhang, L. Zeng, M. K. Nazeeruddin, G. Yang and B. Chen, *Adv. Sci.*, 2024, **11**, e2309111.

166 J. Zhang, X. Ji, X. Wang, L. Zhang, L. Bi, Z. Su, X. Gao, W. Zhang, L. Shi, G. Guan, A. Abudula, X. Hao, L. Yang, Q. Fu, A. K. Jen and L. Lu, *Nano-Micro Lett.*, 2024, **16**, 190.

167 Y. Xu, C. Zhou, X. Li, K. Du, Y. Li, X. Dong, N. Yuan, L. Li and J. Ding, *Small Methods*, 2024, **8**, e2400428.

168 L. Tao, Y. Huang, B. Ding, H. Wang, J. Tang, S. Zhang, J. Zhang, M. K. Nazeeruddin and H. Wang, *Mater. Today Energy*, 2024, **44**, 101611.

169 X. Zhu, D. Yu, X. Zhou, N. Wang, H. Liu, Z. Liang, C. Wu, K. Wang, D. Jin, S. Liu and D. Yang, *Joule*, 2025, **9**, 101919.

170 Y. S. Shin, J. W. Song, D. G. Lee, J. Lee, J. Seo, J. Roe, G. Y. Shin, D. Kim, J. Yeop, D. Lee, M. Kim, Y. Jo, H. Jang, J. G. Son, W. Lee, J. Son, S. Park, S. Cho, T. J. Shin, G.-H. Kim, J. Y. Kim, T. K. Lee, M. Grätzel and D. S. Kim, *Joule*, 2025, **9**, 101779.

171 A. L. Palma, *Sol. RRL*, 2019, **4**, 1900432.

172 A. Fakharuddin, F. D. Giacomo, A. L. Palma, F. Matteocci, I. Ahmed, S. Razza, A. D'Epifanio, S. Licoccia, J. Ismail, A. D. Carlo, T. M. Brown and R. Jose, *ACS Nano*, 2015, **9**, 8420–8429.

173 J. H. Heo, H. J. Han, D. Kim, T. K. Ahn and S. H. Im, *Energy Environ. Sci.*, 2015, **8**, 1602–1608.

174 H. C. Liao, P. Guo, C. P. Hsu, M. Lin, B. Wang, L. Zeng, W. Huang, C. M. M. Soe, W. F. Su, M. J. Bedzyk, M. R. Wasielewski, A. Facchetti, R. P. H. Chang, M. G. Kanatzidis and T. J. Marks, *Adv. Energy Mater.*, 2016, **7**, 1601660.

175 S. M. P. Meroni, K. E. A. Hooper, T. Dunlop, J. A. Baker, D. Worsley, C. Charbonneau and T. M. Watson, *Energies*, 2020, **13**, 1589.

176 M. Yang, Z. Li, M. O. Reese, O. G. Reid, D. H. Kim, S. Siol, T. R. Klein, Y. Yan, J. J. Berry, M. F. A. M. van Hest and K. Zhu, *Nat. Energy*, 2017, **2**, 17038.

177 C. Zuo, F. Hao, H. Dong, J. Chang, K. Yan, Y. Ding, Z. Xiao and L. Ding, *Energy Environ. Sci.*, 2025, **18**, 10125–10134.

178 C. Chen, J. Chen, H. Han, L. Chao, J. Hu, T. Niu, H. Dong, S. Yang, Y. Xia, Y. Chen and W. Huang, *Nature*, 2022, **612**, 266–271.

179 Y. Jiang, C. Wu, L. Li, K. Wang, Z. Tao, F. Gao, W. Cheng, J. Cheng, X.-Y. Zhao, S. Priya and W. Deng, *Nano Energy*, 2018, **53**, 440–448.

180 S. G. Hashmi, D. Martineau, X. Li, M. Ozkan, A. Tiihonen, M. I. Dar, T. Sarikka, S. M. Zakeeruddin, J. Paltakari, P. D. Lund and M. Grätzel, *Adv. Mater. Technol.*, 2016, **2**, 1600183.

181 J. Yang, E. L. Lim, L. Tan and Z. Wei, *Adv. Energy Mater.*, 2022, **12**, 2200975.

182 J.-E. Kim, Y.-S. Jung, Y.-J. Heo, K. Hwang, T. Qin, D.-Y. Kim and D. Vak, *Sol. Energy Mater. Sol. Cells*, 2018, **179**, 80–86.
183 A. Bashir, S. Shukla, J. H. Lew, S. Shukla, A. Bruno, D. Gupta, T. Baikie, R. Patidar, Z. Akhter, A. Priyadarshi, N. Mathews and S. G. Mhaisalkar, *Nanoscale*, 2018, **10**, 2341–2350.
184 S. S. Sangale, D. S. Mann, H.-J. Lee, S.-N. Kwon and S.-I. Na, *Commun. Mater.*, 2024, **5**, 201.
185 J. B. Whitaker, D. H. Kim, B. W. Larson, F. Zhang, J. J. Berry, M. F. A. M. van Hest and K. Zhu, *Sustainable Energy Fuels*, 2018, **2**, 2442–2449.
186 T. R. Rana, M. Abbas, E. Schwartz, F. Jiang, M. Y. Yaman, Z. Xu, D. S. Ginger and D. MacKenzie, *ACS Energy Lett.*, 2024, **9**, 1888–1894.
187 R. Patidar, D. Burkitt, K. Hooper, D. Richards and T. Watson, *Mater. Today Commun.*, 2020, **22**, 100808.
188 Y. Deng, C. H. V. Brackle, X. Dai, J. Zhao, B. Chen and J. Huang, *Sci. Adv.*, 2019, **5**, eaax7537.
189 B. Taheri, E. Calabrò, F. Matteocci, D. Di Girolamo, G. Cardone, A. Liscio, A. Di Carlo and F. Brunetti, *Energy Technol.*, 2020, **8**, 1901284.
190 B. Tyagi, N. Kumar, H. B. Lee, M. M. Ovhal, V. V. Satale, A. Mohamed, D. H. Kim and J. W. Kang, *Small Methods*, 2024, **8**, e2300237.
191 J. Su, X. Zheng, H. Guo, S. Jiang, H. Tian, J. Yang, X. Ye, H. Cai, J. Ni, J. Qiu and J. Zhang, *J. Electron. Mater.*, 2022, **51**, 2396–2405.
192 J. G. Tait, S. Manghooli, W. Qiu, L. Rakocevic, L. Kootstra, M. Jaysankar, C. A. Masse de la Huerta, U. W. Paetzold, R. Gehlhaar, D. Cheyns, P. Heremans and J. Poortmans, *J. Mater. Chem. A*, 2016, **4**, 3792–3797.
193 J. H. Heo, F. Zhang, C. Xiao, S. J. Heo, J. K. Park, J. J. Berry, K. Zhu and S. H. Im, *Joule*, 2021, **5**, 481–494.
194 B. Gao and J. Meng, *Sol. Energy*, 2021, **230**, 598–604.
195 D. A. Chalkias, A. Mourtzikou, G. Katsagounos, A. N. Kalarakis and E. Stathatos, *Small Methods*, 2023, **7**, e2300664.
196 H. C. Weerasinghe, N. Macadam, J. E. Kim, L. J. Sutherland, D. Angmo, L. W. T. Ng, A. D. Scully, F. Glenn, R. Chantler, N. L. Chang, M. Dehghanimadvar, L. Shi, A. W. Y. Ho-Baillie, R. Egan, A. S. R. Chesman, M. Gao, J. J. Jasieniak, T. Hasan and D. Vak, *Nat. Commun.*, 2024, **15**, 1656.
197 J. Yi, T. L. Leung, J. Digweed, J. Bing, C. Bailey, C. Liao, R. Tao, G. Wang, Z. Li, H. T. Nguyen, D. R. McCamey, J. Zheng, M. A. Mahmud and A. W. Y. Ho-Baillie, *Small*, 2024, **20**, e2402215.
198 Z. Chu, B. Fan, Y. Zhao, Y. Xie, Y. Luo, J. Li, C. Gong, Y. Zhang, X. Meng, Y. Chen, H. Li, X. Hu and Y. Chen, *Science*, 2025, **390**, 905–910.
199 F. U. Kosasih, L. Rakocevic, T. Aernouts, J. Poortmans and C. Ducati, *ACS Appl. Mater. Interfaces*, 2019, **11**, 45646–45655.
200 L. Bayer, M. Ehrhardt, P. Lorenz, S. Pisoni, S. Buecheler, A. N. Tiwari and K. Zimmer, *Appl. Surf. Sci.*, 2017, **416**, 112–117.
201 L. Bayer, X. Ye, P. Lorenz and K. Zimmer, *Appl. Phys.*, 2017, **123**, 619.
202 Y. Gao, C. Liu, Y. Xie, R. Guo, X. Zhong, H. Ju, L. Qin, P. Jia, S. Wu, R. E. I. Schropp and Y. Mai, *Adv. Energy Mater.*, 2022, **12**, 2202287.
203 M. Fenske, C. Schultz, J. Dagar, F. U. Kosasih, A. Zeiser, C. Junghans, A. Bartelt, C. Ducati, R. Schlatmann, E. Unger and B. Stegemann, *Energy Technol.*, 2021, **9**, 2000969.
204 C. Wang, G. Y. Tan, X. P. Luo, J. Li, X. F. Gao, Y. P. Mo, X. L. Zhang, X. W. Wang and F. Z. Huang, *J. Power Sources*, 2020, **466**, 228321.
205 N. N. Udalova, A. S. Tutantsev, Q. Chen, A. Kraskov, E. A. Goodilin and A. B. Tarasov, *ACS Appl. Mater. Interfaces*, 2020, **12**, 12755–12762.
206 E. Bi, W. Tang, H. Chen, Y. Wang, J. Barbaud, T. Wu, W. Kong, P. Tu, H. Zhu, X. Zeng, J. He, S.-I. Kan, X. Yang, M. Grätzel and L. Han, *Joule*, 2019, **3**, 2748–2760.
207 D. Jiang, Z. Liu, J. Li, H. Cao, Y. Qian, Z. Ren, S. Zhang, Y. Qiu, C. Zhang, J. Wei, L. Yang and S. Yin, *Joule*, 2024, **8**, 1161–1175.
208 C. Schultz, M. Fenske, J. Dagar, A. Zeiser, A. Bartelt, R. Schlatmann, E. Unger and B. Stegemann, *Sol. Energy*, 2020, **198**, 410–418.
209 L. Ma, Z. Yan, X. Zhou, Y. Pi, Y. Du, J. Huang, K. Wang, K. Wu, C. Zhuang and X. Han, *Nat. Commun.*, 2021, **12**, 2023.
210 S. Hong, J. Lee, H. Kang, G. Kim, S. Kee, J.-H. Lee, S. Jung, B. Park, S. Kim, H. Back, K. Yu and K. Lee, *Sci. Adv.*, 2018, **4**, eaat3604.
211 X. Liu, J. Zhang, H. Wang, Y. Miao, T. Guo, L. K. Ono, S. Yuan, Y. Wang, P. Ji, H. Chen, C. Zhang, T. Li, C. Ding, S. Mariotti, X. Huo, I.-N. Rabehi, H. Wang, Y. Zhao and Y. Qi, *Joule*, 2024, **8**, 2851–2862.
212 L. Yu, W. Zhang, H. Ge, G. Yan, W. Yu, Y. Du, L. Zhou, W. Long and Y. Huang, *Catalysts*, 2023, **13**, 953.
213 A. Jeong, J. M. Choi, H. J. Lee, G. Y. Kim, J. K. Park, W. M. Kim, S. Kuk, Z. Wang, D. J. Hwang, H. Yu and J. H. Jeong, *Prog. Photovoltaics*, 2021, **30**, 713–725.
214 S. Baumann, G. E. Eperon, A. Virtuani, Q. Jeangros, D. B. Kern, D. Barrit, J. Schall, W. Nie, G. Oreski, M. Khenkin, C. Ulbrich, R. Peibst, J. S. Stein and M. Köntges, *Energy Environ. Sci.*, 2024, **17**, 7566–7599.
215 D. B. Ritzer, T. Abzieher, A. Basibüyük, T. Feeney, F. Laufer, S. Ternes, B. S. Richards, S. Bergfeld and U. W. Paetzold, *Prog. Photovoltaics*, 2021, **30**, 360–373.
216 L. Rakocevic, G. Schöpe, B. Turan, J. Genoe, T. Aernouts, S. Haas, R. Gehlhaar and J. Poortmans, *Prog. Photovoltaics*, 2020, **28**, 1120–1127.
217 G. Boschloo, *ACS Energy Lett.*, 2023, **8**, 1147–1151.
218 L. Vesce, M. Stefanelli, L. A. Castriotta, A. Hadipour, S. Lammar, B. Yang, J. Suo, T. Aernouts, A. Hagfeldt and A. Di Carlo, *Sol. RRL*, 2022, **6**, 2101095.
219 H. Wu, J. Zhang, Y. Zhang, F. Cao, Z. Qiu, L. Zhang, A. M. Asiri, P. J. Dyson, M. K. Nazeeruddin, J. Ye and C. Xiao, *ACS Appl. Mater. Interfaces*, 2024, **16**, 41986–41995.
220 J. W. Schall, A. Glaws, N. Y. Doumon, T. J. Silverman, M. Owen-Bellini, K. Terwilliger, M. A. Uddin, P. Rana, J. J. Berry, J. Huang, L. T. Schelhas and D. B. Kern, *Sol. RRL*, 2023, **7**, 2300229.
221 A. Wehrmann, S. Puttnins, L. Hartmann, M. Ehrhardt, P. Lorenz and K. Zimmer, *Opt. Laser Technol.*, 2012, **44**, 1753–1757.

222 B. H. S. Miranda, L. d Q. Corrêa, G. A. Soares, J. L. Martins, P. L. Lopes, M. L. Vilela, J. F. Rodrigues, T. G. Cunha, R. d Q. Vilaça, S. Castro-Hermosa, L. Wouk and D. Bagnis, *Sol. Energy*, 2021, **220**, 343–353.
223 C.-Y. Lee, C.-S. Tsao, H.-K. Lin, H.-C. Cha, T.-Y. Chung, Y.-M. Sung and Y.-C. Huang, *Sol. Energy*, 2021, **213**, 136–144.
224 A. Gusain, A. Thankappan and S. Thomas, *J. Mater. Sci.*, 2020, **55**, 13490–13542.
225 D. Vak, K. Hwang, A. Faulks, Y. S. Jung, N. Clark, D. Y. Kim, G. J. Wilson and S. E. Watkins, *Adv. Energy Mater.*, 2015, **5**, 1401539.
226 Y. J. Heo, Y. S. Jung, K. Hwang, J. E. Kim, J. S. Yeo, S. Lee, Y. J. Jeon, D. Lee and D. Y. Kim, *ACS Appl. Mater. Interfaces*, 2017, **9**, 39519–39525.
227 L. Mao, B. Luo, L. Sun, S. Xiong, J. Fan, F. Qin, L. Hu, Y. Jiang, Z. Li and Y. Zhou, *Mater. Horiz.*, 2018, **5**, 123–130.
228 S. S. Sangale, S. N. Kwon, P. Patil, H. J. Lee and S. I. Na, *Adv. Energy Mater.*, 2023, **13**, 2300537.
229 J. Petry, V. Škorjanc, A. Diercks, T. Feeney, A. Morsa, S. R. Kimmig, J. Baumann, F. Löffler, S. Auschill, J. Damm, D. Baumann, F. Laufer, J. Kurpiers, M. Müller, L. Korte, S. Albrecht, M. Roß, U. W. Paetzold and P. Fassl, *EES Sol.*, 2025, **1**, 404–418.
230 X. Jia, C. Zhou, Y. Tang and W. Wang, *Sol. Energy Mater. Sol. Cells*, 2021, **227**, 111112.
231 D. Cheng and Y. Gao, *Sol. Energy Mater. Sol. Cells*, 2024, **274**, 112999.
232 Z. Xie, H. Lu, G. Yang, Z. Gao, K. Zhu, Y. Wang, Z. Meng, C. Guo, H. Pei, Q. Jiang, H. Li, S. Zhang, H. Chu, X. Chen, Y. Chen and J. Gao, *Nat. Commun.*, 2025, **16**, 9421.
233 N. Espinosa, M. Hösel, M. Jørgensen and F. C. Krebs, *Energy Environ. Sci.*, 2014, **7**, 855–866.
234 R. García-Valverde, S. Chaouki-Almagro, M. Corazza, N. Espinosa, M. Hösel, R. R. Søndergaard, M. Jørgensen, J. A. Villarejo and F. C. Krebs, *Sol. Energy Mater. Sol. Cells*, 2016, **151**, 60–65.
235 Y. Hu, S. Si, A. Mei, Y. Rong, H. Liu, X. Li and H. Han, *Sol. RRL*, 2017, **1**, 1600019.
236 Y. Rong, Y. Hu, A. Mei, H. Tan, M. I. Saidaminov, S. I. Seok, M. D. McGehee, E. H. Sargent and H. Han, *Science*, 2018, **361**, eaat8235.
237 A. Mahmood and J.-L. Wang, *Energy Environ. Sci.*, 2021, **14**, 90–105.
238 H. Wang, J. Feng, Z. Dong, L. Jin, M. Li, J. Yuan and Y. Li, *npj Comput. Mater.*, 2023, **9**, 200.
239 S. Shafian, M. N. Husen, L. Xie and K. Kim, *Mater. Today Sustainability*, 2025, **31**, 101176.
240 V. de la Asunción-Nadal, C. Iliffe Sprague, B. Guijarro-Berdiñas, U. B. Cappel and A. García-Fernández, *EES Sol.*, 2025, **1**, 927–957.
241 X. Cai, F. Liu, A. Yu, J. Qin, M. Hatamvand, I. Ahmed, J. Luo, Y. Zhang, H. Zhang and Y. Zhan, *Light: Sci. Appl.*, 2022, **11**, 234.
242 A. Mannodi-Kanakkithodi and M. K. Y. Chan, *Energy Environ. Sci.*, 2022, **15**, 1930–1949.
243 Q. Song, Y. Bai and Q. Chen, *J. Phys. Chem. Lett.*, 2022, **13**, 10741–10750.
244 W. Li, J. Hu, Z. Chen, H. Jiang, J. Wu, X. Meng, X. Fang, J. Lin, X. Ma, T. Yang, P. Cheng and R. Xie, *Sol. Energy*, 2023, **262**, 111853.
245 W. Xu, Z. Liu, R. T. Piper and J. W. P. Hsu, *Sol. Energy Mater. Sol. Cells*, 2023, **249**, 112055.
246 H. Zhan, V. Ahmad, A. Mayon, G. D. Tabi, A. D. Bui, Z. Li, D. Walter, H. Nguyen, K. Weber, T. White and K. Catchpole, *Energy Environ. Sci.*, 2024, **17**, 4735–4745.
247 S. Ament, M. Amsler, D. R. Sutherland, M.-C. Chang, D. Guevarra, A. B. Connolly, J. M. Gregoire, M. O. Thompson, C. P. Gomes and R. B. V. Dover, *Sci. Adv.*, 2021, **7**, eabg4930.
248 Ç. Odabaşı and R. Yıldırım, *Sol. Energy Mater. Sol. Cells*, 2020, **205**, 110284.
249 F. Laufer, M. Gotz and U. W. Paetzold, *Energy Environ. Sci.*, 2025, **18**, 1767–1782.